JOURNAL OF GEOPHYSICAL RESEARCH, VOL. 114, E08S92, doi:10.1029/2008JE003315, 2009

Mars Reconnaissance Orbiter Mars Color Imager (MARCI): Instrument description, calibration, and performance

J. F. Bell III,[1] M. J. Wolff,[2] M. C. Malin,[3] W. M. Calvin,[4] B. A. Cantor,[3] M. A. Caplinger,[3]
R. T. Clancy,[2] K. S. Edgett,[3] L. J. Edwards,[5] J. Fahle,[3] F. Ghaemi,[3] R. M. Haberle,[5]
A. Hale,[6] P. B. James,[7] S. W. Lee,[8] T. McConnochie,[1] E. Noe Dobrea,[1]
M. A. Ravine,[3] D. Schaeffer,[1] K. D. Supulver,[3] and P. C. Thomas[1]

Received 9 December 2008; revised 2 April 2009; accepted 5 May 2009; published 28 August 2009.

[1] The Mars Color Imager (MARCI) instrument aboard the NASA Mars Reconnaissance Orbiter spacecraft is a wide-angle, multispectral Charge-Coupled Device (CCD) "push frame" imaging camera designed to provide frequent, synoptic-scale color imaging of the Martian atmosphere and surface. MARCI uses a 1024 × 1024 pixel interline transfer CCD detector that has seven narrowband interference filters bonded directly to the CCD. Five of the filters are in the visible to short-wave near-infrared wavelength range (437, 546, 604, 653, and 718 nm) and two are in the ultraviolet range (258 and 320 nm). Here we describe the scientific objectives of the MARCI investigation and the basic characteristics, calibration, and in-flight performance of the MARCI instrument. We include several examples of early scientific results and investigations enabled by an extensive preflight and in-flight calibration program and by validation of the performance of the instrument in flight.

Citation: Bell, J. F., III, et al. (2009), Mars Reconnaissance Orbiter Mars Color Imager (MARCI): Instrument description, calibration, and performance, *J. Geophys. Res.*, *114*, E08S92, doi:10.1029/2008JE003315.

1. Introduction

[2] The Mars Color Imager (MARCI) is a wide-angle, seven-color (ultraviolet, visible, and shortwave near infrared) Charge-Coupled Device (CCD) framing camera, and is one of the primary science payload instruments on the NASA Mars Reconnaissance Orbiter (MRO) mission [*Zurek and Smrekar*, 2007]. The MARCI instrument (Figure 1) is designed for daily synoptic, low-resolution (1 to 10 km) imaging of Mars to study the evolution of weather systems and to observe changes in surface features that result from interactions with atmospheric processes. The major science goals of the MARCI investigation are as follows: (1) observe Martian atmospheric processes synoptically at global scale on a daily basis; (2) study details of the interaction of the atmosphere with the surface at a variety of scales in both space and time; (3) examine surface features characteristic of the evolution of the Martian climate; (4) obtain repeated, global coverage at scales between 1 and 10 km/pixel; (5) use multispectral imaging to distinguish between cloud compositions (water, CO_2 ice and dust); and (6) make UV observations at both limb and nadir to observe ozone as a measure of atmospheric photochemistry and as a surrogate for water vapor concentration. The camera operates in five visible and two ultraviolet (UV) bands, and has a 180° field of view that permits observations of the planetary limbs. The UV imaging capability is unique in Mars orbital mission studies, and comparison of images in the two UV filters enables the determination of seasonal changes in the concentration of ozone [e.g., *Clancy et al.*, 1996, 1999; *Malin et al.*, 2001, 2008]. The MRO MARCI instrument is based on the MARCI wide-angle (WA) camera that flew to Mars on the failed Mars Climate Orbiter (MCO) mission [*Malin et al.*, 2001], but it has been modified for the specific orbital and other constraints of the MRO mission, as well as modifications resulting from lessons learned during the original MCO MARCI WA instrument development and testing process.

[3] This paper describes the MARCI instrument, the procedures, data sets, and results from the preflight and in-flight calibration of the instrument and the validation of the radiometric, geometric, thermal, optical, and mechanical performance of the instrument against functional requirements defined by the MRO Project and the MARCI Science Team. Some examples of initial scientific results from the investigation are also included. A calibration campaign (described here) was established for MARCI in order to prioritize the test sequence, to allow verification of perfor-

---

[1] Department of Astronomy, Cornell University, Ithaca, New York, USA.
[2] Space Science Institute, Boulder, Colorado, USA.
[3] Malin Space Science Systems, Inc., San Diego, California, USA.
[4] Department of Geological Sciences and Engineering, University of Nevada, Reno, Reno, Nevada, USA.
[5] NASA Ames Research Center, Moffett Field, California, USA.
[6] Jet Propulsion Laboratory, Pasadena, California, USA.
[7] Department of Physics and Astronomy, University of Toledo, Toledo, Ohio, USA.
[8] Denver Museum of Nature and Science, Denver, Colorado, USA.

0148-0227/09/2008JE003315$09.00

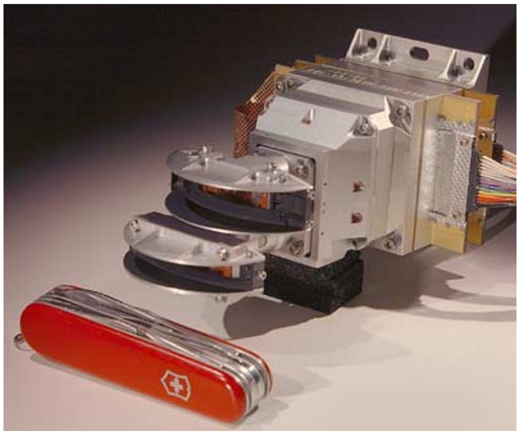

Figure 1. MRO MARCI camera and electronics assembly. The long lens and “taco shell” light baffle houses the UV optics; the short lens/baffle houses the visible wavelength optics. Swiss Army Knife shown for scale. The distance from the base of the electronics modules (behind the two wired plugs on the right here) to the tip of the UV optics is 14.5 cm.

mance to take place in a systematic and timely fashion, and to insure that the preflight (and in flight) calibration resulted in the delivery of a fully tested instrument that either met or exceeded its requirements (or for which deviations or exceptions to those requirements were fully understood and documented). The results described in this paper provide the data needed to calibrate the cameras and to understand the accuracy, precision, and limitations of calibrated MARCI data. This information could also be useful for future users of data from the Lunar Reconnaissance Orbiter Camera’s wide-angle camera [*Robinson et al.*, 2005; *Tschimmel et al.*, 2009], an instrument that is based on the MARCI design and which shares many of MARCI’s operational, calibration, and data analysis characteristics.

2. MARCI Scientific Objectives

[4] The primary goal of the MARCI investigation is to extend the long-term meteorological, climate, and surface-atmosphere interaction observations initiated by the Mars Global Surveyor (MGS) Mars Orbiter Camera wide-angle (MOC WA) instrument. The MARCI investigation is designed to acquire these observations globally at a synoptic scale similar to that of atmospheric processes as viewed by terrestrial weather satellites. The broader scientific goals of the MRO MARCI investigation are similar to those of the MCO MARCI WA investigation, and are summarized in section 1. Here we amplify those goals, objectives, and expectations under the broad categories of atmospheric studies and surface studies. Additional details related to the original MCO MARCI WA investigation are given by *Malin et al.* [2001, 2008].

2.1. Atmospheric Studies

[5] MARCI atmospheric investigations include studies of (1) the distribution of dust, condensates, and ozone in the atmosphere; (2) the structure of condensate clouds and their relationship to topography and to circulation patterns predicted by global circulation models (GCMs); (3) dust-raising events ranging in magnitude from large dust devils to localized dust clouds to planet-encircling dust storm events; and (4) polar phenomena. Among the major scientific questions being addressed are the following:

[6] 1. What is the seasonal and geographical variability in dust, ozone, and condensates in the Martian atmosphere?

[7] 2. What is the general circulation of Mars? How reliable are the predictions of GCMs, and how much interannual variability exists?

[8] 3. What role do clouds in general, and the polar hoods in particular, play in the global water cycle on Mars? Do they control the net interhemispheric transfer of water?

[9] 4. How do local and regional storms and planet-encircling dust events evolve? How are they related to the local-, meso-, and synoptic-scale circulations?

[10] 5. And how are the seasonal and residual caps involved in the global transport of water and dust on Mars? What is the direction of the net annual water transport on the planet?

2.1.1. Clouds

[11] Clouds probe many important properties of the Martian atmosphere and may be used to test dynamical atmospheric models (Figure 2). Discrete white clouds on Mars have been known for many years from the work of ground based astronomers [e.g., *Slipher*, 1962]; these are now known to be largely associated with major topographic features, such as the Tharsis and Elysium volcanoes. *Curran et al.* [1973] used Mariner 9 data to show that the prominent white clouds in the Tharsis and Olympus regions of Mars are composed of water ice. MOC WA daily mapping of Mars has shown that the seasonal behavior of the various cloud components are unique to each cloud system [*Benson et al.*, 2003] but are repeatable from 1 Mars year to another [*Benson et al.*, 2006]. Hubble Space Telescope (HST) Wide Field/Planetary Camera-2 (WFPC2) observations in 1995 revealed a planet-encircling belt of diffuse clouds displaced about 10° north of the equator during late spring and early summer in the northern hemisphere [*Clancy et al.*, 1996; *James et al.*, 1996]. This water ice cloud belt has subsequently been found to be a regular feature on Mars during this aphelion season [*Wolff et al.*, 1999; *Smith*, 2004].

[12] Water ice clouds are most prominent during the northern summer aphelion season and play an important

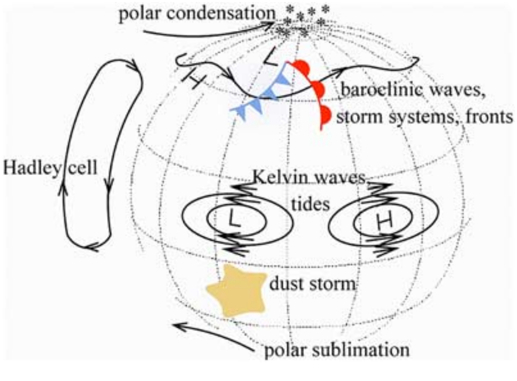

Figure 2. Cartoon depicting the main components of the general circulation on Mars. Figure courtesy of David Catling.

role in limiting the vertical propagation (and hence hemispherical transport) of water vapor by the synoptic-scale circulation system [*Clancy et al.*, 1996; *Richardson et al.*, 2002; *Montmessin et al.*, 2004]. However, the current picture is still far from complete. Thick, diurnally cyclic orographic clouds associated with the elevated topography of the large volcanoes are superimposed on the planet encircling, diffuse aphelion cloud band [e.g., *Wolff et al.*, 1999]. These are very different phenomena, despite the fact that they are both related to the seasonal maximum in northern hemisphere water vapor, cold aphelion temperatures, and low-saturation altitude [*Clancy et al.*, 1996].

[13] During the past decade, various mesoscale atmospheric models have been developed that can investigate details of the orographic clouds such as particle size distributions, opacities, and elevations [e.g., *Richardson et al.*, 2002; *Richardson and Wilson*, 2002; *Toigo et al.*, 2002]. MARCI's spectral range, high spatial resolution relative to the size of clouds, and good calibration enable the potential to directly measure cloud properties for comparison with models. For example, the reflectance of the clouds can depend sensitively upon the scattering properties of the cloud aerosols, such as the single scattering phase function and the size distribution. MARCI images acquired over a wide range of phase angles as well as potentially in several wavelength bands can be used to constrain these parameters.

[14] Interannual variations in the seasonal behavior of clouds were small during the first 4 years they were observed using the MGS MOC [*Benson et al.*, 2006]. The 2001 planet-encircling dust event, which occurred near the end of the cloud season, mainly affected the behavior of clouds associated with Arsia Mons [*Cantor*, 2007b], which alone tend to persist into southern spring and summer. However, one motivation for the MARCI investigation was the fact that observations of just four seasons were deemed insufficient to establish long-term invariability, especially since prior to MRO there had been no Mars years with major perihelic dust storms observed. An important MARCI investigation goal is thus continuing important monitoring of the seasonal cycles of the major clouds and the aphelion cloud belt.

[15] Both dust and condensate clouds are very prominent in the neighborhood of the north polar cap. These clouds are associated with frontal systems that sometimes give rise to major regional dust storms that can move from the northern to the southern hemisphere [*Cantor et al.*, 2001; *Wang et al.*, 2005] and that play an important role in closing the dust cycle on the planet.

[16] More recently, ice clouds have been detected at mesospheric altitudes (~50–80 km), as optically bright layers at equatorial latitudes [*Clancy et al.*, 2004; *McConnochie et al.*, 2006] and as diffuse hazes extending to altitudes above 100 km (F. Montmessin, J. L. Bertaux, and P. Rannou, Stellar occultations at UV wavelengths by the SPICAM instrument: Retrieval and analysis of Martian haze profiles, paper presented at 2nd International Workshop on Mars Atmospheric Modeling and Observations, Laboratoire de Meteorologie Dynamique/European Space Agency, Granada, Spain, 27 February to 3 March, 2006). These bright equatorial clouds have been inferred to include large particles (>1.0 μm) of CO_2 [*Montmessin et al.*, 2007]. The diffuse hazes appear to be composed of very fine CO_2 particles (<0.1 μm). Both types of mesospheric clouds appear to form at particularly cold atmospheric temperatures. The microphysics of ice aerosol formation for either type of mesospheric cloud is poorly constrained by the available observations, as are any climate or dynamical implications associated with these high-altitude clouds. MARCI full color limb imaging provides the potential for extensive wavelength and global coverage of such Mars mesospheric cloud (and dust) aerosols.

2.1.2. General Circulation

[17] The present Martian climate system is characterized by the seasonal cycles of dust, water, and CO_2, which are coupled through the general circulation. Figure 2 depicts the major components of the general circulation as we currently understand them from models and observations. These include traveling baroclinic waves and forced stationary waves in the winter hemisphere, low-latitude Hadley cells and thermal tides, high-altitude jet streams, cap edge circulations, and CO_2 condensation flow.

[18] MARCI observations of dust and clouds can help illuminate the nature of the general circulation and its role in controlling the dust and water cycles. The key issues for the dust cycle are the role the general circulation plays in lifting, transporting, and depositing dust around the planet, and the feedbacks between dust heating and the general circulation. MOC WA images have shown the value of routine synoptic observations in characterizing seasonal and temporal variations in dust lifting by the large-scale wind field [*Haberle et al.*, 2003; *Wang et al.*, 2005; *Strausberg et al.*, 2005; *Kahre et al.*, 2005; *Cantor*, 2007a]. These studies have shown that while virtually every component of the general circulation plays a role in dust lifting, a full understanding of each role still remains elusive.

[19] For example, MOC observations of the 2001 planet-encircling dust event suggest that it began with a series of dust pulses generated along the southwestern edge of the Hellas basin [*Cantor*, 2007a, 2007b]. The period of these pulses (~2–3 sols) closely matches that expected for traveling baroclinic eddies, yet how these systems triggered the onset of widespread lifting throughout Hellas as well as to the north and east of it are uncertain. Furthermore, despite some tantalizing indications of connections [*Haberle et al.*, 2005], it is not understood how (or even if) the events in Hellas then triggered the main lifting center in Claritas, almost halfway around the planet. Continued observations by MARCI with its color and limb-viewing capabilities can directly address questions related to the role of the general circulation in the dust cycle.

[20] Water ice clouds are now believed to play an important role in controlling the net meridional transport of water between hemispheres. *Clancy et al.* [1996] suggested that the altitude in the rising branch of the Hadley circulation at which they form controls how much vapor is exchanged between hemispheres, and general circulation models support this suggestion [e.g., *Richardson and Wilson*, 2002; *Montmessin et al.*, 2004]. Furthermore, the radiative effects of Martian clouds may have a significant impact on the thermal tides, a major component of the general circulation [*Hinson and Wilson*, 2004]. Clouds can also provide wind information through direct tracking of their movement [*Wang and Ingersoll*, 2002; *Mischna et al.*, 1998], and mapping the distribution and orientation of lee waves [*Kahn*, 1984]. MARCI's synoptic coverage and well-calibrated color channels in the visible enable an improvement in our

understanding of the frequency, location, altitude, and opacities of clouds on Mars and their implications for the general circulation.

[21] MARCI observations of both clouds and dust provide data with which to test general circulation model predictions that traveling baroclinic eddies are more vigorous in the northern hemisphere compared to the southern hemisphere [*Barnes et al.*, 1993], and that they tend to be concentrated along certain longitude sectors that have come to be known as "storm zones" [e.g., *Hollingsworth et al.*, 1996]. The storm zones seem to be most intense on the poleward flanks of the Tharsis rise, with other less intense zones in Acidalia, Utopia, and southwestern Hellas. Continuous monitoring of clouds and dust in these regions can provide information on the seasonal variation of activity in these regions, as well as on some of the basic properties of the eddies (phase speed and wavelength).

2.1.3. Interannual Repeatable Weather/Climate

[22] Ground-based temperature profiles, HST WFPC2 imaging, and MGS Thermal Emission Spectrometer (TES) temperature profiles [*Smith*, 2004] suggest generally colder atmospheric temperatures and lower dust loading in recent decades on Mars than during the Viking Mission [*Clancy et al.*, 1990, 2000; *James et al.*, 1994]. This distinction appeared most significant for the northern spring/summer season (around aphelion). The more recent observations suggest that the typical behavior of the Mars aphelion atmosphere may be more characterized by low dust loading, reduced atmospheric temperatures, low-altitude water vapor saturation, and a 10°S to 30°N global belt of moderate opacity clouds [*Clancy et al.*, 1996; *Wolff et al.*, 1999; *Smith*, 2004]. The implication is that low-altitude saturation impedes transport of water vapor into the southern hemisphere during this season and thereby has a significant impact on the global water distribution. However, reevaluation of the Viking infrared atmospheric temperature data [*Wilson and Richardson*, 2000] indicates little interannual variability in global temperatures during the aphelion season. This is consistent with the interannually repeatable atmospheric events (dust devils, dust storms and condensate clouds) observed by MGS MOC [*Cantor et al.*, 2002; *Benson et al.*, 2003], during the same season between 1997 and 2001. Global mapping observations from MGS beyond 2001 suggest that in the present Martian climate, seasonal weather patterns (condensate clouds, dust devils, and dust storms) are generally repeatable from 1 Mars year to the next within a $\sim$14 sol period [*Cantor*, 2003, 2007a, 2007b; *Cantor et al.*, 2006; *Cantor and Malin*, 2007]. However, some weather phenomena, such as the 2001 and 2007 planet-encircling dust events and the large annual regional storms that generate planet-encircling dust hazes, were observed to perturb the above interannual repeatability for short periods of time (a few months) before the atmosphere resumed the predictable cycle again [*Cantor*, 2007a, 2007b; *Cantor and Malin*, 2007].

2.1.4. Dust Devils and Dust Storms

[23] In the past, global mapping was important for monitoring all but the smallest-scale dust activity on Mars. However, MARCI's kilometer-scale ground-sampling resolution is capable of imaging the largest dust devils, which have been observed across much of Mars [*Cantor et al.*, 2006]. Such large dust devils may play an important role in sustaining the low-level background dust opacity observed during the aphelion season [e.g., *Neubauer*, 1966; *Ryan and Lucich*, 1983; *Smith and Lemmon*, 1999; *Murphy and Nelli*, 2002; *Newman et al.*, 2002; *Balme et al.*, 2003; *Ferri et al.*, 2003; *Basu et al.*, 2004; *Fisher et al.*, 2005; *Kahre et al.*, 2005; *Cantor et al.*, 2006]. MARCI observations can also provide insight into the frequency of dust devil activity during the latter half of the afternoon, bridging the gap between observations made by MGS MOC at 1400 LT and the Mars Odyssey THEMIS instrument [*Christensen et al.*, 2004] at 1700 LT, when activity is on the decline [*Murphy and Nelli*, 2002].

[24] Larger dust lifting events (dust storms) have been reported in all seasons on Mars from ground-based and spacecraft observations [e.g., *Gifford*, 1964; *Briggs and Leovy*, 1974; *Peterfreund and Kieffer*, 1979; *Peterfreund*, 1985; *Zurek*, 1982; *Martin and Zurek*, 1993; *Zurek and Martin*, 1993; *McKim*, 1996; *Cantor et al.*, 2001; *Cantor*, 2003, 2007a, 2007b; B. A. Cantor, Present-day aeolian sedimentation of Mars from an orbital perspective, paper presented at 2005 Annual Meeting, Geological Society of America, Salt Lake City, Utah, 16–19 October, 2005] and across much of the planet. Global observations based on MGS MOC images have shown that storms occur almost daily, with thousands occurring each Mars year [*Cantor et al.*, 2001; *Cantor*, 2003, 2007a, 2007b; *Cantor and Malin*, 2007]. However, only a few tens of these storms become the larger "regional" storms [*Cantor et al.*, 2001; *Cantor*, 2007a, 2007b] and in the rarest of cases (seven confirmed events in the 20th century) these storms may generate the largest of Martian dust phenomena, the "planet-encircling" dust event [*Miyamoto*, 1957; *Slipher*, 1962; *Martin*, 1974a, 1974b, 1976; *Briggs et al.*, 1979; *Thorpe*, 1979; *Ryan and Sharman*, 1981; *Martin and Zurek*, 1993; *Zurek and Martin*, 1993; *Smith et al.*, 2002; *Cantor et al.*, 2002; *Cantor*, 2007a, 2007b; *Strausberg et al.*, 2005; *Cantor and Malin*, 2007]. In each hemisphere, there appears to be an annual dust storm cycle, with storms developing in specific locations during certain seasons. The majority of storms develop near the receding seasonal polar cap edge or along the corresponding polar hood boundaries in their respective hemispheres, while other storms develop in the low-lying regions where atmospheric conditions are optimized for dust lifting (e.g., the plains to the east of Olympus and Elysium Mons and Alba Patera, in the Hellas and Argyre Basins, and in Chryse Planitia). MGS MOC WA images showed that most polar storms formed in the late morning hours when boundary layer instabilities would be greatest. However, major questions remain about the diurnal and semidiurnal development of nonpolar local storms (e.g., When do most dust storms form? How long do they last? Do storms show any semidiurnal variation?). The MARCI investigation included plans to operate simultaneously with the MGS MOC experiment to help address these questions by providing global coverage at two different time periods (1400 and 1500 LT). Unfortunately, the MGS was damaged and contact with it was lost on 2 November 2006. The two cameras, MOC WA and MARCI, operated together for only a few weeks (between 24 September 2006 and 17 October 2006) providing observations of the planet twice in the afternoon each day.

2.1.5. Atmospheric Ozone

[25] Ozone (O_3) is created in the Martian atmosphere as a byproduct of the photolysis of the main atmospheric con-

stituent, CO_2. The oxygen trace products of CO_2 photolytic dissociation, O_2 and O, combine through the 3 body reaction $O_2 + O + M \rightarrow O_3 + M$, to form ozone. Trace products of water vapor photolysis, notably OH and HO_2, catalytically mediate the recombination of CO and O_2 to reform CO_2 [*Parkinson and Hunten*, 1972; *McElroy and Donahue*, 1972]. Similarly, these HO_x trace radicals effect the catalytic destruction of Mars ozone, such that water vapor and ozone abundances exhibit strong anticorrelations in space and time. Mariner 9 Ultraviolet Spectrometer (UVS) observations, exploiting the strong Hartley band absorption of ozone over the 250–270 nm wavelength region, provided the first detection of Mars ozone and definition of its variability in season and latitude, and confirmed its association with Mars atmospheric water vapor column variations [*Barth et al.*, 1973]. Strong orbitally forced variations in Mars water vapor saturation altitudes also force corresponding vertical variations in Mars ozone abundances [*Clancy and Nair*, 1996], which have been identified in Mars Express SPICAM ultraviolet stellar occultation profiles [*Lebonnois et al.*, 2006] and modeled in Mars GCM simulations incorporating photochemistry [*Lefèvre et al.*, 2004]. MARCI has two ultraviolet channels, one centered within (260 nm) and the other just longward (320 nm) of the Hartley ozone band absorption, for the specific purpose of mapping Mars ozone optical depths with daily global coverage. The primary objective of these ozone absorption measurements is to characterize the temporal and spatial variations of Mars atmospheric water vapor at moderately high spatial resolution (8 km).

2.2. Surface Studies

2.2.1. Polar Processes

[26] The annual seasonal cycle of the polar caps includes retreat of the seasonal CO_2 frost followed by summer modification of the remaining residual water ice cap. The annual seasonal retreat has been observed during 4 Martian years by the MOC WA cameras in the visible and by MGS/TES in the infrared. While the seasonal retreat is largely repeatable, interannual variability has been noted both in the recession curves and ice cover of the "permanent" ice deposits [*James and Cantor*, 2001; *Benson and James*, 2005; *Malin and Edgett*, 2001; *Snyder Hale et al.*, 2005; *Calvin and Titus*, 2008]. Investigators working with the OMEGA instrument on Mars Express have noted large-scale albedo changes in the residual northern ice deposit and compositional variation in the southern seasonal cap [*Langevin et al.*, 2005, 2007].

[27] Observed in MOC images at roughly 7.5 km/pixel, the seasonal regressions of the polar caps appear to repeat closely from year to year. The average recession curves do not vary greatly, even in response to the major dust storm in the second MOC year [*Benson et al.*, 2006]. However, specific regions in both caps do exhibit year-to-year variability. For example, the Mountains of Mitchel feature in the south polar region responded to the increased opacity of the 2001 dust storm by disappearing roughly 5° of L_s earlier than in 1999 [*Bonev et al.*, 2002]. Certain regions in the north polar perennial cap also display significant interannual differences, such as retreat of high-albedo materials overlying intermediate albedo polar layered deposits, variation in appearance and location of sustained bright patches, and large-scale albedo decreases over the northern summer season [e.g., *Bass et al.*, 2000; *Langevin et al.*, 2005; *Calvin and Titus*, 2008]. These changes have local and global implications for the Martian water cycle. Detailed study of albedo changes on both perennial and annual timescales will help to constrain both the total water budget in exchange between the poles and atmosphere as well as the dynamics of polar layered deposits related to longer-term climate cycles recorded in the stratigraphy. MARCI data will enable the study of large-scale seasonal cap regressions at a higher resolution than has previously been possible, and the more detailed investigation of the behavior of those regions that show variability.

[28] The residual south polar cap is one of the most dynamic places on the planet, and the mechanics governing the observed morphological changes are still poorly understood [e.g., *Thomas et al.*, 2005]. The stratigraphy suggests erosional differences related to deposition of different units, and that the erosion must also be controlled by insolation, composition, and aeolian effects. *Paige and Ingersoll* [1985] and other observers have reported that the albedo of the seasonal south polar cap increases in response to increased insolation. Indeed, the stability of the residual cap appears to depend on the time dependent albedo in the residual cap region convolved with the insolation. The wavelength dependence of the polar cap albedo in the visible region is sensitive to the amounts of dust and water incorporated in the cap [e.g., *Hansen*, 1999]. MARCI observations can help to constrain the dust content of surface layers as well as to monitor atmospheric dynamics that may contribute to scarp retreat and modification of depressions in the upper residual CO_2 ice surface.

[29] It has been suggested that polar dynamics may be related to the sporadic occurrence of planet encircling dust events [*James et al.*, 1987]. The one planet-encircling dust event seen by MGS started at roughly autumnal equinox, when the south polar seasonal cap was very large and insolation was low. This storm had only local effects on the cap regression during the following spring-summer season. However, the effects of a storm occurring during the perihelion season, as occurred in the summer of 2007, could be very different. MARCI coverage allows us to contrast these two events and their impact on seasonal cap regression, and the appearance and modification of permanent ice deposits.

2.2.2. Regional Albedo Features

[30] The current lack of widespread fluvial or volcanic activity on Mars makes eolian transport of sediment the primary agent of surficial change. Earth- and spacecraft-based observations have revealed numerous variable albedo features [e.g., *Slipher*, 1962; *James et al.*, 1996; *Malin and Edgett*, 2001] that are attributed to redistribution of bright dust on the surface [*Thomas and Veverka*, 1979; *Lee et al.*, 1982; *Thomas et al.*, 2003]. Long-term atmospheric dust transport may also be responsible for massive sediment deposits, particularly in the polar regions where condensation of volatiles may lead to rapid deposition of suspended dust. Regional dust storms and occasional planet-encircling dust events readily provide the sediment source needed to create or sustain these various features. Investigation of Martian eolian processes and features requires an understanding of details of regional sediment transport, as well as the location, genesis, timing, and frequency of large dust-raising events [e.g., *Kahn et al.*, 1992].

[31] Previous studies have demonstrated that variations in regional albedo patterns are indicative of eolian sediment transport through a region [*Lee et al.*, 1982, 1994; *Kahn et al.*, 1992]. Experimental studies [*Wells et al.*, 1984] show that small amounts of dust deposited/eroded from the surface can explain the observed surface albedo changes. Indeed, the presence of only a few microns of dust can alter the albedo by several tens of percent [e.g., *Fischer and Pieters*, 1993; *Johnson and Grundy*, 2001]. The colors of Martian albedo features can also be related to variable amounts of dust cover [e.g., *Soderblom et al.*, 1978; *Singer and McCord*, 1979; *McCord et al.*, 1982a, 1982b]. Visual data are therefore diagnostic of net erosion or deposition of dust storm fallout that is taking place currently.

[32] Global mapping of Mars, begun by Viking and continued using cameras aboard HST and MGS, has revealed many examples of variability in regional albedo features over the course of these spacecraft observations [e.g., *James and Lee*, 1999; *Bell et al.*, 1999; *Malin and Edgett*, 2001; *Geissler*, 2005; *Szwast et al.*, 2006; *Cantor*, 2007a]. Between 1999 and 2006 (over 4 Martian years), the MGS MOC returned daily sequences of images that covered the entire illuminated surface of Mars. Regional albedo changes were observed throughout the course of the MGS observations [e.g., *Geissler*, 2005], and mapping the continued variability of surface albedo features is a major goal for MARCI surface studies.

[33] The accumulated historical evidence (ground-based, spacecraft, and HST observations) indicates that a great deal of seasonal and interannual variability exists in eolian activity on Mars, although repeatable observations have been difficult prior to the MGS and Mars Odyssey missions. For example, previous observations have revealed a great deal of interannual variability in the timing, location, and extent of dust storms [*Slipher*, 1962; *Zurek*, 1982; *Martin*, 1984; *Peterfreund*, 1985], but global observations gathered over the duration of the MGS mission strongly suggest year-to-year repeatability of dust storms and weather patterns [*Cantor*, 2003, 2007a, 2007b; *Cantor and Malin*, 2007]. While the basic distribution, season of formation, effective wind directions, and perhaps meteorological conditions involved in the formation of variable features have been documented with previous observations, the actual conditions of dust entrainment and deposition related to these features have remained elusive. The orbit and payload of MRO is particularly well suited to provide the detailed temporal, spatial, and multiwavelength studies needed to significantly advance understanding of these processes.

2.2.3. Surface Color Properties and Mineralogic Constraints

[34] The visible wavelength color of the Martian surface is controlled primarily by the presence of iron-bearing, potentially hydrated minerals in either ferric (Fe^{3+}) or ferrous (Fe^{2+}) oxidation states. Previous telescopic, orbital, and surface remote sensing (near infrared and infrared) as well as in situ studies have allowed many of these specific minerals to be identified. For example, nanophase (X-ray amorphous) and crystalline hematite (α-Fe_2O_3) have been identified on Mars at telescopic, orbiter, and lander/rover spatial scales [e.g., *Bell et al.*, 1990; *Christensen et al.*, 2000a; *Klingelhöfer et al.*, 2004; *Morris et al.*, 2006]. Goethite (α-FeOOH) has been firmly identified from surface rover observations [*Morris et al.*, 2006] and tentatively identified from orbital measurements [e.g., *Geissler et al.*, 1993; *Kirkland and Herr*, 2000]. Ferric-bearing sulfates and hydrates have also been identified from in situ surface measurements [e.g., *Klingelhöfer et al.*, 2004; *Morris et al.*, 2006], and these phases as well as phyllosilicates have been identified from orbital remote sensing data sets [e.g., *Poulet et al.*, 2005; *Gendrin et al.*, 2005; *Langevin et al.*, 2005]. The ferrous silicates olivine, pyroxene, and ilmenite ($FeTiO_3$) and the ferric-ferrous oxide magnetite ($Fe^{2+}Fe_2^{3+}O_4$) have also been directly detected in surface observations [e.g., *Klingelhöfer et al.*, 2004; *Morris et al.*, 2006], with olivine and pyroxene having been detected and mapped previously from decades of telescopic and orbital remote sensing studies [e.g., *Adams and McCord*, 1969; *Singer et al.*, 1979; *Christensen et al.*, 2000b; *Bandfield*, 2002; *Hoefen et al.*, 2003; *Bibring et al.*, 2005].

[35] Detection and mapping of the distribution and abundances of these primary and secondary mineral phases on Mars has direct bearing on the study of the planet's past and present surface environmental conditions, on the magnitude and duration of putative "climate changes" on Mars, and on the overall issue of the planet's past and present habitability. Surface compositional studies in this area were an important part of the original MCO MARCI investigation [*Malin et al.*, 2001], lost in 1999. A goal of the MRO MARCI investigation is to address many of the original MARCI's surface composition/mineralogy goals [*Malin et al.*, 2001], but at a broader spatial scale and with slightly different wavelength coverage. Specifically, the MRO MARCI five-band visible coverage allows for color characterization of surface units as well as basic characterization of the surface as "dusty" or "clean" at spatial scales of about 1 to 10 km/pixel. Spectral parameters such as the red/blue color ratio can serve as a proxy for the strength of near-UV Fe^{3+} electronic transitions and $O^{2-} \rightarrow Fe^{3+}$ charge transfers in surface minerals. In addition, MARCI's filter set could enable the identification of hematite- or goethite-rich surface regions on the basis of the observed presence and intensity of specific Fe^{3+} electronic transitions near 550 nm and 600–650 nm. Conversely, detection of a strong ferric absorption signature at MARCI wavelengths without evidence for specific crystalline ferric oxide/oxyhydroxide bands like these would be an indicator that nanophase ferric oxides dominate the iron mineralogy. Finally, MARCI's filter set should be able to discriminate between ferric-dominated (altered) regions and ferrous-dominated (pristine volcanic) regions on the basis of the magnitude of the visible to near-IR spectral slope and the wavelength of peak reflectance in the red to near IR. In short, MRO MARCI potential mineralogic detection capabilities are similar to those outlined for the precursor MCO MARCI instrument by *Malin et al.* [2001].

[36] Similar visible to near-IR spectral parameterizations and strategies have been used successfully, though at much smaller spatial scales, for orbital measurements from the Mars Odyssey Thermal Emission Imaging System (THEMIS) visible (VIS) camera [e.g., *McConnochie et al.*, 2006; *Bell et al.*, 2008a], the Mars Pathfinder Imager for Mars Pathfinder (IMP) multispectral instrument [e.g., *Morris et al.*, 2000; *Bell et al.*, 2000], and the Mars Exploration Rover Spirit and Opportunity Pancam multispectral instruments [e.g., *Bell et al.*, 2004a, 2004b]. The MGS TES instrument mapped the

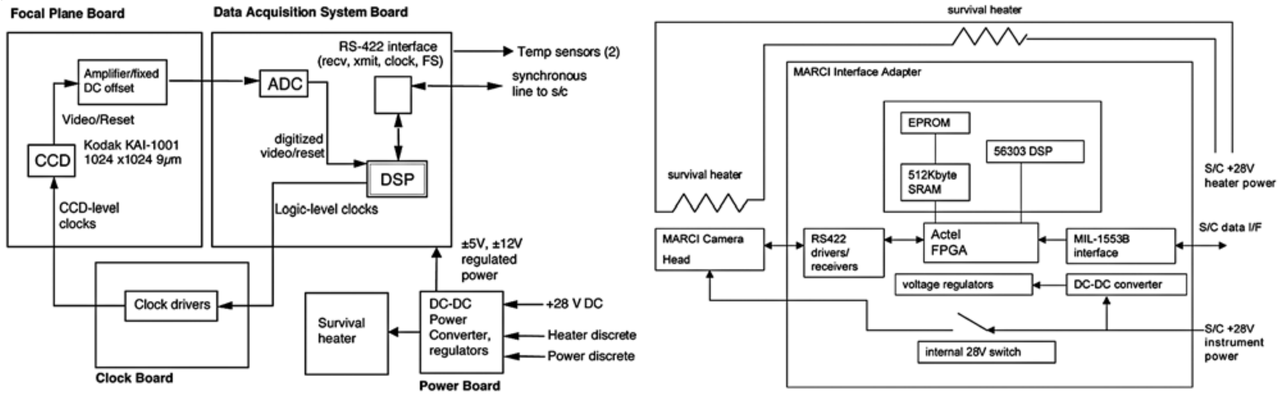

Figure 3. Block diagrams for the (left) MARCI camera head and (right) MARCI Interface Adapter.

surface in the infrared at a scale comparable scale to MRO MARCI, and these data resulted in a number of important discoveries during the past decade [*Christensen et al.*, 2008]. At shorter solar reflectance wavelengths, the Mars Express OMEGA instrument has also mapped much of the planet in the visible to near infrared at several km per pixel scale [*Bibring and Langevin*, 2008], and survey mode data from the MRO Compact Reconnaissance Imaging Spectrometer for Mars (CRISM) instrument are being obtained at comparable (hundreds of meters) scale [*Murchie et al.*, 2007]. The combination of MRO MARCI visible wavelength mapping data, MGS TES thermal infrared, Mars Express OMEGA, and MRO CRISM near-infrared mapping data will thus enable a synergistic, multiwavelength view of the planet's surface mineral inventory.

2.2.4. Surface Physical Properties Constraints

[37] MARCI acquires calibrated radiance measurements of the Martian surface over a wide range of photometric viewing geometries. Each MARCI image spans the entire range of possible emission angles from limb to limb, and the spacecraft orbital track, from south to north over the dayside of the planet, provides coverage over a similarly wide range of incidence angles for typical daily imaging sequences. Laboratory work and previous studies of the spectrophotometric properties of the Martian surface have shown that it is possible to constrain certain physical properties of the surface (e.g., particle size, macroscopic roughness, single-scattering albedo) using such photometric observations [e.g., *Thorpe*, 1982; *de Grenier and Pinet*, 1995; *Guinness et al.*, 1997; *Shkuratov et al.*, 2005; *Soderblom et al.*, 2006]. In addition, such observations could provide new information on the nature of the surface photometric (scattering) function [e.g., *Johnson et al.*, 2008], which is an important but still poorly constrained parameter required for detailed atmospheric correction of Mars remote sensing data sets, as well as retrieval of aerosol physical and radiative properties from telescopic, orbital, and surface-based measurements [e.g., *Wolff et al.*, 1997; *Wolff and Clancy*, 2003].

3. Instrument Description

[38] MARCI is a dual optical path, single focal plane array CCD camera and electronics package (Figure 1) that is

Table 1. MARCI CCD, Optics, and Filter Specifications

Parameter	Value
CCD and Electronics	
Gain (e^-/DN)	26 ± 1
Read noise (e^-)	68 ± 5
Full well (e^-)	46,500 ± 3400
Linearity goodness of fit (r^2)	>0.9999
Visible Optics and Filters	
Focal ratio	*f*/4.3
Focal length	4.0 mm
Field of view (FOV)	180° crosstrack, 26° downtrack
Instantaneous field of view (IFOV)	0.13° (2.3 mrad)
Framelets	16 pixels (2°) downtrack by 1024 pixels (~180°) crosstrack each
Band passes and downlinked detector rows (see also Figure 13 and Table 4)[a]	~425 nm, rows 709–724; ~550 nm, rows 734–749; ~600 nm, rows 760–775; ~650 nm, rows 786–801; ~725 nm, rows 811–826
Minimum focus distance	<0.27 m
Ultraviolet Optics and Filters	
Focal ratio	*f*/7.5 at 260 nm; *f*/7.8 at 317 nm
Focal length	3.8 mm at 260 nm, 4.0 mm at 317 nm
Field of view (FOV)	180° crosstrack, 20° downtrack
Instantaneous field of view (IFOV)	0.13° (2.3 mrad)
Framelets	16 pixels (1.4°) downtrack by 1024 pixels (~180°) crosstrack each
Band passes and downlinked detector rows (see also Figure 13 and Table 4)[a]	~260 nm, rows 266–281; ~320 nm, rows 293–308
Minimum focus distance	<0.02 m

[a] Rows are defined such that row 0 is the closest row to the horizontal readout register.

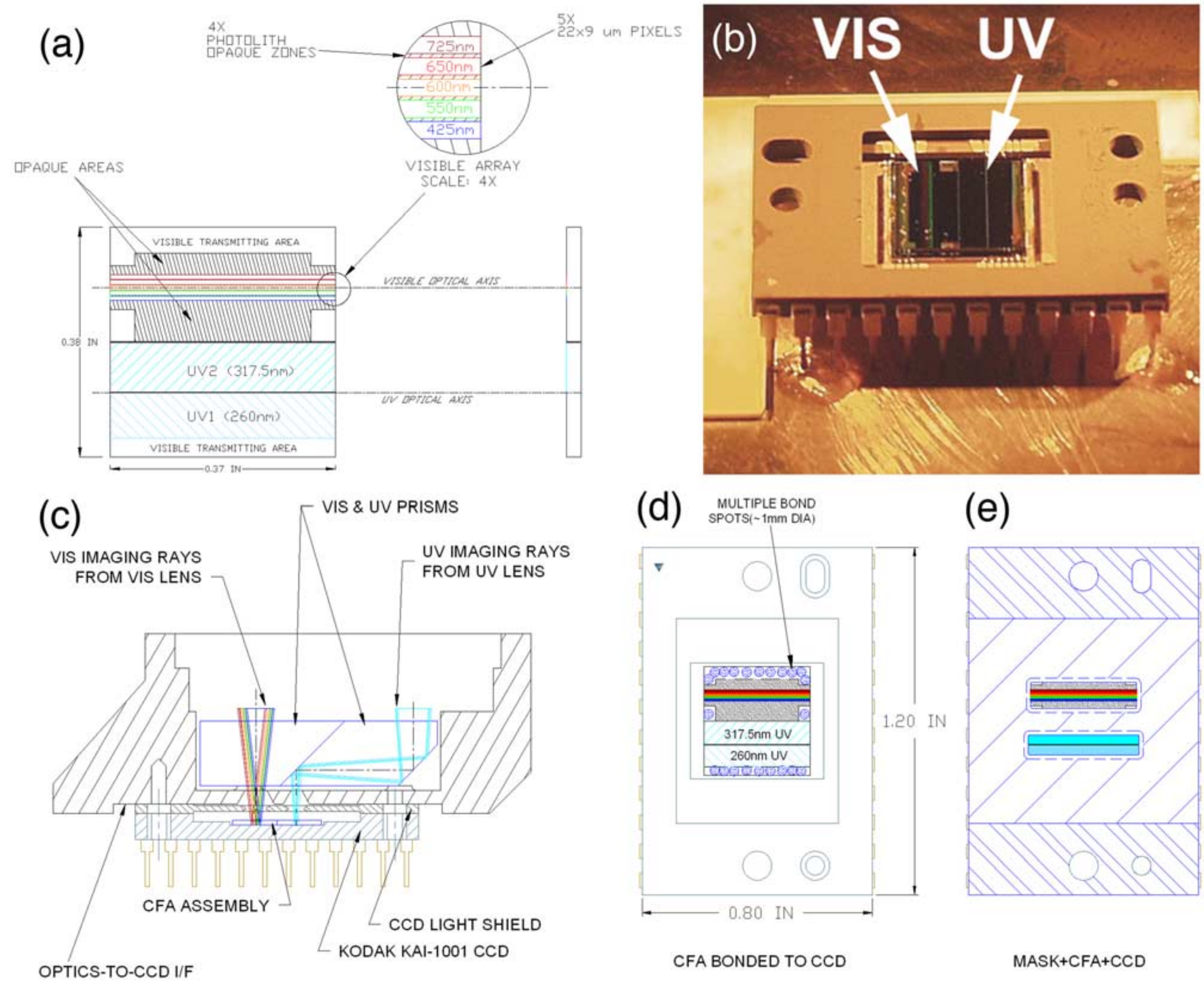

Figure 4. (a) Design of the MARCI VIS and UV color filter arrays (CFAs), which are bonded directly onto the CCD. The VIS CFA uses part of the top half of the CCD, and the UV CFA uses most of the bottom half. The readout of the CCD is from top to bottom in this schematic. (b) Digital camera image of the MARCI focal plane array subassembly. (c) Schematic side view of MARCI VIS and UV light paths, using prisms to redirect the beams from the VIS and UV optics to the appropriate parts of the CCD. (d) MARCI VIS and UV color filter arrays bonded onto the CCD and (e) a schematic of the opaque mask placed on top of the CFAs to help suppress stray/scattered light.

characterized by small physical size (9.2 cm × 7.2 cm × 14.0 cm), low mass (481 g), and low power consumption (<5 W, including power supply losses, when imaging). The two sets of optics have identical wide-angle fields of view (180°), but one set is optimized for performance in the UV (260, 320 nm) and the other set is optimized for performance in the visible to near IR (420, 550, 600, 650, and 750 nm). Table 1 summarizes many of these instrument characteristics. The optical paths are combined onto a single focal plane assembly (FPA) with color filters superimposed on the CCD detector. The instrument also includes a clock board, a data acquisition subsystem (DAS) and a power supply. To match the MRO instrument interface, a separate MARCI Interface Adapter (MIA) box (11.9 cm × 10.4 cm × 3.4 cm, 354 g mass) was designed and provided to the spacecraft. Block diagrams for the MARCI camera head and MIA are shown in Figure 3.

[39] MARCI operates as a "push frame" camera. That is, a color filter array is bonded directly onto the CCD array detector so that each exposure acquires images in different colors over different subsets of the array. Each such single exposure of the entire array is referred to as a "frame," and each subregion of a frame that corresponds to a particular color filter wavelength is referred to as a "framelet." Figure 4 shows schematically the configuration in which each color filter spans approximately the full column width of the CCD array, but only a smaller number of rows. Multispectral coverage of the Martian surface is achieved by using spacecraft ground track motion (approximately parallel to the CCD columns and perpendicular to the long axis of the color filters) to "scan" each filter across the surface as MRO travels from south to north over the dayside of the planet. Complete spatial/spectral coverage is obtained along the ground track by carefully controlling the timing of the frame

exposures in order to ensure adequate overlap of each color band spatially. Subsets of detector rows are selected for downlink in the flight firmware (Table 1). This push frame approach is somewhat similar to the approach used by the Mars Odyssey THEMIS VIS CCD camera to obtain color images of Mars [e.g., *Christensen et al.*, 2004; *McConnochie et al.*, 2006].

3.1. Optics

[40] MRO operations can execute several off-nadir spacecraft rolls per orbit to observe selected targets with the high-resolution imaging instruments of the payload. Global maps produced using the MCO/MARCI's 140° field of view optics would have suffered from a significant loss of coverage as a result of these rolls. To compensate for this, the MRO/MARCI optics were redesigned to increase the field of view to 180°. The commensurate loss of resolution at nadir is partially ameliorated by the lower MRO orbit, such that the MARCI resolution at nadir remains at <1 km/pixel, as on MCO. Compared to the original MCO mission, however, the geometric overlap between swaths is slightly reduced, and thus image quality in these overlap areas is degraded relative to expectations from MCO.

[41] MARCI uses two lenses to cover the desired broad spectral range (UV to near IR) of observations required to meet the investigation goals. One lens covers the UV range only (Figure 1, bottom lens); it is a five element all fused silica lens, designed for optimal performance in the middle of the UV wavelength range of interest. The effective focal length (EFL) of the UV lens varies noticeably with wavelength (Table 1). The visible (VIS) lens uses eight elements made of various radiation-hardened glass substrates (Figure 1, top lens) optimized for the visible bands. The optical paths of the two lenses are coaligned by a prism and parallel plate optical compensator so that all wavelengths are imaged onto a single focal plane array. MARCI UV and VIS optics parameters are summarized in Table 1.

[42] With the new MRO optical design, a few simple changes (relative to the MCO design) were made in order to further enhance performance: the relative Modulation Transfer Function (MTF) of the two channels of the UV lens were optimized for better image quality; external baffling was added to reduce stray light from out-of-field sources, especially from those parts of Mars fore and aft of the area being imaged; and finally, because of concerns about the proximity of spacecraft thrusters to the MARCI unit on the spacecraft's nadir panel, etched foil decontamination heaters and associated control temperature sensors were attached to the MARCI optics. These allow the optics to be heated to remove deposited volatiles, should this ever prove necessary in flight.

3.2. Filters

[43] MARCI uses a filter assembly consisting of two fused silica plates bonded together; one plate has the 5 VIS filters, the second plate has the 2 UV filters. Patterning of the physical shape of the filters (on each plate) was accomplished via a photolithography process during filter coating deposition cycles. The VIS filters are each about 50 nm tall by about 1 cm wide, and the UV filters are about 2 mm tall by about 1 cm wide (Figure 4). Each filter covers the entire cross-track width of the detector but only a fraction of the along-track portion of the detector. Segregation of the UV and VIS light paths and suppression of stray/scattered light in the camera system is aided by an opaque mask placed over the color filter array, with "apertures" cut out for the VIS and UV beams to pass through from their respective optics (Figure 4). Another change from the MCO design was that the UV aperture mask size was decreased, reducing the chance of crosstalk from stray light.

[44] To acquire complete multicolor coverage, consecutive images are taken each time the instrument footprint has advanced by one filter's size in the downtrack direction (see also Figure 23, below). Band selection is accomplished by selectively reading out only part of the resulting frame for transmission to the spacecraft computer. This approach is called push frame or "frame scan." The MARCI visible wavelength (VIS) filter consists of 5 "stripes" each about 20 pixels in along-track extent. The entire detector is read out roughly every 2–3 s. The five band passes were selected near 425, 550, 600, 650, and 725 nm, with band passes of 30–50 nm, to provide good signal-to-noise in scientifically important parts of the spectrum and for continuity with previous and ongoing color observations of Mars. Rejection and passband control were achieved by multilayer dielectric coatings deposited on both surfaces of the fused silica substrates and prism faces. The MARCI UV filters consist of two separate strips, roughly 10 × 2 mm each, that mount near the edge of the detector. Both UV filters are deposited on fused silica substrates. The shortest-wavelength UV filter is centered near 260 nm with a band pass of ~30 nm. The longer-wavelength UV filter is centered near 320 nm with a band pass of ~25 nm. All of the MARCI filters were designed by and procured from Barr Associates in Westford, Massachusetts. Additional specific details on the characteristics of the MARCI filters are provided in section 5.5.

3.3. Camera Electronics

3.3.1. Detector

[45] The heart of the focal plane is a Kodak KAI-1001 Charge-Coupled Device (CCD) detector. This detector has 1024 × 1024 9-μm pixels (1018 × 1008 photoactive, others masked for background/bias signal determination), generates 11-bit output data (0–2047 data number (DN)), and uses interline transfer to implement electronic shuttering. The KAI-1001's fill factor of 20% causes its quantum efficiency to be low, especially at wavelengths beyond 700 nm. These properties combine to make the detector relatively low in sensitivity compared to other possible choices, but the MARCI optics are sufficiently "fast" to allow this compact CCD to be used effectively. In addition, two detector capabilities can reduce the raw data rate from the camera. First, on-chip summing by factors of 2, 4, or 8 can be used to add adjacent lines together in the charge domain under conditions of low signal or low downlink data volume. Second, the CCD's fast-dump feature can be used to read out only selected portions of the detector.

[46] The MCO instrument used Lumogen™ to enhance its detector's UV response. An extensive test program early in the MRO project, however, revealed that the Kodak KAI-1001 CCD has a direct UV response that is competitive with, and in some cases better than, its response with Lumogen™. Without Lumogen™, the filter/detector integration process was considerably simplified. Rather than completely underfilling the filter with optical cement, small spots of cement

bond the filter array at the corners, leaving an air gap of controlled thickness over most of the filter's area.

3.3.2. Clock Generation

[47] The CCD requires seven clock signals: a two-phase vertical clock (V1/V2), a two-phase horizontal clock (H1/H2), a substrate clear clock (S), a reset clock (R), and a fast-dump clock (F). In addition, the analog-to-digital converter (ADC) requires a convert clock. The clocks are generated at logic levels by the digital signal processor (DSP), and are switched at the voltages required by the CCD using discrete P and N-MOSFET transistor pairs. There are two switch timing configurations: one for fast clocks, utilizing discrete HC family logic to synthesize fast one shots, and one for "slow" clocks, which use 74HC4538 integrated circuits.

3.3.3. Analog Signal Processing

[48] The output signal from the CCD is AC coupled and then amplified by a single AD8011 opamp. To bring the amplified signal into the 0–5 V range accepted by the ADC, a fixed DC offset is applied prior to amplification. The resulting AC-coupled signal encompasses half the ADC range: 1.25–3.75 V in the maximum signal condition of all pixels at full well and 0–2.5 V in the case where a small number of pixels are at full well and the rest are near reset.

3.3.4. Digitization

[49] The amplified CCD signal is digitized by an Analog Devices AD1672 ADC running at its maximum rate of 3 Mpixels/sec. For each pixel, both reset and video levels are digitized and then subtracted in the digital domain to perform correlated double sampling (CDS).

3.3.5. Digital Electronics

[50] The digital electronics are responsible for clock generation, sampling of the CCD signal, conversion of the 11-bit samples to 8-bit encoded pixels, storage of the pixels, and finally readout of the pixels to the spacecraft. The DSP in the DAS permits full speed software emulation of much of the usual analog processing, including CDS. Using software emulation, the zero reference ("reset") level for each pixel is digitized and stored in a register. The sum of the video plus zero reference ("video") level is then digitized, and an arithmetic subtraction is performed to produce the final result. The CCD output only requires scaling to the ADC range; no analog sampling, delay or differencing is required.

[51] The Motorola DSP56166 was selected because it can process 3 Mpixels/sec (30 MIPS), incorporates 4 K $\times$ 16-bit data and 2 K $\times$ 16-bit program memory on chip, has two $\leq$15 Mb/sec serial ports that can be used simultaneously for a throughput of $\leq$30 Mb/sec, and its firmware can be booted over these serial lines. For a nominal frame integration period of 0.75 s, it executes up to 20 arithmetic instructions per pixel. These performance characteristics enable this DSP to generate the CCD clocks, read the reset and video levels from the ADC, perform the correlated double sampling subtraction, compand the pixel from 11 to 8 bits, apply lossless (1.7:1) first-difference Huffman compression, and transmit it digitally with handshaking over the communication interface to the MIA.

[52] The DSP clock rate at power up is 10 MHz, supplied by the off-chip oscillator. This rate allows the fixed-rate 2 MHz serial data from the spacecraft to be loaded. Once active, the DSP runs at 60 MHz (30 MIPS) using its internal phase-locked loop. Lower-speed operation can be used to save power in standby and idle periods.

3.3.6. Power Supply and Heater

[53] MARCI uses the Modular Devices MDI2690R-T15 power converter, which produces isolated +5 V and ±15 V from a nominal 28 V input. The ripple on the ±15 V is excessive for the front end video circuitry, so it is down-regulated with series-pass regulators (LP2951 for +12 V and LM2990 for −12 V) to remove ripple. The clock rail and DC bias voltages required by the CCD are generated by source-follower op-amps and zener diodes, as appropriate to the current required.

[54] The survival heaters are etched foil resistive heaters fabricated by Tayco Engineering. They are mounted to the MIA and MARCI camera head. The heaters are sized so that no thermostatic control is required. No additional heating is needed to maintain the instrument at the proper operating temperature.

3.3.7. Instrument Health Assessment

[55] No dedicated internal instrument health monitoring is performed. However, three temperature sensors, two in the camera head and one in the MIA, are monitored by the spacecraft computer. Instrument health diagnostics, including coarse measures of CCD voltage and temperature, are extracted periodically by the science and operations teams from dark current imaging.

3.4. Interface Adapter

[56] A separate subsystem, the MARCI Interface Adapter or MIA, was designed and built to translate the MRO command/data protocol into a form that could be interpreted by the MARCI hardware. MIA provides level shifting between the low-voltage differential signaling (LVDS) interface used by MRO and the RS-422 interface used by MARCI. Using its internal Actel field programmable gate array (FPGA), MIA also translates between the higher-level data protocols used by MARCI and the spacecraft. The MIA and MARCI electronics operate from the same 28V power supply. The MIA mass is 354 g.

3.5. Software

[57] MARCI software runs on two processors: DAS DSP and the main MRO Spacecraft Flight Computer (SFC). The DSP is responsible for generating the CCD clocks, performing the required pixel processing and transmitting the data output to the SFC. The SFC is responsible for instrument operational commands and image postprocessing and compression.

3.5.1. DSP Software

[58] The DSP software is written entirely in assembly language. As indicated previously, it performs all clock generation and pixel processing for the camera. Mission-specific versions of the software have been written to tailor the camera to the capabilities needed.

[59] The MARCI code uses the internal static random access memory (SRAM) space in the DSP for image storage. A double-line buffer scheme allows one line to be read out to the spacecraft while a second is being captured from the CCD. This software also performs spectral band selection, editing, and summing. Summing can be performed either directly on pixel samples or, in cases where the signal is considerably less than the full well, by accumulating multiple lines into the horizontal register before digitization.

Table 2. MARCI Science Team Instrument Calibration and Testing Requirements

ID Number	Requirement
1	It shall be possible to produce radiometrically calibrated images from the MARCI camera observations of Mars, using preflight and in-flight calibration observations.
2	The radiometric calibration of images acquired through the five MARCI visible wavelength filters shall be performed with an absolute accuracy of ≤10%.
3	The radiometric calibration of images acquired through the five MARCI visible wavelength filters shall be performed with a relative (pixel to pixel) accuracy of ≤1%.
4	The signal-to-noise ratio (SNR) of images acquired through the five MARCI visible wavelength filters shall be ≥200 for exposures of at least 50% full well.
5	The radiometric calibration of images acquired through the two MARCI UV wavelength filters shall be performed with an absolute accuracy of ≤10%.
6	The radiometric calibration of images acquired through the two MARCI UV wavelength filters shall be performed with a relative (among 8 × 8 pixel averages) accuracy of ≤1%.
7	The signal-to-noise ratio (SNR) of images acquired through the two MARCI UV wavelength filters shall be ≥70–100, for 5 s integration periods and 8 × 8 pixel averaging.

3.5.2. SFC Software

[60] MARCI performs only minimal command and image processing internally. Using its serial communication line, the camera receives commands, operates upon them, and transmits the results to an external host processor. For MRO, that host processor is the SFC. The SFC is based on a RAD750 processor board (a rad hard derivative of the IBM/Motorola PowerPC architecture) built by BAE Systems.

[61] Higher-level commanding, image processing, and fault protection are provided by instrument-supplied software running in the SFC. The SFC flight software is written in the ANSI C software language for the VxWorks environment provided for the SFC by Lockheed Martin Space Systems (LMSS), the spacecraft manufacturer. It relies on LMSS system services for basic functions such as uplink commanding, downlink data transfer, and communication with instrument hardware. The MARCI version of this code provides internal command sequencing for timed image acquisition and housekeeping functions, image memory allocation, communication with the camera hardware, and image processing. The latter includes additional pixel summing and editing, and both lossless and lossy image data compression. The lossless mode uses a Huffman first-difference scheme; the lossy mode uses a discrete cosine transform operating on 16 × 16 pixel blocks, requantization and zero truncation, and adaptive Huffman compression of remaining coefficients. This compressor was originally developed for the MGS/MOC flight software.

4. MARCI Requirements and Operating Constraints

4.1. Mission and Investigation Requirements

[62] The overall MRO Project science requirements were documented by *Zurek and Smrekar* [2007]; these include a number of science goals specifically identified for the MARCI investigation (see section 1). The MARCI science team translated the achievement of these investigation-specific goals into a set of requirements that would need to be met during design, calibration, testing, and operation of the instrument (Table 2). These requirements were then used to develop a detailed calibration and test plan for MARCI, which included step-by-step procedures for test setups, data acquisition strategies, and, in some cases, data reduction methods.

4.2. Spacecraft and Mission Constraints/Requirements

4.2.1. Power

[63] MARCI uses ±5 V and ±12 V regulated power, provided by its own power supply, and draws 7 W when imaging (<4 W when powered but idle on the night side); unregulated (spacecraft nominal) 28 V power input may also be used.

4.2.2. Thermal

[64] The MARCI operating temperature range is −35°C to +35°C. Survival temperature range is −60°C to +80°C. Once operational, MARCI does not need replacement heat unless powered off.

4.2.3. Mechanical

[65] The MARCI optic axes are parallel to the spacecraft *z* axis (Figure 5), but the camera is clocked around the instrument centerline by 5°, counterclockwise looking into the instrument aperture, in order to reduce field of view (FOV) incursion by MRO spacecraft appendages.

4.2.4. Command

[66] MARCI requires a relatively small number of uplink commands to establish the orbit timing and operational mode (summing and compression) to be used. During normal mapping, the instrument operates as a background task, always collecting data on the sunlit portion of the planet. A few KBytes of uplink a week is sufficient to insure the appropriate observations are being collected.

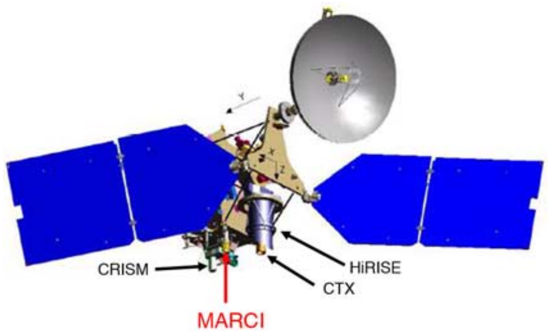

Figure 5. Schematic of the MRO primary science phase mapping configuration, with the spacecraft *x*, *y*, and *z* axes defined and the locations of the nadir-viewing instruments, including MARCI, indicated. See also Figure 5 of *Zurek and Smrekar* [2007].

Table 3. Summary of MARCI and CTX Standalone Camera Calibration and Testing

Test	Brief Description
CCD testing and performance validation	Validate CCD linearity, read noise, full well, gain, bias, and dark current at system level.
Absolute and relative radiometry	Determine conversion between DN and radiance for each filter; measure system noise equivalent spectral radiance at each wavelength.
Flat fields	Determine pixel-to-pixel variability in each filter from observations of a uniform input scene.
System spectral throughput	Determine relative throughput of system over each filter's band pass; also determine rejection band throughput.
Geometric target imaging	Determine effective focal length, field of view, and geometric distortion in all filters.
MTF/point spread function target imaging	Measure MTF and point spread function by observing a target with dots and horizontal, vertical, and diagonal bars of varying thickness/frequency.
Scattered and stray light test	Estimate magnitude of light scattered into the FOV by bright sources outside the FOV.
Observations of geologic samples	Validate calibration by obtaining measurements of known and diverse reflectance sources.
Polarization	Assess magnitude of MARCI/UV polarization sensitivity.

4.2.5. Resolution and Surface Coverage

[67] A MARCI pixel's instantaneous field of view (IFOV) is about 2.3 mrad, which translates to 0.7 km at nadir, and about 4 km at the limb, from an altitude of 300 km.

4.2.6. Predicted Signal-to-Noise Ratios

[68] During the MARCI design phase, the characteristics of the CCD, optics, filters, and electronics were optimized to achieve a required instrumental signal-to-noise ratio (SNR) in each spectral band pass. Predicted SNR was computed assuming observations of low-albedo (0.1) surfaces, at high solar incidence angle (75°; 1700 LT), and under aphelion solar illumination conditions (1.67 AU). For these conditions, the SNR in all five VIS band passes was predicted to exceed SNR of 100:1, the 250 nm UV filter observations were found to require 8 × 8 summing to achieve a SNR of 68:1, and the 330 nm filter was found to require 2 × 2 summing to achieve a SNR of 50:1. Since data rate limitations sometimes require even higher summing factors, SNR for all channels was expected to usually exceed 100:1. MARCI was found to meet or exceed these SNR expectations in actual in-flight performance (section 6).

4.2.7. Data Rates and Volumes

[69] The raw data rate from MARCI is nominally relatively low: 5 bands × 16 lines × 1024 samples × 8 bits/2.6 s readout = 252 Kbps for the visible filters, and 2 bands × 16 lines × 1024 samples × 8 bits/8^2 summing/2.6 s = 1.6 Kbps for the UV filters. Lossless 1.7:1 compression yields total output rates as low as 150 Kbps. Data volumes depend on the number of bands and choice of summing. The flexible nature of the instrument and its software permit the data volume to be tuned to the available allocation, however. For example, a full resolution seven-band, global image can be acquired and downlinked for about 6.2 Gbits/d.

5. MARCI Calibration: Methods and Results

5.1. Preflight Instrument Calibration and Characterization

[70] MARCI calibration and testing prior to MRO launch (12 August 2005) was divided into the following three main activities: (1) component-level testing of individual parts such as the CCD detector, electronics, filters, and optics; (2) standalone camera-level testing of the assembled MARCI camera prior to its integration with the MRO spacecraft; and (3) system-level testing of the MARCI camera after integration with the spacecraft, during the Assembly, Test, and Launch Operations (ATLO) phase of the MRO Project. Here we focus primarily on standalone camera calibration and test results. Component-level testing was primarily used to screen for the highest-quality parts to use during camera fabrication; results from many of those tests on the final flight camera components are described in the MARCI Preflight Calibration Report [*Malin Space Science Systems* (*MSSS*), 2005]. ATLO testing was primarily used to verify camera functionality after critical spacecraft tests like vibration and thermal vacuum testing; a brief summary of the results of those tests is also presented separately in the MARCI Preflight Calibration Report [*MSSS*, 2005].

[71] MARCI standalone camera testing involved configuring the camera such that it had a clear view of several different kinds of illumination sources. These sources included an integrating sphere, a monochromator, and various geometric and geologic targets that were illuminated by external light sources. Table 3 provides a summary of the MARCI standalone camera calibration and test regimen. These tests were performed in a flight hardware qualified optics laboratory at Malin Space Science Systems in San Diego, California.

5.2. CCD Testing and Performance Validation

5.2.1. Gain, Full Well, Read Noise, and Linearity

[72] Important electronics characteristics of a CCD, such as the gain (e^-/DN), full well level (e^-), read noise (e^-), and range of linearity, can be derived by obtaining photon transfer curves (also known as "light transfer curves" or "signal versus noise plots"), using the methods outlined by *Janesick et al.* [1987] and *Bell et al.* [2003]. The data required to assess the linearity, gain, read noise, and full well level of the MARCI detector were obtained by acquiring pairs of images at increasing exposure times from 0 msec to an exposure time corresponding to a signal approximately 20% above visible saturation for all bands. An example data set is shown in Figure 6. The MARCI CCD was found to have an r^2 goodness-of-fit linearity coefficient >0.9999 for data acquired between 10% and 90% of the full well value. Average values for the derived MARCI CCD gain, read noise, and full well from many such tests are reported in Table 1. Because of schedule and budget constraints, most light transfer curves for the MARCI flight CCD had to be acquired at room temperature (20°C–25°C). Thus, our derived average preflight read noise of 68 ± 5 e^- also includes a thermal noise component greater than that which MARCI exhibits in flight, when focal plane array temperatures are much lower (average ≈ -10°C, observed range is about 0°C to -20°C). Detailed procedures for preflight calibration data acquisition are described by *MSSS* [2005]. In-flight verification and validation of MARCI CCD performance is described in section 6.

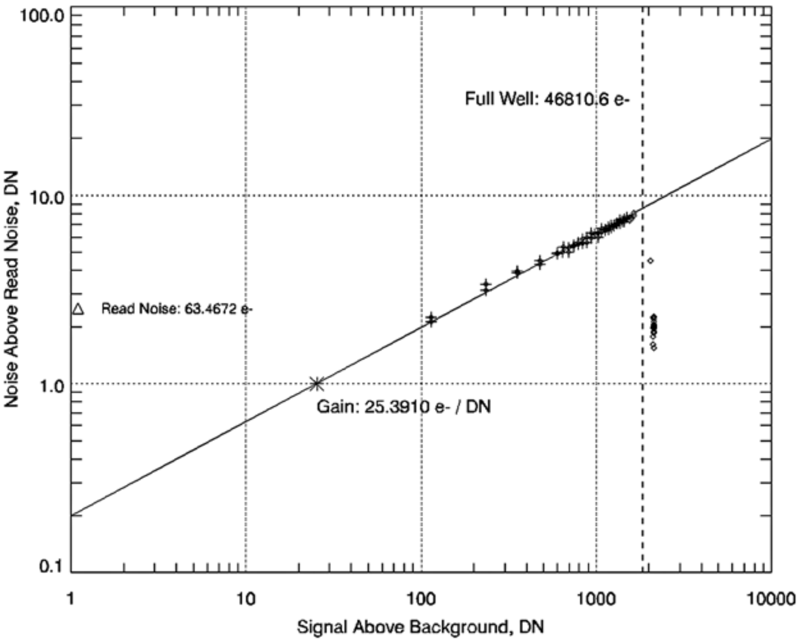

Figure 6. Plot of MARCI bias-removed signal versus noise, from data acquired during room temperature preflight calibration and testing on 30 July 2004. Gain and full well were determined using the method of *Janesick et al.* [1987]. The read noise level was determined from analysis of two zero exposure images. Averages from many such tests were used to generate the MARCI CCD characteristics presented in Table 1.

5.2.2. Bias and Dark Current

[73] CCD detectors typically operate with a bias voltage added to the signal chain to prevent undersaturation (zero DN values) during low-temperature operation. In addition, thermal noise induces electron liberation in most CCDs, producing a temperature-dependent current in the devices even in the absence of illumination. This dark current signal is a function of temperature and exposure time. Characterizing both the bias and dark current levels of a CCD is an important part of calibrating the device.

[74] The MARCI CCD's dark current performance was assessed by acquiring sets of images at increasing exposure times under zero illumination conditions (calibration and room lights off and camera shrouded). Because dark current increases exponentially with temperature, our preflight measurements acquired at room temperature revealed high levels of dark current (generated by the MARCI CCD detector). Even though these levels were much higher than we were expecting to see in flight (on the basis of experience with similar CCDs for the MCO/MARCI and THEMIS VIS instruments), it was still important to acquire these measurements in order to properly remove the dark current signal from our room temperature calibration data.

[75] Interpretation of MARCI preflight dark current measurements has to take into account the fact that dark current in the MARCI CCD detector is accumulated both in the pixel photosites during each integration and in the pixel vertical register transfer sites (V registers) during readout of the CCD. The specific configuration of either the Ground Support Equipment (GSE) or in-flight computer and electronics used to acquire images controls the amount of V register dark that accumulates during exposures. Specifically, when a MARCI mage is commanded, the camera receives the command, integrates for the commanded exposure time, transfers the acquired charge to the V registers on the CCD, waits for a preprogrammed interframe delay or "dwell" time, and then starts the image readout in response to the CCD clocking. Therefore, the time to accumulate dark current in the CCD photosites is the commanded exposure time, and the time to accumulate dark current in the V registers is the dwell minus the exposure time. For MARCI and similar pushframe cameras, the dwell time is a key parameter that can be used to establish a specific percentage of frame-to-frame overlap for each filter's projected footprint on Mars.

[76] To characterize the bias and dark current levels over a more appropriate range of expected operating temperatures for MARCI in flight, however, bias and dark current measurements were also made during a limited set of thermal vacuum tests, over a temperature range from −35°C to +30°C. An example data set is shown in Figure 7. These and other similar thermal vacuum tests reveal no significant levels of dark current in the MARCI CCD below 0°C. They also reveal a very stable bias level for the detector at temperatures below 0°C. These results are consistent with the expectations from component-level vendor data on this model CCD [*MSSS*, 2005]. As described below, these results have also been validated by occasional in-flight bias and dark current monitoring measurements. These test results, combined with the fact that the flight operating temperature of MARCI has been observed to be -10.5 ± 3.7°C over the first ~18 months of operation at Mars (Figure 8), indicate that no special dark current subtraction or temperature-dependent bias removal steps need to be included in the MARCI data reduction pipeline.

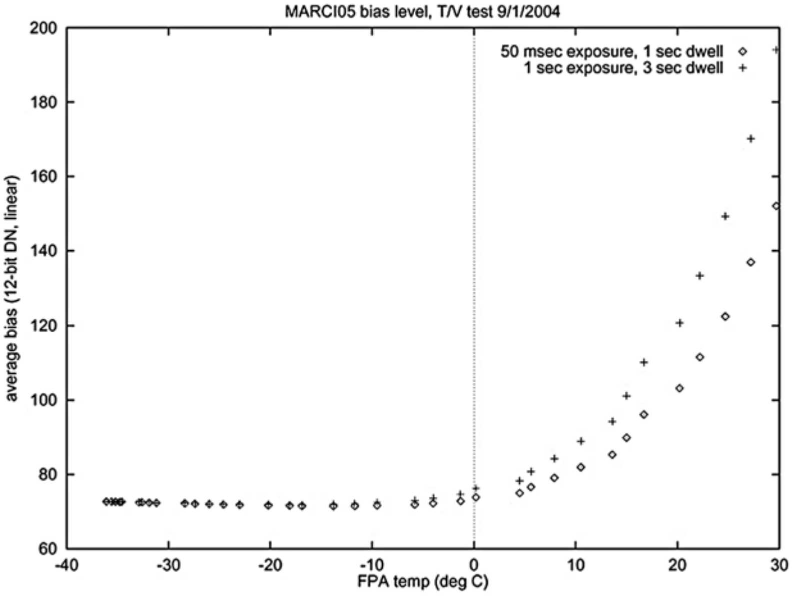

Figure 7. MARCI dark current as a function of temperature, as measured during preflight thermal vacuum testing. Data for two different exposure times/dwell durations are shown; these settings and tests fully bracket the range of exposure times and temperatures that have been experienced during MARCI flight operations to date. The tests reveal no significant dark current accumulation over typical MARCI flight operating conditions.

5.3. Absolute and Relative Radiometry

5.3.1. VIS Filters

[77] The absolute radiometric response of the MARCI visible wavelength filters was measured by imaging the output port of an integrating sphere (Figure 9). A NIST-calibrated Quartz-Halogen (QTH) lamp supplied light to the integrating sphere input port. The radiance output of the integrating sphere and QTH lamp combination was measured by a NIST-certified external vendor using units of W/m^2/μm/sr. We also verified the integrating sphere radiance by using a calibrated photodiode to view the integrating sphere output. For the brightest available lamp setting, the photodiode reading was only 0.5% below that expected from the vendor's sphere radiance calibration. At lower lamp settings, the discrepancy in the photodiode measurements increased, with the photodiode uncertainty

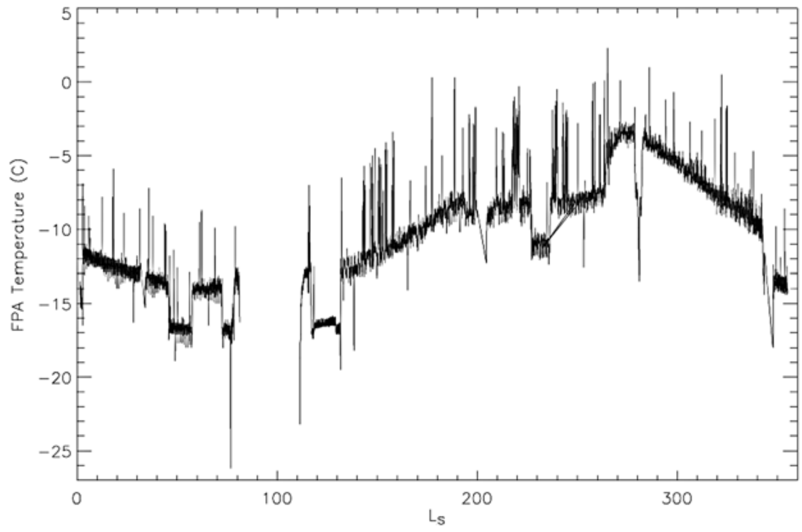

Figure 8. MARCI in-flight focal plane array temperatures versus season (L_s) during the first 18 months of MRO operations. The data follow a generally sinusoidal seasonal curve that correlates with Martian heliocentric distance. The deviation below the expected sinusoidal curve from $L_s \sim 200°$ to $L_s \sim 260°$ is the result of lower atmospheric temperatures during the planet-encircling dust storm of the summer of 2007. Multiday to weeklong temperature drops are a manifestation of different spacecraft-Sun pointing configurations employed during different periods of the mission.

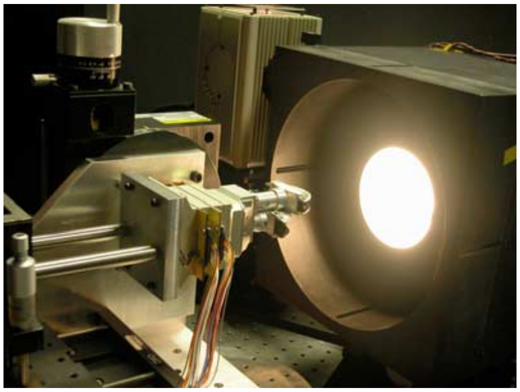

Figure 9. Laboratory setup for MARCI radiometric and flat field measurements. The MARCI detector was approximately 15 cm from the integrating sphere exit port for these measurements. In this orientation, the cross-track direction is horizontal and the visible wavelength channel optics are on the bottom.

increasing to a level of 7.4% below expectation at the lowest useable setting (at 10 times lower radiance than the maximum setting). However, if we assume that the vendor's calibrated sphere + lamp radiances are correct, then the calculated MARCI response per unit radiance is constant to within 0.5% over the order of magnitude in radiance output. Such a result strongly suggests that the vendor sphere radiance data is substantially more accurate than our photodiode-based sphere radiance validation measurements. For this reason, we have adopted the vendor-supplied data as the "known" sphere radiance. Even if we assume that the maximum photodiode validation discrepancy of ∼7% represents a true "error" in the absolute calibration of the input radiance, the result is still well within the science team's absolute calibration accuracy requirement of <10% (Table 2). Additional details and calibration data for the sphere, lamps, and photodiode are provided as part of the ancillary calibration files described by *MSSS* [2005].

[78] For each MARCI VIS set of sphere radiometric measurements, we used a set of exposure times intended to sample the full dynamic range (and somewhat beyond saturation) of all five VIS filters. A bias and dark current image at the appropriate temperature and exposure time was then subtracted from each raw sphere image. The image of the sphere's output port spanned approximately 400 pixels at the center of the MARCI detector (e.g., Figure 10); the MARCI response was calculated by averaging an approximately 10 row by 100 column clean subset of that illuminated area for each filter. A linear fit to the average 11-bit raw data number (DN) as a function of exposure time for each filter and each sphere input radiance setting (discarding measurements with any DN values greater than 1800 to avoid any potential nonlinearity/saturation issues) was used to determine an overall average DN/msec for each set of test observations.

[79] To derive a radiometric response coefficient for each MARCI filter, the "true" radiance value for each set of sphere measurements was assumed to be the vendor-estimated radiance of the sphere weighted by each filter's system response function, determined as described in section 5.5.1. MARCI's "response," then, is simply the overall average DN/msec divided by the assumed true radiance, and thus has units of [(DN/msec)/(W/m^2/μm/sr)]. The current values of these MARCI preflight derived response coefficients are listed in Table 4; additional details and examples of the sphere radiance measurements and linear curve fitting are provided by *MSSS* [2005].

[80] The uncertainties in the MARCI responsivity coefficients were estimated from the scatter of the response coefficients derived from individual tests as the QTH lamp brightness was varied. The radiance incident on MARCI varied over an order of magnitude in the tests used to construct the uncertainty estimates, and the highest radiance used in these tests was similar to that of a bright (nonice) surface region of Mars, observed at the subsolar point and at perihelion. The 420 nm filter exhibits the most uncertainty, with the error being dominated by the observations at the lowest lamp settings. The uncertainty in the 420 nm radiance coefficient would drop by almost a factor of two if we did not include those low lamp measurements. However, to be conservative, we have included these measurements in our overall estimate of the calibration accuracy. The overall level of the absolute radiometric uncertainty determined from our analysis is well within the science team's requirement of absolute calibration accuracy of <10% (Table 2).

5.3.2. UV Filters

[81] The absolute radiometric response of the MARCI UV channels was initially measured in a way very similar to the procedures described above for the visible channels, except for the use of a Xenon calibration lamp source for enhanced mid-UV radiances relative to the limited UV output of the QTH lamp. The absolute radiance of the Xenon lamp/integrating sphere setup was characterized by an external vendor using a NIST traceable diode. However, after instrument delivery, subsequent analysis revealed problems with the initial test setup that called into question the derived UV radiometry. As a result, an observing campaign using simultaneous HST WFPC2 and MARCI observations (of the same locations and photometric angles) was carried out. We provide the details of the observations and the results of the

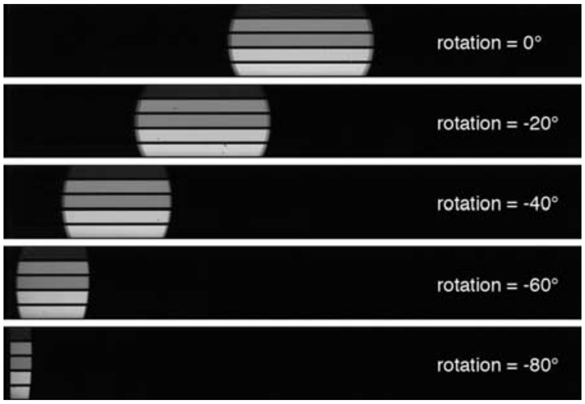

Figure 10. Example MARCI preflight calibration images of the exit port of an integrating sphere, obtained at various rotation angles of the camera (0° is face on directly pointed at the sphere aperture). All of these images were acquired with exposures of 45 msec. The 425 nm filter is at the top, and the 720 nm filter is at the bottom.

Table 4. MARCI Filter Band Passes and Responsivity Coefficients[a]

Band	λ_{eff}[b] (nm)	πF[c] (W/m^2/μm)	R [(DN/msec)/(W/m^2/μm/sr)]
		VIS	
1	437 ± 32	1798.4	0.806 ± 0.024
2	546 ± 40	1875.7	1.124 ± 0.009
3	604 ± 31	1742.7	0.751 ± 0.005
4	653 ± 42	1580.7	0.882 ± 0.006
5	718 ± 50	1360.3	0.777 ± 0.007
		UV[d]	
6	258 ± 30	132.08	$1.15 \times 10^{-2} \pm 0.03 \times 10^{-2}$
7	320 ± 24	755.64	$2.50 \times 10^{-2} \pm 0.04 \times 10^{-2}$

[a] Several of the MARCI responsivity coefficients given here are being reassessed and reevaluated as part of an ongoing calibration process. For updates and details, please consult M. J. Wolff et al. (Ultraviolet dust aerosol properties as observed by MARCI, submitted to *Icarus*, 2009).

[b] Effective wavelength and bandwidth (full width at half maximum; see section 5.5) in nm.

[c] Solar spectral irradiance at 1 AU, from *Wehrli* [1986].

[d] MARCI UV coefficients require the default summing mode of $S = 8$ for equation (4).

subsequent analyses, including the associated radiometric uncertainties, in section 6.4.1.

5.4. Pixel-to-Pixel Nonuniformity (Flat Field) Variations

[82] A major challenge to obtaining flat field observations is to provide uniform illumination across MARCI's 180° field of view. The approach that we adopted was to assume that the exit port of the integrating sphere is a uniformly "flat" field, to illuminate small sections of the MARCI field of view one at a time with this source, and then to assemble a synthetic full field image combining all of the observations.

[83] MARCI was mounted on a rotation stage with the front element of the optics positioned 15 cm from the exit port of the integrating sphere (Figure 9). The rotation stage provided azimuthal rotations; viewed from above, the zero position points the optic axis at the center of the exit port, positive angles denote clockwise rotation, and negative angles denote counterclockwise rotation. The same calibrated QTH or Xenon lamps used for radiometric calibrations discussed above was used to provide illumination of the integrating sphere for the flat field measurements.

5.4.1. Visible Wavelength Flat Fields

[84] Exposures were obtained with the rotation stage positioned at angular increments of 5°, from −80° to +80° azimuth. For each rotational position, separate images were obtained with exposures optimized to obtain maximum signal levels near 1600 DN for each separate filter. Additional bias/dark current frames at these same exposures were obtained prior to and following the illuminated observations; these images were averaged to enable subtraction of mean bias/dark current from each flat field exposure. All images were captured as 11-bit files (DN range 0–2047), with a frame size of 1024 columns × 128 rows, and with the 128 rows selected to encompass only the continuous rows of the CCD corresponding to the bonded on MARCI VIS filter strips. Nine exposures were obtained at each exposure and rotational position. Examples of images obtained at several rotational positions are shown in Figure 10.

[85] For each set of exposures at a given position angle, the nine separate frames were averaged to improve signal-to-noise, and the appropriate averaged bias/dark frame was subtracted. A subset of 16 rows for each filter strip, corresponding to the "Downlinked Detector Rows" entry in Table 1 (referenced to the full 1024 rows of the entire CCD) was extracted for use as each filter's 1024 × 16 flat field segment at that rotation angle orientation. The approach adopted to synthesize a composite "full field of view" image from all of the individual flat field segments was to save the maximum value at each overlapping pixel location found in the averaged flat field segment images from the 33 different orientations of the camera; this ensures the most uniformly illuminated portion of the target is saved into the composite flat field image. Additional details on the MARCI flat field data acquisition and processing are provided by *MSSS* [2005].

[86] To account for any residual nonuniformity in the illumination source, MARCI was then inverted on the rotation stage (with the visible wavelength optics on top), and a complete second set of the same observations was carried out. A second "composite" flat field image was generated as described above. The mean of the two flat field images was generated, and then the composite flat field image was normalized to the mean values of the pixels in a region near the center of each filter strip, yielding the final composite flat field images shown in Figure 11a. Line plots of the average normalized flat field values for each filter (Figure 12) show the response to be fairly smoothly varying across the entire field of view.

[87] The composite flat field image reveals a variety of minor imperfections in the detector/filter system. Figure 11b also shows a contrast-enhanced version of the flat field, with the few "extensive" (encompassing more than a few pixels) blemishes circled. The blemish on the right hand portion of the image shows about a 6% sensitivity increase. All of these flaws are adequately removed, however, as part of the routine "pipeline" processing of MARCI images (discussed below).

5.4.2. Ultraviolet Wavelength Flat Fields

[88] The MARCI UV preflight flat fields were constructed in a very similar fashion as the visible flat fields. Key UV distinctions included the larger filter regions (64 lines each) and significantly longer exposure times. Only 16 lines are read from each of the MARCI UV detector regions in flight, and on-board 8 × 8 pixel averaging reduces the transmitted "line images" to 2 × 128 pixel arrays for each of the MARCI 260 and 320 nm UV channels. Consequently, preflight acquisition of UV flat fields helped to guide the selection of the 16 specific lines to be extracted from the array for imaging in each UV band during MARCI flight operations. In particular, the 16 lines had to be chosen to avoid edge/roll-off effects near the filter boundaries, as well as pinholes and scratches that could generate potential red leaks.

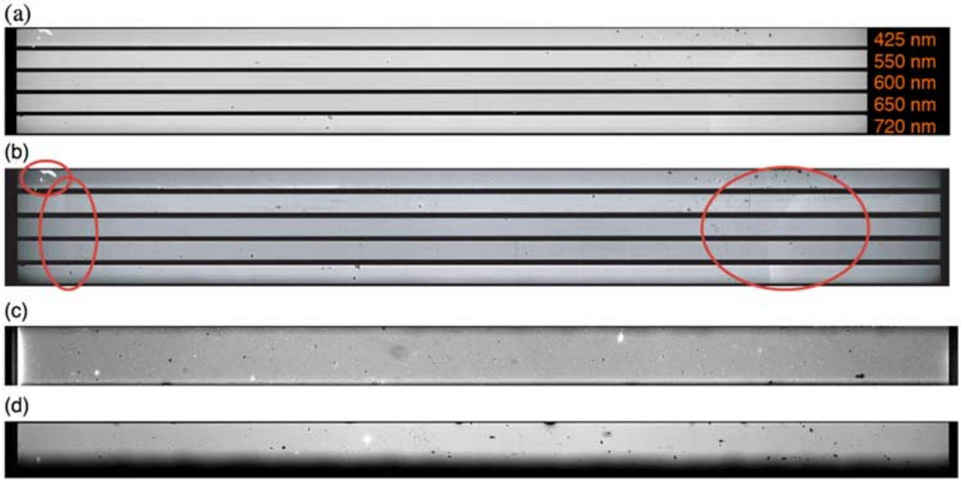

Figure 11. (a) Composite flat field image of MARCI VIS focal plane. (b) Contrast-enhanced version of the composite flat field image of the MARCI VIS focal plane. (c) MARCI UV 260 nm filter flat field image. (d) MARCI UV 320 nm filter flat field image.

[89] Both MARCI UV filter preflight flat fields (Figures 11c and 11d) include spurious bright and dark pixels, several pinhole leaks, and some other large-scale variations. Spurious bright and dark pixels in both channels comprise roughly 1% of the pixel population. Six specific pinholes were identified that range in size from 3 × 3 to 8 × 8 pixels in area. The largest pinhole leaks appear as bright dots in the flat field images in Figures 11c and 11d. Several were unavoidably positioned such that they would always be included in any choice of which specific 16 rows of the UV filters to downlink. Fortunately, as described in more detail below, the effects of these pinholes/potential red leaks have not been debilitating to the scientific utility of the MARCI UV flight data returned from Mars. The resulting MARCI preflight UV flat field image files must be sampled with the same 8 × 8 scheme as used during flight (see below) before they can be used to calibrate raw flight UV images.

5.5. System Spectral Throughput

5.5.1. MARCI VIS Filters

[90] Relative response as a function of wavelength was measured by imaging a monochromator slit through each of the MARCI VIS filters. The monochromator output wavelength was incremented by intervals of 1 nm in the center of each MARCI VIS filter band pass, 2 nm on the wings of the band pass, and 5–20 nm for out-of-band wavelengths. Initial estimates of the limits of the band passes were made using vendor-supplied component-level filter transmissivity curves [*MSSS*, 2005]. Three separate images were acquired and averaged at each monochromator setting. The system response at each wavelength was defined as the ratio of the total integrated signal in a region containing the slit image (after bias, dark, and residual background subtraction) to the measured power output of the monochromator.

[91] The derived relative system response of each MARCI VIS filter is plotted in Figure 13. Out-of-band “leakage” at the camera level (filters plus optics plus CCD) was found to be less than 1% for all of the filters, and less than 0.4% where it could be the most debilitating, in the shortest-wavelength VIS filter. Overall, the filters were found to meet the required specifications for band center, band width, and out of band rejection as defined by the MARCI science team. Additional plots and details regarding both the in-band and out-of-band relative throughput of the MARCI VIS filters is provided by *MSSS* [2005].

5.5.2. MARCI UV Filters

[92] Similar monochromator scans were acquired for the two MARCI UV filters, and their relative response profiles are also plotted in Figure 13. The MARCI UV filters were designed to be optimized with respect to the Hartley ozone absorption band [e.g., *Clancy et al.*, 1996], a distinct improvement over the original MCO/MARCI WA design. Both UV filters were designed and shown by component-level vendor data [*MSSS*, 2005] to exhibit transmission

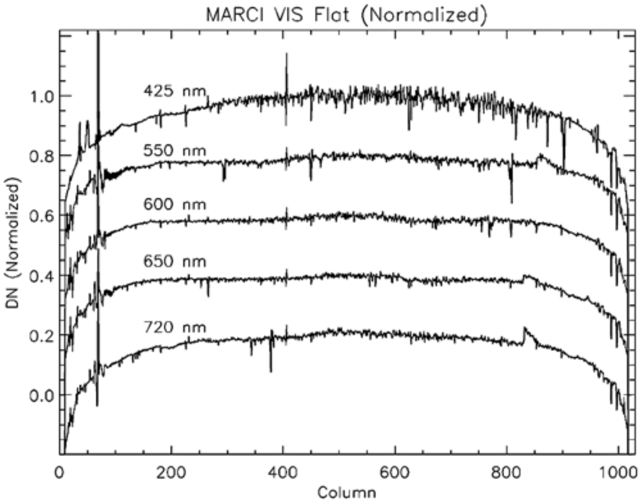

Figure 12. Average profiles across each MARCI VIS filter normalized flat field image. Each plot is offset from the one above it by −0.2. These profiles are from the delta flat corrected in-flight flat field data files (see section 6.3.2) and are essentially indistinguishable from the preflight flat field profiles.

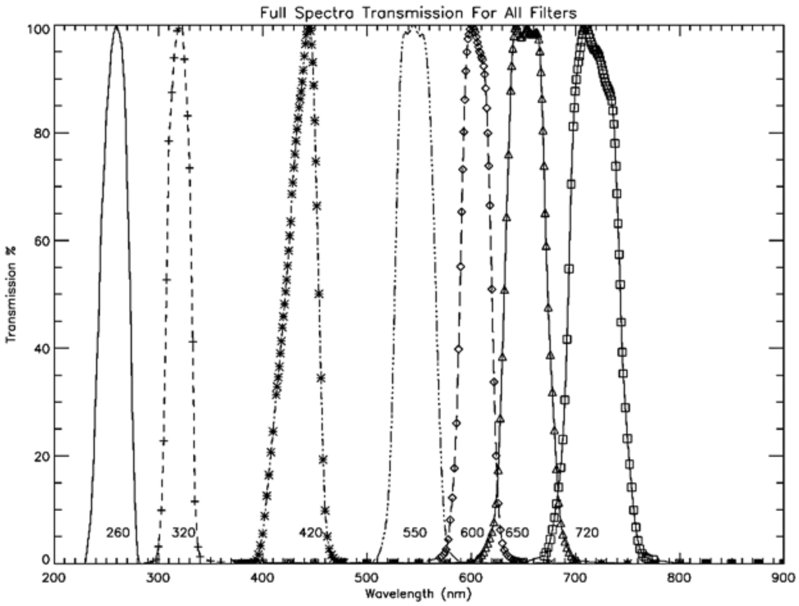

Figure 13. MARCI VIS and UV filter transmission profiles, normalized to 1.0 at their peak values.

decreases >5 orders of magnitude outside the filter band passes. However, because of time and equipment limitations, we were not able to conduct camera level (i.e., including MARCI detector response and optics throughput) MARCI UV out-of-band response measurements comparable to those obtained for the MARCI VIS channels.

[93] Upper limits for potential "red leak" contributions to the MARCI UV channels during Mars imaging operations were thus addressed by two other independent approaches. First, during radiometric calibration testing, relatively coarse upper limits for MARCI UV red leak contributions were obtained with the QTH lamp and a UV cut-off (380 nm) filter placed in front of the integrating sphere entrance port. Integrated red leak contributions to the 260 and 320 nm MARCI channels corresponding to typical Mars bright region radiances were determined to be less than 25% and 3%, respectively. Second, we also placed constraints on potential MARCI UV red leaks using the out-of-band transmission data for the MARCI UV filters provided by the vendor at the component level [*MSSS*, 2005], along with the measured MARCI UV and MARCI VIS radiometric response coefficients and the modeled/expected Mars UV and visible radiances. These calculated upper limits for the red leak contribution to MARCI UV observations at 260 and 320 nm are 8% and 0.5%, respectively, for a typical Mars high-albedo (0.25) region. As discussed below, cruise observations of the Earth and in-flight observations at Mars provide the ultimate empirical test of the magnitude of any red leak in the MARCI UV filters.

5.6. Geometric Target Imaging

[94] Geometric calibration provides a map of angles from a reference direction (i.e., the optical axis) as a function of line and sample in an image. The map is provided by images of targets with known relative angular positions. For many CCD framing cameras, in-flight images of stars are the usual geometric calibration method. However, the resolution and sensitivity of MARCI is such that stellar images during flight are not feasible. We considered imaging of fixed targets covering the 180° field of view during preflight testing, but schedule and budget constraints prevented the construction of such special targets as well as obtaining the measurements required to establish their optical nodal positions.

[95] Instead, we decided to use a collimated light source, with the camera on a two-axis rotation stage, to provide images of a spot (effectively at an infinite range) and thus to map the viewing angles onto the MARCI detector. Each image was obtained at a specified azimuth and elevation of the rotation stage (examples are shown in Figure 14). For each image, a "center of mass" centroid was obtained for each image dot (using software from previous NEAR and Cassini geometric calibration efforts [*Porco et al.*, 2004]). A brief summary of the MARCI geometric calibration results is provided here; for both the MARCI VIS and MARCI UV geometric calibrations, specific additional details on the input data sets, fitting functions, derived geometric coefficients, and residuals to the geometric fits, are provided by *MSSS* [2005].

5.6.1. MARCI VIS Geometric Calibration

[96] The loci of centers from the MARCI visible and ultraviolet images are shown in Figure 15. The convergence of the data at the left and right sides of the image area is a manifestation of the combined azimuth and elevation rotations; the lines are similar to lines of longitude on a globe. For narrow angle imagers, geometric calibration maps are usually made of the tangent of the projected sky angular positions as a function of detector samples and lines. For the extreme wide-angle case of MARCI, however, practical problems arise from fitting to the tangents of large angles. Two separate fitting functions were thus derived here, one for the approximately linear central portion of the field of view (using standard methods from fitting geometric calibration images of stars), and another nonlinear (polynomial) function for the entire field of view. The functional fits were made by comparing predicted with actual pixel locations. The optical center, rotation of the camera, and an effective

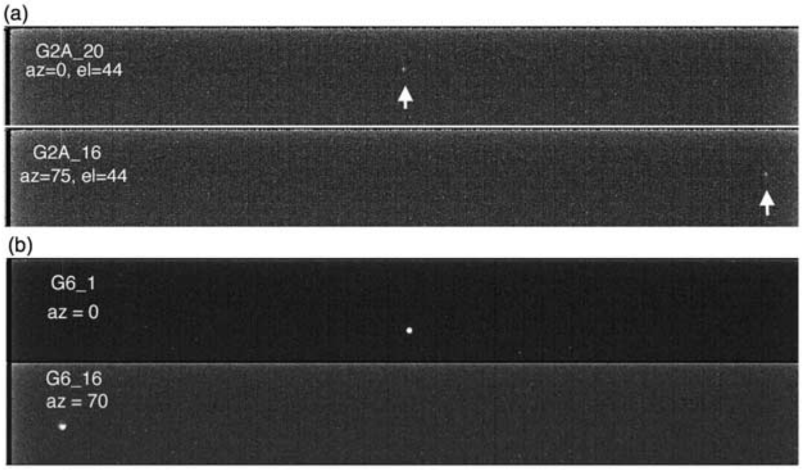

Figure 14. (a) Examples of two MARCI VIS preflight geometric calibration images. Arrows indicate the locations of a collimated (essentially infinitely distant) spot at locations separated by 75° in azimuth. (b) Examples of two preflight MARCI UV geometric calibration images, separated by 70° in azimuth.

focal length, are also fit. With the optical center located, fits were done to test the consistency of the angular measures of the rotation stage. For example, differences in spot locations for identical stage settings are typically 0.0 to 0.02 pixels in the sample direction, and as much as 0.55 pixels in the line direction. The best fit MARCI VIS focal length, assuming 9 μm square pixels, is 3.9 mm for data fit within 10° of the optical axis. However, for such a wide-angle imager, focal length needs to be described for a specific angular range and distortion coefficient. For example, for data fit within 5° of the optical axis, the best fit focal length is 4.2 mm.

5.6.2. MARCI UV Geometric Calibration

[97] The two ultraviolet bands, 260 and 317 nm, were sampled in single elevation sweeps with additional elevation steps for part of the 317 nm filter data (Figure 15). The singular feature of these data is the asymmetric form of the spot in the images (Figure 14b); for large azimuths, the centroiding errors due to asymmetry of the spot pattern are likely to exceed 1 pixel. Nonetheless, an optical center was derived from the data, though with significantly large residuals because of centroiding errors caused by the asymmetries in the spot images. However, the derived geometric functions for the UV filters do fit to within half an 8 × 8 summed UV pixel for angles within about 45° of the center of the field of view.

5.7. Modulation Transfer Function/Point Spread Function Target Imaging

[98] The Modulation Transfer Function (MTF) is a measure of the amplitude response of an imaging system to varying spatial frequencies. In a discretely sampled imaging system, such as MARCI, the natural limit is spatial frequencies that are twice the detector sampling interval (pixel pitch), typically termed the Nyquist frequency.

[99] There are several common ways to measure MTF, including imaging black and white bar targets of varying spatial frequencies, a fixed number of even black and white bars, line sources that are narrower than the pixel dimension stepped across the field, point sources, and canted periodic targets [e.g., *Boreman*, 2001; *Sitter et al.*, 1995; *Guerineau et al.*, 1999].

[100] Each of these approaches have varying levels of procedural and setup complexity, and the MARCI team desired the simplest approach possible using setup and test materials in common with radiometric, geometric, and spectral calibration testing. Given the very wide field of view of the camera, observation of MTF targets was restricted to the central portion of the array. Test targets included vertical bar, horizontal bar, and diagonal bar periodic targets with bar widths of 2.54 cm on 2.54 cm centers. A standard 1956 EIA television resolution test chart was also available with radial variations in line pair per millimeter (lpmm) and circular black and white rings. Each of the periodic bar targets was observed at room temperature for a set of four distances from the MARCI camera: 162.5 cm, 81.3 cm, 40.6 cm (closest in focus), and 20.3 cm (inside focus). Periodic dark current measurements were also made for each exposure level used for the MTF observations.

[101] Because of limitations in the test setup, uniformity of the illumination source, and control on the orientation of the targets with respect to the CCD, as well as the general challenges of working with an ultrawide field of view like MARCI's, the MTF was eventually determined by using each target's black and white edge transition as an individual edge or step function (known as the Edge Spread Function (ESF) [*Boreman*, 2001]). The derivative of the ESF is the line spread function (LSF) of the system, and the magnitude of the Fourier transform of the LSF is equal to the MTF. With this method, each bar target then provides several independent estimates of the system MTF in each filter.

[102] In order to determine MTF, multiple rows in each filter were extracted across each black and white edge, and then averaged to generate an average ESF for each filter and target distance. The ESF data were then used to derive the MTF as described above. Two example MTF curves are shown in Figure 16. The MARCI camera MTF response is typical for a discretely sampled system performing near its diffraction limit. Where response appears to be less than ideal (at low frequencies) it is likely due to deficiencies in the test set up conditions, such as nonuniform target illumination and imperfect orientation of targets. The MARCI visible wavelength optics appear to perform better at higher spatial

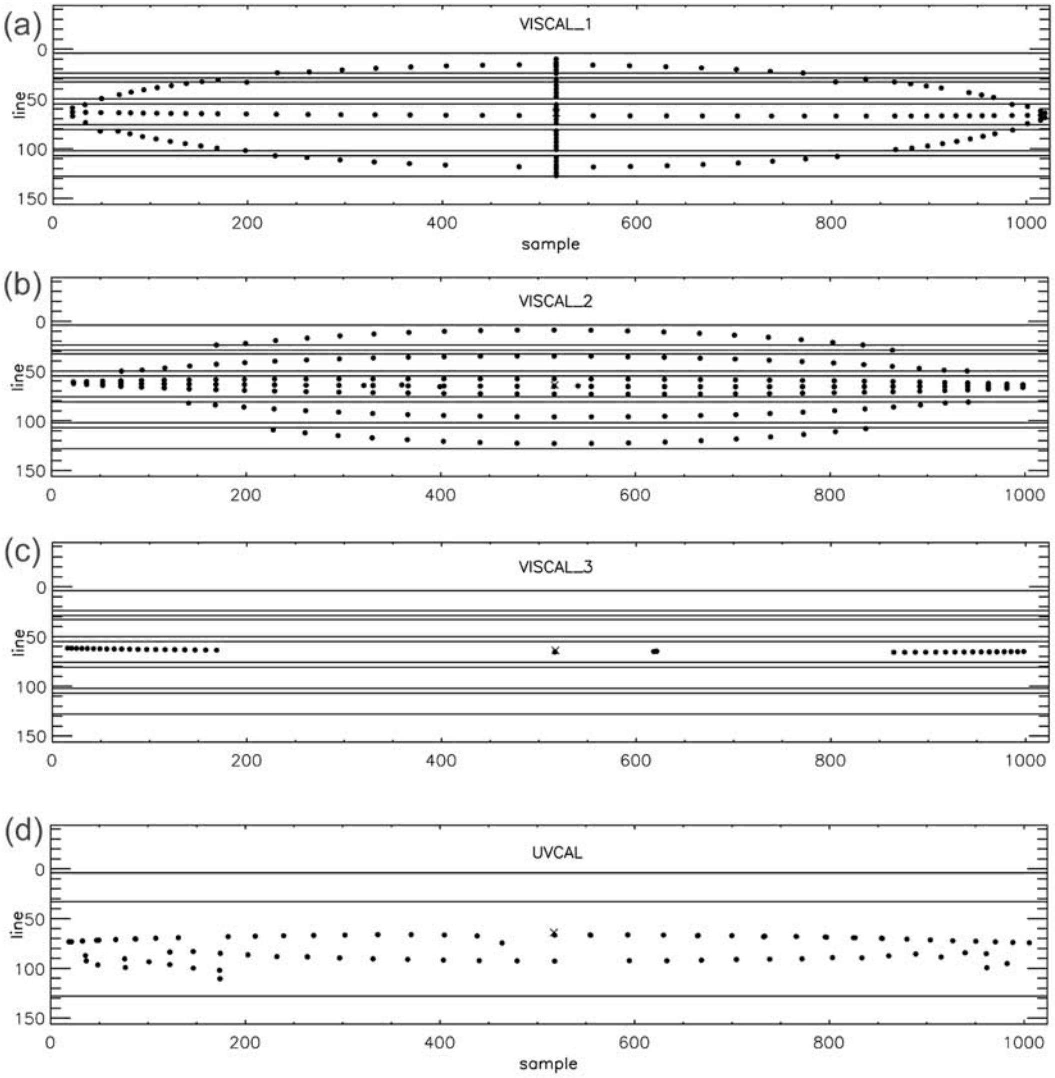

Figure 15. Image locations of geometric calibration points measured for the (a–c) MARCI VIS and (d) MARCI UV filters. MARCI VIS filter boundaries are indicated in Figures 15a–15c.

frequencies, however. There is no significant variation in MTF response with filter wavelength, and comparison of the horizontal and vertical target test results shows no significant variations in MTF with horizontal or vertical directionality on the detector. Much more additional detail on the test setup, data sets, and derived MTF values is provided by *MSSS* [2005].

5.8. Scattered and Stray Light Tests

[103] Preflight, room temperature measurements were obtained to characterize the degree of stray and/or scattered light within the MARCI field of view induced by bright sources just outside the field of view. The 180° field of the MARCI optics made it challenging to design and carry out this test, but a configuration of the camera and light source (zeroth-order white light monochromator exit slit image) was found that allowed a qualitative to semiquantitative assessment of the stray/scattered light component along the axis perpendicular to the filters, or in the spacecraft's along-track direction. Stray light fields of view were predicted on the basis of the optics design to be ~196° crosstrack and ~40° downtrack for both the UV and VIS optics.

[104] In the first set of tests, we oriented a bright source near the center of the MARCI optical axis, but on the lower edge of the field of view. Figure 17a shows an image of the monochromator slit about 2° from the bottom of the MARCI field of view. The lamp current and exposure time were set to allow the slit image to reach a maximum signal level near 1500 DN. Figure 17b shows the result of moving the slit down 2° so that it was just off the edge of the MARCI field of view, and increasing the lamp current and exposure time to massively saturate the slit image (equivalent maximum DN value would be ~8.5 *million* DN). The scattered light pattern can be discerned and the bright source exactly at the edge of the field saturates the region in the bottom filter near the source. The falloff is sharp, however, and the magnitude of the scattered light in the second band from the bottom is only ~0.006% of the peak signal at the edge of the field.

[105] Figure 17c shows the result of moving the ~8.5 × 10^6 DN source to a position 1° further past the edge of the

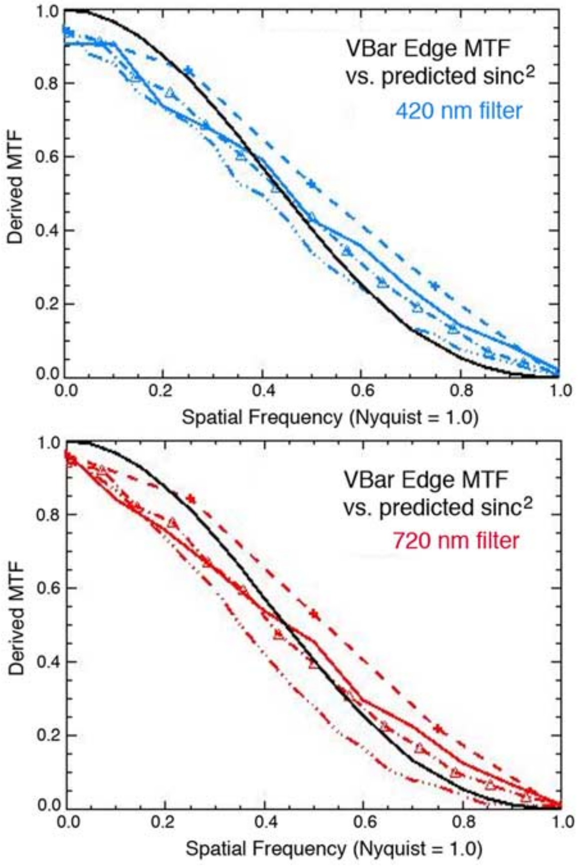

Figure 16. Example derived MTF curves for two MARCI VIS filters ((top) 420 nm and (bottom) 720 nm), on the basis of observations of the vertical black and white bar target. The y axis is derived MTF, and the x axis is spatial frequency, where 1.0 is the Nyquist sampling. The smooth black curve is a $\sin(x)/x$ function, which is the ideal MTF response function for a contiguously sampled system. Different line styles of data represent different target distances, i.e., the MTF at 162.6 cm is the dashed line, the MTF at 81.3 cm is the solid line, the MTF at 40.6 cm (closest to focus) is the dot-dashed line with triangle symbols, and the MTF at 20.3 cm is the dot-dot-dashed line.

field of view. The maximum signal level near the field is ~1300 DN, indicating that the MARCI internal baffles and other stray light suppression design factors have reduced the stray/scattered light component to <0.015% of the just out of field signal level.

[106] Other similar stray light tests showed that comparable levels of stray light suppression are still achieved even if the source is as close as 0.5° off the edge of the field, and that the level of suppression appears to be constant within the ~15° wide region around the center of the field of view that was simplest to test. Measurements of the bright source just off the top of the MARCI field of view indicate that the high level of stray light suppression is vertically symmetric (along-track spacecraft direction). Perhaps the most extreme example of a "problem" that we could identify is shown in Figure 18, with the bright source at the edge of the top of the MARCI field of view. The image shows halo and lens flare-like patterns typical of reflections from multiple lens elements/surfaces and at first glance appears to be problematic. However, the maximum amplitude of the signal in these scattered light components is <0.01% of the intensity of the source at the edge of the field, indicating that these effects should be negligible to undetectable in flight.

[107] We also conducted some tests of a bright source near the limit of the wide-angle field of view of the MARCI VIS optics, ~90° from the center of the optical axis. While not rigorous or definitive because of the challenging geometry of the measurements, we did not see any evidence for problematic reflections or glints in the small number of azimuth and elevation positions that we could sample.

[108] These scattered/stray light test results are not particularly quantitative or robust, but they nonetheless indicate that the design steps taken to maximize the stray/scattered light suppression within the MARCI optics work well under the limited number of stressing cases that we could simulate in our preflight calibration testing. Additional in-flight characterization of stray/scattered light in Mars orbital observations is discussed below.

5.9. Observations of Geologic Samples

[109] Past experience has shown that it can be useful to validate spaceflight instrument performance and the preflight calibration pipeline by obtaining independent observations of reflectance standards and well-characterized geologic samples [e.g., *Bell et al.*, 2003]. Measurements of such materials can then be compared to laboratory measurements to assess the true level of expected uncertainties in the flight data.

[110] Following that philosophy, a set of samples of rocks and NIST-calibrated reflectance and color calibration standards was assembled by collaborator Richard V. Morris (of the NASA Johnson Space Center in Houston, Texas) and mounted to an aluminum plate that could be viewed by the MARCI camera. The specific samples that were chosen for

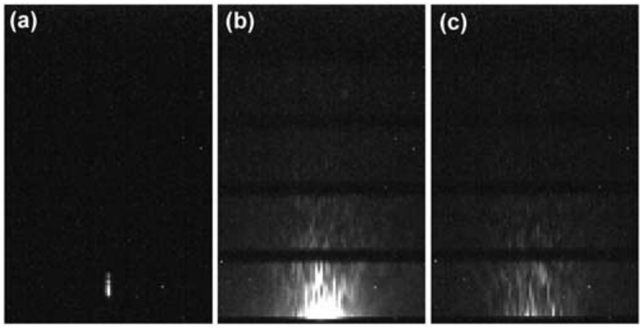

Figure 17. (a) Central portion of a MARCI image, showing the white light ~1500 DN monochromator slit 2° above the bottom of the MARCI field of view, with the lamp and exposure time set to give a maximum signal level of ~1500 DN. (b) Image from the same test, with the slit image moved down to the edge of the field and the lamp level and exposure time set to give an equivalent signal level of ~8.55×10^6 DN. There is some saturation near the source location at the bottom of the field, but the signal in the filter second from bottom is only ~0.006% of the source level. (c) Image from the same test, with the ~8.55×10^6 DN slit image moved down 1° further from the edge of the field. The maximum scattered/stray light signal level in the image is <0.015% of the source level.

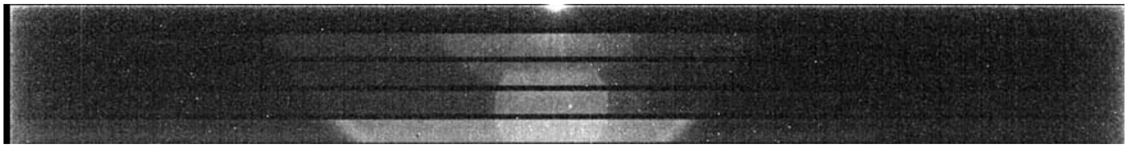

Figure 18. MARCI five framelet preflight test image, showing the stray light pattern induced by placing an extremely bright white light source (equivalent to >3 × 10^6 DN) at the top edge of the center of the field of view. Although the result looks problematic, the maximum magnitude of the stray light signal is <0.01% of the out of field source signal.

this validation study were selected because they exhibit spectral variations that should be detectable and quantifiable in the MARCI wavelength range. In addition, some of the samples exhibit small-scale spatial variations that also serve as a real-world test of the resolution capabilities of the camera system. An example MARCI color image of the test samples is shown in Figure 19, compared to a commercial digital camera image of the same scene. More details on the target configuration and data processing are given by *MSSS* [2005]. Overall, these kinds of imaging measurements verified that MARCI would be able to obtain outstanding color images in flight.

5.10. Polarization

[111] The wide-angle field of view of MARCI incorporates increasing observational sensitivity to the polarization of the incident radiance for views >40° from the optical axis. This behavior is effectively corrected for most MARCI VIS imaging objectives, associated with weakly to unpolarized radiation (such as that coming from the surface), by the application of the MARCI flat fields. Consequently, definition of polarization properties for MARCI does not constitute a standard calibration product for pipeline processing of MARCI VIS images. However, this information does need to be incorporated in the radiative transfer (RT) analysis of the MARCI UV atmospheric radiances. At UV wavelengths, Rayleigh scattering from the molecular atmosphere of Mars contributes significant polarization to the observed Mars radiation field (aerosols and surface contributions contribute much weaker polarization effects). The polarization of the observed Rayleigh scattering is a function of phase angle, and the proportional contribution of Rayleigh scattering will depend on emission angle, viewed surface elevation and dust/cloud aerosol optical depths. Thus, the MARCI UV sensitivity to polarization orientation needed to be characterized in preflight testing in order for that sensitivity to be factored in to scientific analysis of atmospheric aerosol observations.

[112] The MARCI UV polarization calibration employed the Xenon lamp with a linear polarizing transmission filter mounted on a rotation stage in front of the integrating sphere exit port. The polarizing filter was a Sheet Polarizer on a UV fused silica substrate that provides linearly polarized throughput in the UV independent of the incident angle of illumination. The polarizer was sequentially imaged in three rotation orientations separated by 60°, and the MARCI field of view was stepped across the polarizer/exit port in 10° azimuth increments. In addition to viewing this polarization setup with the MARCI camera, we used the same calibration photodiode used for the radiance calibrations described above to establish the polarization of the emergent radiation from the polarizer/exit port setup for the 3 rotation positions of the polarizer. The ratios of diode response among the polarization orientations remained unity (±2%) for emission angles within ±50° (well beyond polarizer emission angles viewed in the MARCI polarization setup), affirming the validity of the setup for accurate characterization of the MARCI polarization properties.

[113] Figure 20 presents the sensitivity of the MARCI UV 260 and 320 nm channels to polarization of incident light as a function of camera azimuth angle (angular distance from the optical axis across the MARCI field of view). Pol1, pol2, and pol3 refer to 0°, 60°, and 120° counterclockwise rotations of the polarizing filter, where a 0° orientation corresponds to linear polarization in the horizontal plane of measurement

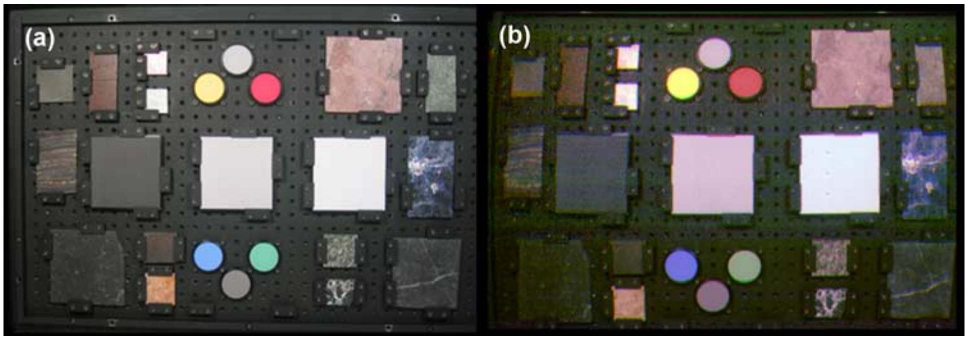

Figure 19. Images of the rock and standards plate imaged during preflight calibration tests. (a) Commercial digital camera image of the target; (b) RGB composite of MARCI wide-angle 600, 530, 423 nm filter images under the same lighting and from approximately the same distance and orientation. The noisier appearance of the MARCI image is a result of high MARCI CCD dark current during these long-exposure, room temperature measurements.

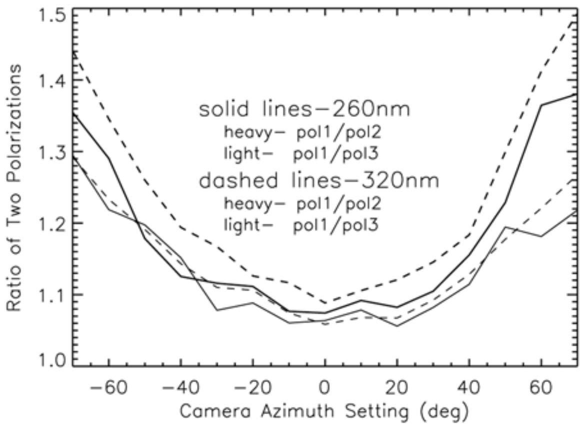

Figure 20. Angular (azimuthal) dependence of the MARCI polarization characteristics, from the repeated (9 August 2004) calibration observations. The three polarization orientations (pol1, pol2, pol3) refer to 0°, 60°, and 120° rotations of the polarizing filter. Thick lines show the ratio of the UV (dashed lines are 320 nm and solid lines are 260 nm) images of the exit port for the first and second polarization orientations, and thin lines show the ratio of the UV (dashed lines are 320 nm and solid lines are 260 nm) images of the first and third polarization orientations.

(i.e., parallel to the long axis of the MARCI lens). The polarization sensitivity is represented by two ratios of the three linear polarization orientations, pol1/pol2 (heavy lines) and pol1/pol3 (light lines). The two MARCI UV channels are distinguished by solid (260 nm) and dashed (320 nm) lines. The variation of the two polarization ratios in camera azimuth (i.e., emission angle in Mars orbit imaging) and the enhanced throughput of the pol1 orientation with respect to the pol2 and pol3 orientations of polarization are consistent with the wide-angle optical design of MARCI. Minimum polarization sensitivity (5–10%) is present near the optical axis, increasing to 25–45% at the limits of the MARCI field of view. Throughput is maximized for the pol1 orientation of polarization, for which reflection at the lens face should be minimized. The positive and negative emission angle behavior is fairly symmetric, with ~5% differences that appear to be opposite in sign for the pol1/pol2 and pol1/pol3 polarization ratios. These measurements provide the data needed to fit smooth polynomials to these polarization dependences and to account for the effects of polarization in the radiative transfer-based retrieval analysis of MARCI UV imaging.

6. In-Flight Instrument Performance, Calibration, and Validation

[114] MARCI has proven to take excellent images of Mars in all seven of its spectral band passes. Exposure times for images in individual filters can be set to reach signal levels of 1500–1600 DN, which, on the basis of the gain and noise characteristics of the array (Table 1), meet the science team's 200:1 instrumental SNR requirement (Table 2). For more typical multispectral image sequences that acquire all 5 visible wavelength filters at once, using average image exposure times (10–20 msec) over average Martian bright regions yields raw signal levels with maxima near 1200 to 1600 DN in band 4 (653 nm) and minima near 200 to 300 DN in band 1 (437 nm). Thus, typical five-band MARCI VIS multispectral imaging sequences exhibit a wide range of instrumental SNR levels, from about 70 in the blue to over 200 in the shortwave near infrared. As a result of the longer exposure time for the UV frames, a similar scene produces SNR levels of about 70 and 110 for band 6 (260 nm) and band 7 (320 nm), respectively.

[115] A number of specific MARCI performance characterization and calibration/validation observations were acquired during the MRO spacecraft's cruise to Mars, after the MRO Mars orbit insertion (which occurred on 10 March 2006) and aerobraking, and then periodically during the mission's primary science phase (which began in November 2006). These observations, an overview of which is provided in Table 5, provide important data for the verification that MARCI is continuing to meet its measurement requirements postlaunch and in flight. Such measurements also allow for validation of the preflight instrument calibration pipeline, afford data needed to modify the preflight calibration for in-flight operations, and, in the event of changes in instrument performance, furnish the critical new data with which one can recalibrate the instrument. These sequences are also crucial for cross-platform comparison between instruments on a variety of other Earth and Mars orbital missions, thus establishing a radiometric baseline that spans across many Mars years (e.g., needed to observe surface changes with time, etc.).

6.1. Postlaunch Earth and Moon Observations

6.1.1. Visible Wavelength Observations

[116] Postlaunch observations of the Earth and Moon were a high priority for the MARCI investigation, as they provided the first means to assess whether there were any changes in the instrument's postlaunch sensitivity, as well as the first observations of radiometric reference sources for validation of preflight radiometric calibration coefficients. MARCI observed the Earth and Moon 3 days after launch (15 August 2005), when the spacecraft was ~1.17 million km from the Earth and ~1.44 million km from the Moon. At this range, the Earth was only expected to subtend ~5 pixels in the MARCI VIS field of view, and the Moon less than one pixel. Summing of the UV channels by 8 × 8 pixels meant that the Earth would be less than one pixel in the UV filters and the Moon would likely not be detectable.

[117] MARCI observations of the Earth and Moon through all seven filters were acquired by slewing the MRO spacecraft across the region of space that contained these bodies, and acquiring a set of timed observations as they passed across each MARCI filter. The Earth was detected in all of the MARCI VIS filters, but appeared only in the 320 nm MARCI UV filter (this was as expected; the large amount of ozone in our planet's atmosphere causes the Earth to be quite dark in the ozone-optimized 260 nm filter). The MARCI Earth/Moon imaging sequence data are archived online in the NASA PDS in data files CRU_000001_9999_MA_99N999W.IMG (VIS data) and CRU_000001_9999_MU_99N999W.IMG (UV data), downloadable from http://pds-imaging.jpl.nasa.gov/data/mro/mars_reconnaissance_orbiter/marci/mrom_0001/data/. Additional details and an animation of the sequence of observations can also be found online at

Table 5. MARCI In-Flight Calibration and Test Observations

Date	Observations/Purpose
15 Aug. 2005	Launch + 3 days; MARCI UV integrations on Earth and Moon primarily to determine red leak in the 260 filter and potential radiometric calibration, plus MARCI Visible filter observations of Earth and Moon. For details, see section 6.1 and also http://www.msss.com/mro/marci/images/2005/08/19/index.html.
30 Aug. 2005	Launch + 18 days; MARCI bias and dark current imaging. See section 6.2.
24 Mar. 2006	Postorbit insertion MARCI instrument check out sequence. For examples and details, see http://www.msss.com/mro/marci/images/2006/04/13/.
9–10 Nov. 2006	Flat fields; near beginning of primary mission phase mapping orbit. A 90° slew about the z axis so that the MARCI line array is oriented along the velocity direction. Wide field of view requires repeat of observation at various roll angles. See section 6.3.
11 Dec. 2006	Stray light analysis; near beginning of the primary mission phase mapping orbit. Slew from dark space to the planet's limb and back to dark space for stray light analysis. Repeat after each Mars year for instrument drift monitoring. See section 6.5.
23 and 27 Jul. 2007	Simultaneous observations by MARCI and HST WFPC2. See section 6.4.
Nov. 2006–2008	Primary science phase bias and dark current characterization: Monthly nightside MARCI imaging sequences to monitor CCD bias and dark current levels (see section 6.2).

http://www.msss.com/mro/marci/images/2005/08/19/index.html.

[118] To find the response (DN/msec) for the Earth in each MARCI VIS filter, the individual Earth images at each time step were analyzed with aperture photometry methods. Specifically, images of the Earth were individually examined by calculating the sum of the DN values inside a box aperture target surrounding each ~5 pixel wide image of the planet. We tested box sizes between 1 and 15 pixels in area, depending on whether the Earth was at, near, or far from the edge of each filter as the spacecraft slewed. Ultimately, small aperture boxes only 2–3 pixels in size, centered on the brightest part of the Earth image, were found to yield the highest-quality data. A similar nearby box of the same number of pixels was used to provide data on the background pixel sum for each Earth image. The same procedure was then repeated for the Moon targets and Moon target backgrounds, but the boxes in this case were only 1 pixel in size. Plots of each target's pixel sum versus the target number within each separate MARCI VIS filter image were used to isolate only data with the Earth or Moon completely within a filter's field of view. Unfortunately, because of the nature of the slew and the specific spacecraft pointing constraints at the time of these observations, the Earth was only partially visible in band 1 (420 nm) and the Moon was not visible in bands 1 or 2 (420 nm and 550 nm). Nonetheless, we estimated the band 1 Earth aperture sum value as the final value observed in the data set in band 1. We subtracted the background (bias, dark) from each of the target aperture sums using the sums from the nearby background boxes and then averaged these "corrected" values to get an average corrected pixel value per Earth or Moon target. The averages were then divided by 10 msec (the exposure time of all the images) to get the average corrected DN/msec values for the Earth and Moon for all of the filters in which they were observed.

[119] To estimate the predicted radiance for Earth in each filter during the time of these observations, we convolved the solar flux at Earth [*Wehrli*, 1986] over the MARCI VIS band passes and assumed the following: (1) a constant albedo for the Earth of 0.3 (soil and sea are dark, around 0.1, and clouds and snow are bright, around 0.5), loosely supported by Galileo Solid State Imager (SSI) estimates of Earth *I*/*F* values obtained during the 1990 and 1992 Earth flybys [*Geissler et al.*, 1995]; and (2) that Earth completely fills each of the pixels in the boxes used to estimate the average DN/msec values. To estimate the whole disk radiance of the Earth, I, in each MARCI filter in units of W/m^2/μ m/sr, we used the following approach:

$$I = [F_{\text{sun}}/\pi], \tag{1}$$

where F_{sun} is the solar irradiance value convolved over each MARCI VIS filter band pass, and division by π converts the radiance to irradiance under the assumption that the MARCI VIS pixels are completely filled by a uniform Earth. Note that the right side of equation (1) would need to be multiplied by 1000 to convert between flux units used in *Wehrli* [1986] and those used for the MARCI VIS radiance coefficients (Table 4). The predicted mean DN/msec pixel value for Earth in each filter was then calculated as

$$\begin{aligned}(\text{DN/msec})_{\text{predicted}} = I\left(\text{W/m}^2/\mu\ \text{m/sr}\right)A_{\text{Earth}}R_{\text{MARCI}} \\ \cdot\left[(\text{DN/msec})/\left(\text{W/m}^2/\mu\ \text{m/sr}\right)\right],\end{aligned} \tag{2}$$

where I is from equation (1), A_{Earth} is the estimated albedo of the Earth (0.3), and R_{MARCI} are the filter responsivity coefficients for the MARCI VIS from Table 4.

[120] Our analysis of the MARCI Moon data followed the same method as that for the Earth observations, with the exception that the Moon was only partially filling one pixel. For this reason, there are far fewer data points for the Moon and the data extracted are highly variable because of the MARCI CCD's 20% pixel fill factor. Generally, to count as a valid "Moon" pixel in our analysis, the pixel had to be at least 10 DN above the value of the corresponding background pixel. The calculation of the predicted Moon radiance also followed the same method as for the Earth, with the important exception of the estimated albedo value of the Moon. The whole disk reflectance of the Moon is well documented and modeled for a large variety of wavelengths and phase angles. For example, *Kieffer and Stone* [2005] derive an average reflectance of ~0.1 for the full Moon at the relevant MARCI wavelengths. Near a phase angle of 90° corresponding to the MARCI Moon postlaunch viewing geometry, *Kieffer and Stone* [2005] observe an average reflectance approximately an order of magnitude lower, or

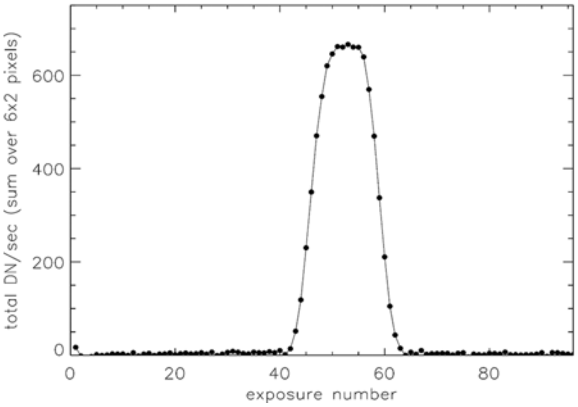

Figure 21. Integrated DN associated with Earth illuminated pixel regions in 320 nm MARCI images acquired 3 days after launch versus image exposure number. Roughly 25 of the 320 nm images contained measurable Earth signal.

around 0.01. Thus, we adopted 0.01 as our estimate of the albedo of the Moon for our estimated radiance calculation.

[121] Using the methods described above, we found that the MARCI VIS derived Earth radiance values were significantly different from the predicted Earth radiances, averaging approximately 40% below the predictions in bands 2 through 5 (the best illuminated bands). However, for the two best illuminated MARCI filter images of the Moon (bands 3 and 4), we find much better agreement with the predicted lunar radiances: band 3 signal was only 4% below the predicted radiance and band 4 signal was only 8% above.

[122] Major sources of uncertainty in the analysis of the MARCI Earth images are as follows:

[123] 1. The estimate of the albedo of the Earth. A value of 0.3 was selected on the basis of typical reflectances of terrestrial materials. However, the Earth was observed at approximately 90° phase angle and the details of the photometric function and any regional albedo variations were not included in this model. A factor of ~2 uncertainty or more between observed and predicted radiances could easily be accommodated just in the lack of knowledge of the Earth's albedo.

[124] 2. Lack of knowledge of the Earth's phase function.

[125] 3. The assumption that the Earth is uniformly filling every MARCI VIS pixel. It may or may not be the case that enough of the Earth was filling enough of each pixel to justify our irradiance to radiance conversion above.

[126] While the discrepancies between the actual and predicted DN/msec values for the Moon are considerably smaller than those for the Earth, the uncertainties in the data itself owing to the highly variable values of the Moon pixels are much higher. The Moon filled only (barely) one MARCI pixel, making accurate analysis difficult, given that the Moon was at most only ~9 DN/msec above background and that the background varied by almost as much. Our assumption of an average lunar albedo of 0.01 at ~90° phase angle could also contribute some fraction of the overall error, given the uncertainties in knowledge of the lunar phase function and the fact that the regions observed by MARCI at this phase angle are not the same regions observed by ground based observers at the same phase angle. Together, these uncertainties could contribute a factor of ~4 or more to the difference between predicted and measured Moon response values. Thus, it is rather remarkable (though perhaps just a coincidence) that the observed lunar radiance is as close to the predicted value as it is.

[127] To summarize the MARCI VIS postlaunch Earth/Moon observations, we consider the fact that observed MARCI Earth and lunar radiances were even within a factor of ~2 of their (highly uncertain) predictions to be at least a reasonable initial flight validation of our preflight derived radiance coefficients. It was also, of course, an excellent early mission demonstration of the ability to point the spacecraft accurately and to perform and end-to-end exercise of the instrument's downlink and data processing pipelines.

6.1.2. UV Wavelength Observations

[128] Postlaunch MARCI imaging observations provided two key results for MARCI UV calibrations: radiometric response of the 320 nm channel, and potential red leak (out of band) contributions in the 260 nm channel. While the Moon was not detected in MARCI UV imaging, the Earth is actually a more appropriate UV calibration target because of the predictability of its UV brightness. Unfortunately, while the Earth was detected, it was not resolved in the postlaunch UV images because the data are summed 8 × 8 pixels (corresponding to 1 UV pixel) performed onboard the spacecraft for MARCI UV imaging. As a result, one must consider irradiance rather than radiance (essentially perform point source photometry rather than that for an extended source). Figure 21 shows the aperture photometry count rates versus exposure number for the 320 nm frames. Although 12 UV pixels are averaged, most of the signal is contained in 2–3 binned (UV) pixels. For the 260 nm data, no Earth signal was identified to within a background uncertainty of 2 DN/sec. This implies a minimal red leak in this channel, as the 260 nm Earth albedo is exceptionally small (260 nm reflectance <0.1% of that at 320 nm) because of Hartley band absorption coupled with very large ozone abundances in the terrestrial middle atmosphere.

[129] For calculation of the predicted terrestrial flux in each of the MARCI UV channels, we employed a DISORT-based multiple scattering radiative transfer code [*Stamnes et al.*, 1988] to a grid of points across the illuminated region of the Earth as viewed during the MARCI observations. Key modeling input parameters included vertical profiles for Rayleigh scattering (scaled to a column extinction optical depth of 1.22 at 300 nm [*Tomasi et al.*, 2005]), ozone density (scaled to a vertical column of 280 Dobson units [*McPeters et al.*, 1998]), and the solar spectral irradiance [*Wehrli*, 1986].

[130] On the basis of comparison of MARCI observed and RT modeled irradiances, we obtained our most accurate determination (prior to Hubble Space Telescope cross calibration observations obtained in 2007; see below) of the 320 nm channel responsivity: 0.0334 [(DN/msec)/(W/m^2/μm/sr)]. The nondetection of a signal in band 6 (260 nm) indicates a <5% out-of-band (red leak) signal for imaging of Mars in this band pass.

6.2. In-Flight Bias and Dark Current Measurements

[131] Initial in-flight MARCI bias and dark current images were acquired as part of the Launch + 3 days

Table 6. MARCI Flight Bias and Dark Current Data Files[a]

Data File	Date	Exposure Time (msec)	Temperature[b] (°C)
T01_000903_1164_MD_00N076W	5 Oct. 2006	25.0	−12.5
P02_001971_1573_MA_00N276W	28 Dec. 2006	25.0	−7.0
P03_002190_1664_MA_00N135W	14 Jan. 2007	25.0	−6.7
P03_002373_1742_MA_00N257W	28 Jan. 2007	25.0	−5.7
P04_002558_1823_MA_00N102W	11 Feb. 2007	25.0	−5.0
P05_002794_1929_MA_00N065W	2 Mar. 2007	25.0	−3.1
P06_003316_2173_MA_00N276W	11 Apr. 2007	25.0	−4.6
P06_003514_2269_MA_00N282W	27 Apr. 2007	25.0	−7.3
P07_003673_2347_MA_00N303W	9 May 2007	17.5	−6.8
P07_003857_2438_MA_00N286W	24 May 2007	17.5	−4.0
P08_003990_2503_MA_00N317W	3 Jun. 2007	17.5	−2.8
P08_004217_2616_MA_00N034W	21 Jun. 2007	17.5	−2.2
P09_004421_2716_MA_00N204W	6 Jul. 2007	17.5	0.1
P09_004567_2787_MA_00N230W	18 Jul. 2007	17.5	−1.7
P09_004715_2858_MA_00N310W	29 Jul. 2007	17.5	1.0
P10_004892_2943_MA_00N103W	12 Aug. 2007	17.5	−1.2
P11_005148_3062_MA_00N252W	1 Sep. 2007	17.5	−2.7
P11_005278_3121_MA_00N201W	11 Sep. 2007	17.5	−3.3
P11_005427_3188_MA_00N309W	23 Sep. 2007	17.5	−2.5
P12_005655_3287_MA_00N054W	11 Oct. 2007	17.5	−4.8
P12_005845_3368_MA_00N201W	25 Oct. 2007	17.5	−5.9
P13_006150_3494_MA_00N248W	18 Nov. 2007	17.5	−9.8
P14_006519_0039_MA_00N243W	17 Dec. 2007	17.5	−8.4
P15_006748_0126_MA_00N016W	4 Jan. 2008	17.5	−7.8
P15_006890_0178_MA_00N293W	15 Jan. 2008	17.5	−7.8
P15_007041_0234_MA_00N096W	27 Jan. 2008	17.5	−8.9
P16_007258_0312_MA_00N261W	13 Feb. 2008	17.5	−8.6
P16_007448_0379_MA_00N049W	27 Feb. 2008	17.5	−9.1
P17_007614_0437_MA_00N262W	11 Mar. 2008	17.5	−9.6
P17_007799_0501_MA_00N274W	26 Mar. 2008	17.5	−12.
P18_007979_0563_MA_00N149W	9 Apr. 2008	17.5	−12.9
P18_008118_0610_MA_00N344W	20 Apr. 2008	17.5	−9.5
P19_008346_0688_MA_00N090W	7 May 2008	17.5	−9.9
P19_008645_0790_MA_00N335W	31 May 2008	17.5	−9.8
P20_008762_0830_MA_00N290W	9 Jun. 2008	17.5	−9.0
P21_009241_0995_MA_00N049W	16 Jul. 2008	17.5	−8.1
P22_009746_1174_MA_00N157W	24 Aug. 2008	17.5	−8.5
P23_009918_1237_MA_00N172W	7 Sep. 2008	17.5	−8.4
P24_010458_1442_MA_00N155W	19 Oct. 2008	17.5	−8.7

[a] See section 6.2.

[b] MARCI focal plane array temperature.

(15 August 2005) Earth and Moon observations described above, as well as a Launch + 18 days (30 August 2005) imaging sequence. Those measurements, conducted at focal plane array temperatures near −11°C, revealed a stable bias level below 1 DN and no evidence for dark current at that temperature and exposure time (10 msec), consistent with preflight expectations.

[132] Additional bias and dark current measurements have been acquired approximately bimonthly during the MRO primary science phase by acquiring MARCI image strips on the night side of the planet. As of October 2008, 40 useable nightside bias/dark sequences have been acquired. Table 6 lists the filenames and other summary information for these primary science phase dark monitoring sequences.

[133] Analysis of MARCI nightside signal levels in the masked-off CCD detector edge pixels reveals that the detector's mean bias + dark current signal level has remained stable and below 1 DN (0.23 ± 0.04 DN) for the duration of the mission to date. In-flight MARCI observations have spanned a range of focal plane array temperatures from about −20°C to +2°C (Figure 8). To date we have not been able to detect any statistically significant bias + dark current signal even at the warmest flight operating temperatures encountered in Mars orbit.

6.3. In-Orbit Flat Field Measurements

[134] We acquired a set of in-orbit MARCI "flat field" measurements to verify the general validity of the preflight flat field functions as well as to provide an improvement or update to those initial calibration products. We found that the low-frequency component of the MARCI flat fields has not changed measurably since the preflight calibration measurements were made, but that significant high-frequency changes had occurred in the MARCI flat field response during flight. These high-frequency changes could be satisfactorily removed using a new set of improved in-flight flat field files. These improvements were generated using a differencing or "delta flat" methodology described below.

[135] The derivation of a MARCI flat field entirely using in-orbit data represented a significant challenge. Because there is no truly flat part of Mars that can be usefully captured by all parts of the CCD during standard observations, a special spacecraft maneuver was needed. The intent of such a maneuver was essentially to provide the same scene for each pixel across a majority of each downlinked image line. The sequence was performed twice: during MRO orbits 1353 and 1355 (9 and 10 November 2006), and orbits 4675 and 4676 (26 July 2007).

Table 7. MARCI Flight Flat Field Data Files[a]

Data File	Date	Exposure Time (msec)	Temperature (°C)	Spacecraft Attitude Details[b]
P01_001353_1330_MA_00N140W	9 Nov. 2006	20.0	−14.8	90° z axis yaw; 50° + x axis roll, return
P01_001353_1330_MU_00N140W	9 Nov. 2006	3122	−14.8	90° z axis yaw; 50° + x axis roll, return
P01_001355_1331_MA_00N194W	10 Nov. 2006	20.0	−13.2	90° z axis yaw only
P01_001355_1331_MU_00N194W	10 Nov. 2006	3122	−13.2	90° z axis yaw only
P09_004675_2839_MA_00N104W	26 Jul. 2007	17.5	−4.0	90° z axis yaw; 60° − x axis roll, return
P09_004675_2839_MU_00N104W	26 Jul. 2007	2525	−4.0	90° z axis yaw; 60° − x axis roll, return
P09_004676_2839_MA_00N131W	26 Jul. 2007	17.5	−2.9	90° z axis yaw; 60° + x axis roll, return
P09_004676_2839_MU_00N131W	26 Jul. 2007	2525	−2.9	90° z axis yaw; 60° + x axis roll, return

[a] See section 6.3.
[b] Compare to Figure 5.

[136] During normal (nadir pointed) MARCI imaging, the yaw angle ("twist" about the nadir-pointed +z axis of the spacecraft; Figure 5) varies by only about ±4° to compensate for planetary ground motion. The MARCI detector is oriented so that during normal imaging operations the detector rows are approximately orthogonal to the ground track motion, thus moving the ground "horizontally" across the detector array (see section 3). For the in-orbit flat field observations, however, the spacecraft attitude was twisted ~90° about the z axis (Figure 5), so that the ground was instead dragged "vertically" across the MARCI detector array. In addition, 40° to 60° rolls in the +x and −x directions were also included on top of that ~90° z axis twist in order to ensure that each edge of the 180° MARCI field of view could be completely illuminated by the planet. Table 7 lists the filenames and other summary information for these in-flight flat field sequences.

6.3.1. Analysis of In-Orbit Flat Field Observations

[137] Analysis of the in-flight flat field measurements requires knowledge of the observational geometry for each pixel. Since the MARCI detector was not precisely aligned with the ground track (i.e., movement of a surface element is not perfectly parallel to the detector x axis), we rely instead upon the reconstructed spacecraft ephemeris data (the so-called "C kernel") to derive pointing information. In order to construct a sample for each pixel with essentially the same atmospheric path length while covering the center to the edge of the detector, we chose pixel values with emergence angles within 5° of the minimum angle observed by a given pixel. This typically corresponds to an observed latitude range of about 40°. Such a relatively large range is less problematic than it might seem in terms of surface features because of the fortuitous presence of a planet encircling dust event during the summer 2007 observations. Unfortunately, the resulting mean incidence angle spans a range of ~15–20°, introducing nontrivial photometric effects. However, by focusing on the central 400 pixels for each line, the drift in incidence (and phase) angle is generally only (at most) ~5°.

[138] Using the uncalibrated images (i.e., no dark or bias correction), a flat field was constructed for the central portion of the detector using the above approach and normalizing each band in the same manner as was done for the preflight flat fields. For the VIS bands, the resulting shapes over the limited detector region chosen are consistent with those of the preflight flat fields within the uncertainties introduced by nonconstant photometric angles. Although not an ideal result in terms of the original goal of the observation, the verification of the general shape of the flat field provides sufficient confidence to now utilize the delta flat methodology described below.

[139] The agreement in the UV is less optimal, which may be due to scattered light effects resulting from the unusual illumination geometry of the camera optics, including associated polarization effects. There is a suggestion of such atypically scattered light effects even in the VIS bands, though this appears confined to the outer ~100 pixels at the edge of the detector. Consequently, given the similarity of the preflight flat field procedure for both the UV and VIS and the general consistency of the VIS flats between preflight and in-orbit measurements, we adopt the UV preflight flat field functions as being adequate for use in the delta flat approach.

6.3.2. Delta Flat Update

[140] Given the potentially debilitating effects of launch vibrations, rapid temperature swings, interplanetary radiation, etc., it would not be unusual to observe changes in the small-scale structure of the instrumental flat field from that determined by prelaunch laboratory measurements. As long as the general low-frequency shape of the flat field function is not changing (as discussed above, it does not appear to have changed in general since the preflight calibration), it is possible to characterize small, high-frequency changes in the flat fields using a simple coaddition approach. Specifically, by averaging of hundreds (or thousands) of MARCI images, one can produce a "mean image" that encapsulates the general low-frequency shape of the flat field, and a corresponding delta flat that can be used to identify small-scale (i.e., on the order of several to a dozen pixels) differences between the preflight and in-flight flat field behavior. This approach has been previously applied to both astronomical and planetary observations where a large number of images are available [e.g., *Kuhn et al.*, 1991; *Lucey et al.*, 1997; *McEwen and Robinson*, 1997].

[141] We calculate an initial mean image for each month of MARCI observations since November 2006 in order to allow for the possibility of on-orbit evolution of the flat field behavior. In addition, we restricted our analysis to the full resolution (unsummed) data in order to avoid issues related to either interpolation or extrapolation of data that were originally acquired in the 1024 × 16 pixel (128 × 2 for the UV) images and prelaunch flat field files. Our method for generating these delta flat improvements to the MARCI preflight flat fields involved the following steps:

[142] 1. Each raw image was processed by subtracting the background level (average value of dark space off the limb), sorting the individual filter image pieces into separate arrays of concatenated framelets for each filter (see details on

image structure in section 7.1), and then dividing each filter's array by the appropriate normalized preflight flat field, framelet by framelet. Each filter's calibrated array is then collapsed to an initial mean image by averaging to a single framelet (1024 × 16 for the VIS filters, 128 × 2 for the UV filters), using a set of DN thresholds chosen to eliminate both low S/N framelets (for example, near the polar terminator) and very bright surface regions (for example, over polar ice). Filtering out anomalously low and high values avoids introducing nonrandom spatial structure into the mean images for each filter.

[143] 2. For all images in each month's sample (typically ~400), the resulting initial mean images from each filter are averaged to produce an overall mean image. A comparison of these monthly mean images for the first fifteen months of the MRO primary science phase did not reveal any convincing evidence of a time dependence in the observed large-scale or small-scale structure. Thus, a new set of proposed in-flight flat field images was constructed from the mean of each filter's overall mean image between November 2006 and January 2008.

[144] 3. If the best possible flat field has been derived via this process, the proposed new in-flight flat field images should be characterized by a smoothly varying function across the array, reflecting the mixture of many kinds of surface terrains, general atmospheric conditions (i.e., dust loading, clouds), and solar illumination geometry. Any small-scale departures from "smooth" must thus represent features that are missing from the original preflight flat fields used in Step 1 above. We quantified such departures by breaking up the 1024 pixel domain into subregions (typically 5 to 7 of them) such that the mean image for each line in the subregion can be well approximated by a polynomial of moderate order, typically sixth degree or less. The degree of the fitting polynomial and the subregion boundaries are chosen interactively in order to avoid the introduction of both the oscillatory structure that is not uncommon with such fitting functions and nontrivial discontinuities between fits of each subregion. Typically, ~75% of the field of view can be covered with two or three polynomial-fit subregions, with the remaining subregions being concentrated near the limbs.

[145] 4. The delta flat is then derived by taking the ratio of the proposed new in-flight mean image and the fitting polynomial, for each subregion. A value of 1.0 in the delta flat array indicates no change from the preflight flat field applied in Step 1.

[146] Because of the subjective nature of Step 3 and the potential to identify "bad pixels" in the process, the above algorithm is iterative. However, the VIS bands have typically required only 3 or 4 iterations. In contrast, the UV bands each required more than twice as many. For an optimum flat field, each line in the mean image (16 for the VIS filters, or 2 for the UV) should be essentially identical. Thus, as part of the above iterative process, we also included a step that looks for multiplicative offsets between the individual lines in the mean images. Visible line-to-line differences could indicate the need for an additional multiplicative correction. This approach generally yielded required additional offsets of less than 1–2% for most of the bands. However, the band 1 (437 nm) flat field was found to contain 2 lines for which this "renormalization" amplitude was about 5%.

[147] New in-flight MARCI flat fields were created by multiplying the original preflight flat field files by the delta flat files created by the above process. While our application is complicated by the wide-angle nature of the camera as well as the fact that Mars has a spatially variable surface and atmosphere, we ultimately benefit from this process because the large amount of input data enabled us to produce very high SNR delta flat corrections. The resulting new flat fields were found to produce a significant improvement in the calibration of the UV data. This is a direct result of the less than ideal SNR levels in the preflight UV flat fields. In the VIS bands, the largest radiometric differences appear in band 1, where the preflight values may be somewhat SNR limited. In general, the application of the new flat field files also produces calibrated images with a noticeably improved appearance for all filters, probably because of the very high SNR of the delta flat process.

6.4. In-Orbit Radiometric Calibration/Validation

6.4.1. HST Cross Calibration

[148] We conducted an imaging campaign using the Hubble Space Telescope (HST) in order to independently derive and validate the preflight absolute calibration of the MARCI UV filters. Our HST observations occurred at two epochs during 2007 (23 and 27 July), when the sub-Earth point on Mars as viewed from HST and the subspacecraft point on Mars as viewed from MRO were nearly coincident. One "orbit" of HST Wide Field Planetary Camera 2 (WFPC2) observations were obtained at each opportunity (HST Director's Discretionary Program #11314). Each HST orbit consisted of four repetitions of three filters in order to allow for uncertainties in the exact timing of MRO's passage through the sub-Earth footprint. The HST filters used, F255W, F336W, and F439W (effective wavelengths 260, 334, and 431 nm), are reasonably well matched to MARCI bands 6, 7, and 1 (effective wavelengths 258, 320, and 437 nm), respectively.

[149] To process these HST images, we first calibrated (to standard radiance units) and geometrically registered the images to an areocentric coordinate system using the techniques described by *Wolff et al.* [1999]. Then the corresponding MARCI images containing the sub-HST point for each epoch were bias subtracted and flat fielded to units of DN/msec and geometrically registered to the same map base as the HST images. HST and MARCI pixels were then correlated to identify pixels from each data set that satisfied the following specific criteria: (1) pixel centroid latitude and longitude within 0.5° and (2) incidence, emission, and phase angles within 3°, 3°, and 4°, respectively. We required a minimum of 5 MARCI pixels for a "match" to be declared for each HST pixel. For each observing epoch, only two of the four filter sequences produced observations that met these requirements. Ultimately, the number of HST pixels included in the sample for each band is approximately 110, 230, and 130 for MARCI bands 6, 7, and 1, respectively.

[150] Next, we derived a band pass transformation between the HST and MARCI filters using synthetic spectra. As a result of the very dusty conditions present in the Martian atmosphere in July 2007, the standard approach of

simply using a spectrum constructed from solar irradiance and a representative surface reflectance is inadequate. Instead, we constructed a radiative transfer model using the optical depths reported by the Mars Exploration Rovers [e.g., *Lemmon et al.*, 2004] and the dust/surface properties and phase functions found by *Wolff et al.* [1999, 2007], respectively. We found that there is not a great deal of sensitivity to the details of the dust models, in that varying the optical depth by a factor of two changes the resulting band pass transformations by less than 3%. The adopted transformations scale the F255W and F336W radiances by 0.85 and 0.82 for MARCI bands 6 and 7, respectively, and for F439W and MARCI band 1 there is less than a 1% difference.

[151] The MARCI radiometric coefficient is then calculated using the direct conversion of transformed WFPC2 radiances and the calibrated MARCI count rates (DN/msec) for the matching pixels. The formal precision is set by standard error propagation of the root-mean-square variance of the matching WFPC2-MARCI pixel sample data set, scaled appropriately. The resulting MARCI band 6 and 7 values may be found in Table 4. For MARCI band 1, the derived value is 0.806 ± 0.024 compared with the original ground calibration value of 0.793. The excellent correspondence between the two band 1 values provides a useful check on the ground calibration radiometry as well as validation of the methodology used in the WFPC2-MARCI cross calibration for the UV filters. Although the formal precision seems quite small, there are systematic accuracy issues which limit the overall uncertainty of the UV radiometry to ~8–10% (band 7) to ~12–15% (band 6). The largest source of this uncertainty is the 8–10% and 3–5% uncertainty in the WFPC2 radiometry for F255W and F336W, respectively [*McMaster and Biretta*, 2008]. This uncertainty should be better characterized (and likely reduced) with the final calibration of the WFPC2 data set associated with the expected end of WFPC2 operations in 2009. Another smaller source of systematic uncertainty is the error associated with the model dependencies of the WFPC2 to MARCI band pass transformation process.

6.4.2. CRISM Comparison

[152] Simultaneous imaging by the MRO CRISM and MARCI instruments provides another excellent opportunity to check the radiometric calibration on MARCI (as well as CRISM). Because of limitations on the CRISM wavelength range and the presence of a significant artifact near 670 nm [*Murchie et al.*, 2007], we focus here only on validation of MARCI bands 2, 3, and 5 (546, 604, and 718 nm).

[153] To begin our validation analysis, we constructed a sample of CRISM radiometrically calibrated spectra (and associated pointing information [cf., *Murchie et al.*, 2007]) by selecting the nadir portion of emission phase function (EPF) sequences taken during the first 5 months of the MRO primary science phase (November 2006 to March 2007). To provide comparable spatial resolution, the CRISM data were summed to be approximately 2 km per spectral "pixel" in the cross-track direction. Then the corresponding MARCI images obtained simultaneously with the relevant CRISM EPF were bias subtracted and flat fielded to units of DN/msec and geometrically registered to the same map base as the CRISM images. Matching CRISM and MARCI pixels were then correlated such that for each CRISM summed pixel, all MARCI pixels with centroids within 2 km were collected. Given the field of view of CRISM, this approach produced photometric angle differences of less than ~0.5°. For a CRISM summed pixel to be further considered, we required that it has at least 3 associated MARCI pixels.

[154] Finally, synthetic photometry was performed on each spatially averaged CRISM spectrum using the system response functions described above. The resulting simulated MARCI radiance was converted to a radiometric scaling coefficient through a simple ratio with the mean of the associated MARCI count rates. We discarded statistical outliers by requiring that points in the final sample be within three standard deviations of the mean radiometric coefficient. This filtering changed the derived coefficients by less than 0.5% for all three MARCI bands; however, this 3σ criterion does reduce the standard deviation of the coefficient sample by about 30–40%. The number of derived coefficients that passed the above criteria was 501, 409, and 482 for bands 2, 3 and 5, respectively.

[155] The resulting MARCI derived radiometric coefficients from this cross-calibration exercise are 1.189 ± 0.064 (band 2), 0.755 ± 0.052 (band 3), and 0.802 ± 0.051 (band 5). Within the quoted precision (i.e., the RMS of the sample defined above), the derived coefficients are in excellent agreement (5.7%, 0.5%, 3.1%, respectively) with those obtained from the preflight ground calibration (Table 4). No time variability was observed in the derived cross-calibration coefficients within the data examined in the first 5 months of the MRO primary science phase. Using Occam's Razor, the excellent correspondance of the CRISM and ground-based MARCI radiometric coefficients would also suggest a CRISM radiometric accuracy of order ~1–3% in the wavelength regions covered by MARCI bands 3 and 5, and only mildly worse (~6%) for the band 2 wavelength region, where the need for a CRISM scattered light correction may partially explain a larger uncertainty [i.e., *Murchie et al.*, 2007].

6.5. In-Flight Scattered and Stray Light Levels

[156] Assessing the contribution of off-axis scattered light in the MARCI field of view during Mars orbital flight operations is extremely difficult because of the 180° field of view of the camera (e.g., slewing Mars completely out of the field of view could essentially mean turning the spacecraft upside down!). However, the off-axis flat field tests described previously in section 6.3 and Table 7 provide at least a partial way of assessing the in-flight scattered light component. Specifically, in images when the planet only fills about half of the instrument's field of view (Figure 22), we find signal levels from scattered light in the unilluminated areas off the limbs to be only ~0.2% to 1.0% of the average illuminated signal level, peaking near band 2 (546 nm), near the maximum of the Sun's radiance combined with the CCD's spectral responsivity. Similarly low scattered light levels are observed in nighttime images at high latitudes, where only part of the sunlit terminator is in the field of view.

[157] A small amount of internal stray light or veiling glare from Mars itself can also be detected in most "normal" MARCI images of Mars, detected as slightly elevated signal levels in the 50 to 70 columns of the detector just off the

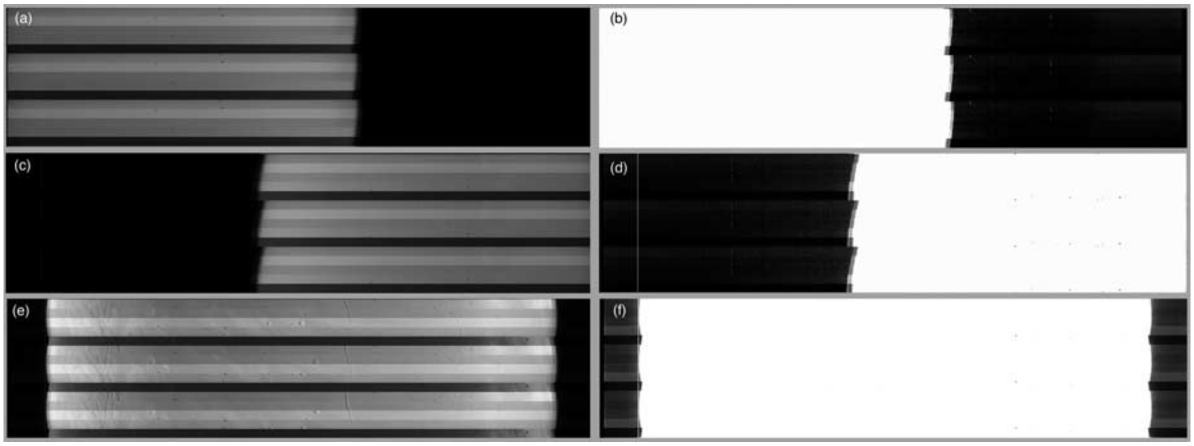

Figure 22. Examples of minor levels of stray light/veiling glare in raw MARCI images. (a) Part of image P09_004675_2839_MA_00N104W, acquired on 26 July 2007 near the maximum ~60° roll of the spacecraft to the right, thus completely illuminating the left side of the MARCI field of view with Mars (see section 6.3 and Figure 5 for details). Three MARCI frames are shown here, each of which consists of five individual multispectral framelets (bands 1–5, from the bottom to the top). (b) Same image as Figure 22a, but harshly stretched to reveal minor levels (<1%) of stray light in the field of view to the right of the Martian limb. (c) Similar to Figure 22a, but from part of MARCI image P09_004676_2839_MA_00N131W, also acquired on 26 July 2007 near the maximum ~60° roll of the spacecraft to the left, thus completely illuminating the right side of the MARCI field of view with Mars. (d) Same image as Figure 22c, but harshly stretched to reveal minor levels of stray light in the field of view to the left of the Martian limb. (e) Part of "normal" nadir-pointed MARCI image P01_001339_1325_MA_00N118W, acquired on 8 November 2006. (f) Same image as Figure 22e, but harshly stretched to reveal minor levels of on-axis stray light in the field of view off both sides of the Martian limbs. See text for details.

planetary limbs on the far left and far right of the field of view (Figure 22). This stray light probably arises from multiple on-axis reflections off the surface of the CCD and the bottom of the glass interference filters and/or other optical elements. The magnitude of the glare ranges from ~1–3% of the average illuminated signal level in each filter. The glare has a reddish color, as expected for stray light from Mars. The small magnitude and diffuse nature of this glare (no discernable features or surface markings can be detected in the glare signal, indicating that it is not simply a focused ghost image) allows for its effective removal from the illuminated data using the "bias subtraction" methods outlined below.

7. MARCI Calibration Pipeline: From Raw Data to *I/F*

7.1. Raw MARCI Images

[158] Raw MARCI images can be obtained from the NASA Planetary Data System (PDS, e.g., http://pds-imaging.jpl.nasa.gov/Admin/resources/cd_mro.html). Detailed documentation on the structure and content of the raw MARCI Experiment Data Records (EDRs) can also be found online from the PDS in the MARCI Software Interface Specifications document (M. Caplinger, Mars Reconnaissance Orbiter: Software interface specification, Mars Color Imager (MARCI) standard data product, Malin Space Science Systems, Inc., available at http://pds-imaging.jpl.nasa.gov/data/mro/mars_reconnaissance_orbiter/marci/mrom_0001/document/marcisis.pdf, 2007), which is stored within the "document" subdirectories associated with each data volume release. Details on the file-naming scheme for the PDS-archived raw MARCI images is provided in Appendix A.

[159] Raw images begin with a text header that identifies various properties of the image and contains a file offset to the data portion of the image. The image data are then appended to the end of the file. Raw MARCI images are a concatenation of the original MARCI frames (single exposures of the entire CCD, but with only the desired filters saved). For a desired summing factor f ($f = 1$, 2, or 4 for the MARCI VIS filters; f always equals 8 for the UV filters), each MARCI frame acquired has $16/f$ lines of image data per selected filter band. Each of those sets of $16/f$ lines is referred to as a *framelet*. Thus, a raw MARCI data file represents the concatenation of frames and their associated framelets acquired during any particular observing sequence, in a format shown graphically in Figure 23. Nadir-pointed MARCI image strips acquire data from limb to limb (covering local times from ~1500 ± 0200 at the equator from MRO's low 300 km orbit) and they can often stretch from pole to pole, spanning of order 100,000 pixels in length (for MARCI VIS). All raw MARCI images are 8-bit data with image dimenion that are multiples of 16 pixels. Data from the MARCI visible wavelength channels (bands 1–5) and UV channels (bands 6, 7; $f = 8$) are stored in separate files because of their dramatically different file sizes.

7.2. Calibration Algorithm

[160] A straightforward set of calculations and image manipulations can be used to convert raw MARCI images into radiometrically calibrated data.

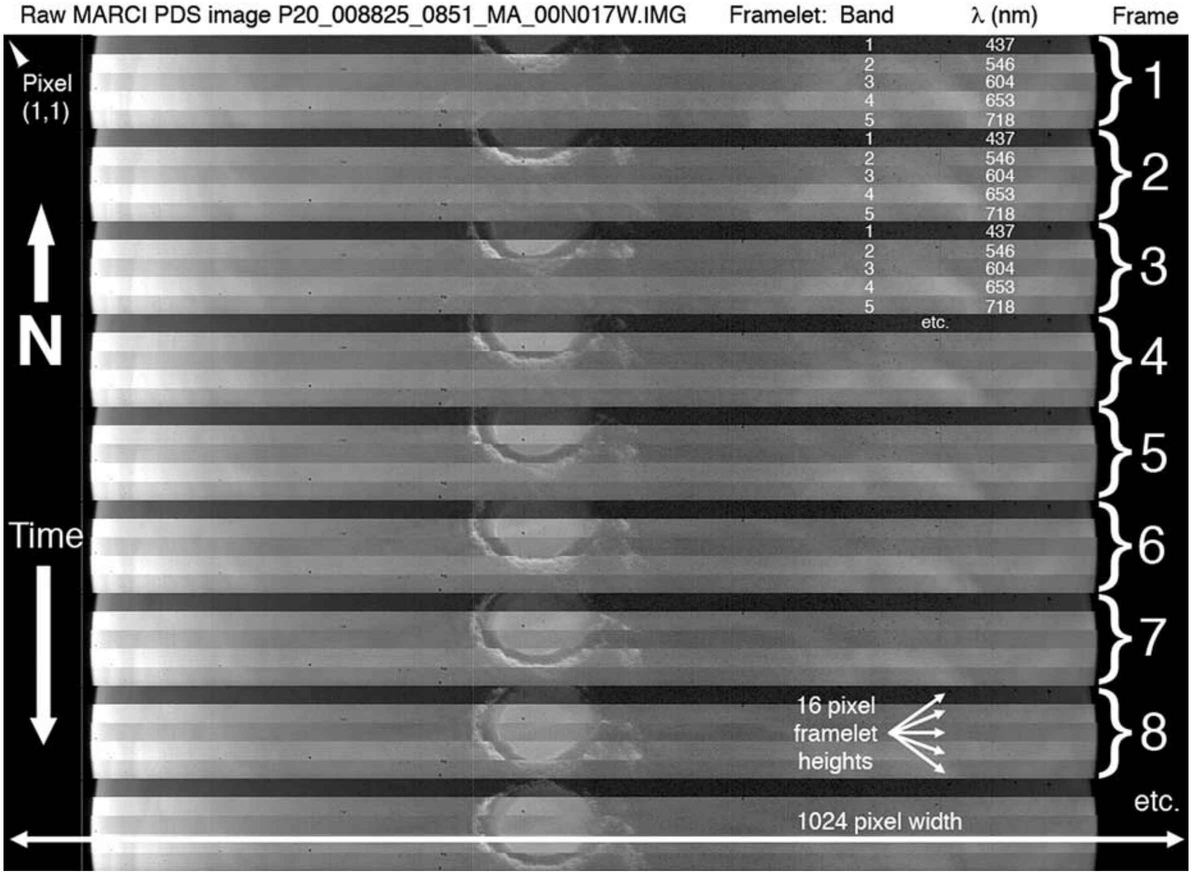

Figure 23. Part of raw MARCI image P20_008825_0851_MA_00N017W, acquired on 14 June 2008. This is a summing mode 1, five-filter visible wavelength imaging sequence. North is up. The full MARCI image from this particular sequence is 105760 rows long by 1024 rows wide. The arrow indicating the position of pixel (1, 1) is for schematic purposes only; the actual pixel number at the top of this image is approximately (1, 91120) in the full MARCI image, corresponding to a high northern latitude on Mars. The ~80 km diameter frost-filled impact crater Korolev can be seen "marching" to the south through each filter framelet, as the MRO spacecraft ground track moves from south to north during the sequence.

7.2.1. Decompanding

[161] All MARCI data are "companded" (a word originating from "compressed, then later expanded") within the instrument electronics from their original 11-bit (0–2047) format to 8-bit (0–255) data files using a square-root-like compression lookup table (LUT). This onboard compression process is designed to prevent shot noise from being encoded into the downlinked data. The MARCI 11–8-bit LUT and the 8–11-bit inverse LUT needed to "decompand" the original data are summarized in Table 8. That information is also available with each MARCI PDS data volume release as a simple ASCII text file called marcidec.txt that is stored within the "calib" subdirectory. To decompand the raw data, each occurrence of the 8-bit value in Table 8 is replaced with its corresponding 11-bit value. Creation of the most efficient version of this onboard data compression scheme required the accurate knowledge of the CCD gain, read noise, and full well acquired during preflight camera testing.

7.2.2. Flat Fielding

[162] Flat field calibration files are available in the calib subdirectory of each MARCI PDS data release for each of the seven MARCI filters. The five visible band flat field files (vis1flat.ddd to vis5flat.ddd) are 1024 × 16 arrays of data saved in 8-bit (0–255) format, and the two UV band flat fields (uv6flat.ddd, and uv7flat.ddd) are 128 × 2 arrays saved in floating point format. The most recent PDS archived flat field image updates occurred on 1 March 2007. Future updates will include those on the basis of the HST-derived UV cross-calibration refinements described in section 6.4.1. Each file has a 1024 byte header providing more details on the file structure. The first word of the header contains a normalization factor for that file. To derive a normalized (floating point, mean = 1.0) flat field image for that band, the 8-bit data must be divided by the normalization factor. The 8-bit flat field files do not require decompanding; they are simply stored in that format.

[163] If the summing mode of the visible wavelength data is not equal to 1, the normalized flat field file must be "aligned" with the summed MARCI data. This is achieved by binning the rows and columns of the normalized flat by a factor of 2 or 4, depending on the summing factor. For example, if the visible band summing is 2, then the new normalized flat field file will be a 512 × 8 array averaged

Table 8. MARCI 8–11-Bit Decompanding Table[a]

8 Bit	11 Bit	8 Bit	11 Bit	8 Bit	11 Bit	8 Bit	11 Bit	8 Bit	11 Bit	8 Bit	11 Bit
0	0	46	83	92	291	138	625	184	1084	230	1669
1	1	47	86	93	297	139	633	185	1095	231	1683
2	2	48	90	94	303	140	642	186	1107	232	1697
3	3	49	93	95	309	141	651	187	1118	233	1712
4	3	50	96	96	315	142	660	188	1130	234	1726
5	4	51	100	97	321	143	669	189	1142	235	1740
6	5	52	103	98	328	144	678	190	1153	236	1755
7	5	53	107	99	334	145	687	191	1165	237	1769
8	6	54	110	100	340	146	696	192	1177	238	1784
9	7	55	114	101	346	147	705	193	1189	239	1798
10	8	56	118	102	353	148	714	194	1201	240	1813
11	9	57	121	103	359	149	723	195	1212	241	1828
12	10	58	125	104	366	150	732	196	1225	242	1842
13	11	59	129	105	373	151	742	197	1237	243	1857
14	13	60	133	106	379	152	751	198	1249	244	1872
15	14	61	137	107	386	153	761	199	1261	245	1887
16	15	62	141	108	393	154	770	200	1273	246	1902
17	17	63	145	109	400	155	780	201	1286	247	1917
18	18	64	150	110	407	156	789	202	1298	248	1932
19	20	65	154	111	414	157	799	203	1310	249	1947
20	21	66	158	112	421	158	809	204	1323	250	1963
21	23	67	163	113	428	159	819	205	1336	251	1978
22	25	68	167	114	435	160	829	206	1348	252	1993
23	26	69	171	115	442	161	839	207	1361	253	2009
24	28	70	176	116	449	162	849	208	1374	254	2024
25	30	71	181	117	457	163	859	209	1386	255	2040
26	32	72	185	118	464	164	869	210	1399		
27	34	73	190	119	472	165	879	211	1412		
28	36	74	195	120	479	166	889	212	1425		
29	38	75	200	121	487	167	900	213	1438		
30	40	76	205	122	494	168	910	214	1451		
31	43	77	210	123	502	169	920	215	1464		
32	45	78	215	124	510	170	931	216	1478		
33	47	79	220	125	518	171	941	217	1491		
34	50	80	225	126	526	172	952	218	1504		
35	52	81	230	127	534	173	963	219	1518		
36	55	82	235	128	542	174	973	220	1531		
37	57	83	241	129	550	175	984	221	1545		
38	60	84	246	130	558	176	995	222	1558		
39	63	85	251	131	566	177	1006	223	1572		
40	65	86	257	132	574	178	1017	224	1586		
41	68	87	262	133	582	179	1028	225	1599		
42	71	88	268	134	591	180	1039	226	1613		
43	74	89	274	135	599	181	1050	227	1627		
44	77	90	279	136	608	182	1061	228	1641		
45	80	91	285	137	616	183	1073	229	1655		

[a] See section 7.2.1.

down from the original 1024 × 16 array. No alignment is required for the UV flats, as they already accommodate the fact that all UV data are acquired in summing mode 8. To deal with and "flag" known bad pixels on the MARCI array, any pixels in the normalized, aligned (if necessary) flat field arrays that have normalized values less than 0.25 are set to zero.

[164] Finally, to apply the flat field correction to the decompanded MARCI data, the data are divided, band by band, by the normalized, aligned (if necessary), bad pixel-filtered (if necessary) flat field array for each band. Care must be taken to ensure that the correct flat field array is applied to each part (i.e., framelet) of the original MARCI frames that have been concatenated into the archived data files (Figure 23).

7.2.3. Determination of Visible Versus UV Exposure Times

[165] Even though every filter in each MARCI frame is integrated for the same exposure time (the LINE_EXPOSURE_DURATION label entry in the image header), clever use of on-chip summing, the programmable interframe delay time (section 5.2.2), and placement of the UV filters "downstream" in the CCD electronic shuttering readout process allows the UV filters to effectively be integrated for a much longer exposure time, enabling much higher SNR than would otherwise be possible in a single frame exposure. Thus, the MARCI visible and UV filter images have different exposure times, despite being obtained essentially simultaneously. The exposure time for the visible filters is the LINE_EXPOSURE_DURATION label entry saved in the image header. The exposure time for the UV filters is related to the visible exposure time via

$$\begin{aligned} \mathrm{uv\_exposure\_time} = {} & \mathrm{INTERFRAME\_DELAY} \\ & - 57.763 - \mathrm{visible\_exposure\_time}, \end{aligned} \quad (3)$$

where all times are in milliseconds, and the value of "INTERFRAME_DELAY" is stored as a keyword in each

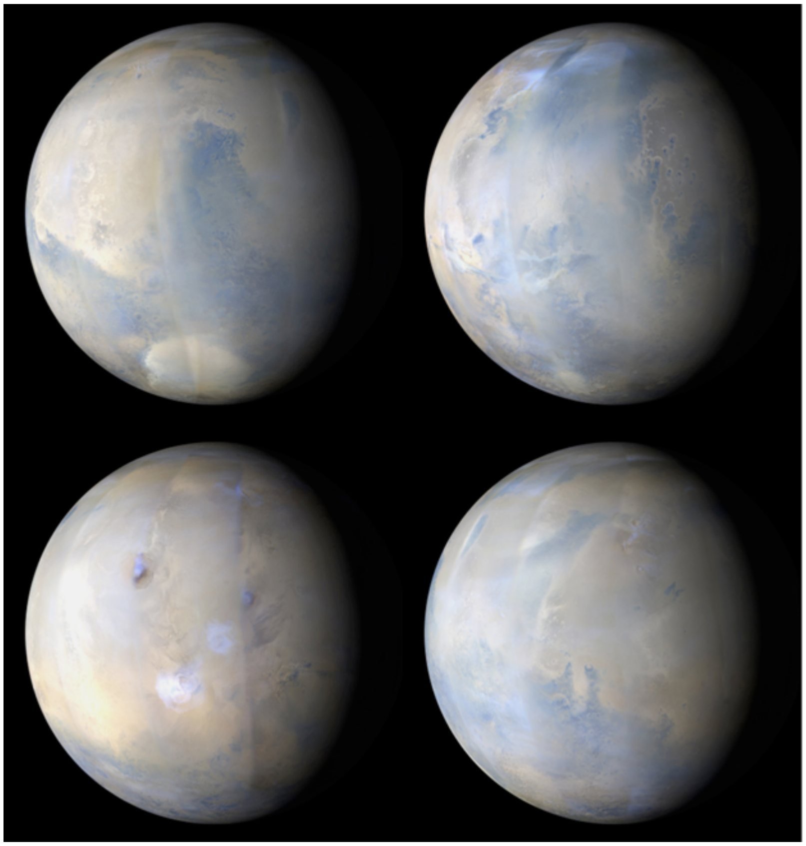

Figure 24. Four hemispheres of Mars as seen in MARCI band 1–3 daily global images, acquired at 1.0 km/pixel and wrapped on a sphere. These data show what Mars looked like ~1500 LT on 14 December 2007 at $L_s = 2°$.

MARCI image header. For example, for MARCI UV data acquired early in the MRO primary science phase when an interframe time of 3.2 s was used, for a programmed visible exposure time of 20 msec, the corresponding UV exposure time is 3.122 s. For data taken later in the primary science phase, when the interframe time was decreased to 2.6 s, for a visible exposure time of 20 msec the UV exposure time will be 0.6 s shorter, or 2.522 s.

7.2.4. Conversion to Radiance and *I/F*

[166] Decompanded and flat fielded MARCI data can be converted to radiance and radiance factor (*I/F*, where *I* is the observed radiance in W/m^2/μm/sr, and πF is the solar spectral irradiance at the top of the Martian atmosphere at the time of the observation, in W/m^2/μm [e.g., *Hapke*, 1993]) using the following equation:

$$I = \mathrm{DN}/\exp/(Sd)/R, \tag{4}$$

where DN is the decompanded, flat fielded MARCI data value, exp is the exposure time in milliseconds for either the visible or UV bands (see section 7.2.3), *S* is the summing factor (1, 2, or 4 for the visible bands, 8 for the UV bands), *d* is the decimation value (1.0 except for UV band 7; see below), and R is the responsivity coefficient. Current best estimates of the values of *R* are listed in Table 4. Note that application of these calibration coefficients for the MARCI UV data assumes that the UV exposure time has been calculated as described in equation (3).

[167] Decimation is the process of discarding pixels in the charge domain direction within the instrument in order to avoid saturating the charge accumulation register during summing. At present, decimation is implemented only in MARCI band 7, and only for data acquired after 21:30:00 UTC on 6 November 2006. The decimation value to use in equation (4) is 1.0 before that time, and 0.25 (e.g., 6 out of 8 pixels are discarded in the summing process) after that time.

[168] To convert the derived MARCI radiance (*I*) to radiance factor (*I/F*) requires an estimate of *F*, the solar radiance at the top of the Martian atmosphere at the time of the observation. *F* can be estimated by

$$F = S/\pi/D^2, \tag{5}$$

where *S* is the solar spectral irradiance at 1 AU [*Wehrli*, 1986] and *D* is the heliocentric distance of Mars at the time of the observation, in AU. Values of *S* that have been convolved with the MARCI responsivity functions are listed in Table 4. *I/F* can be further converted into an estimated Lambert albedo through division by the cosine of the solar incidence angle for each pixel. As described in many other places where this kind of method is used [e.g., *McConnochie et al.*, 2006; *Bell et al.*, 1999, 2006, 2008b], it is important to remember that this approach would result in only an estimate of the narrowband albedo for a particular band

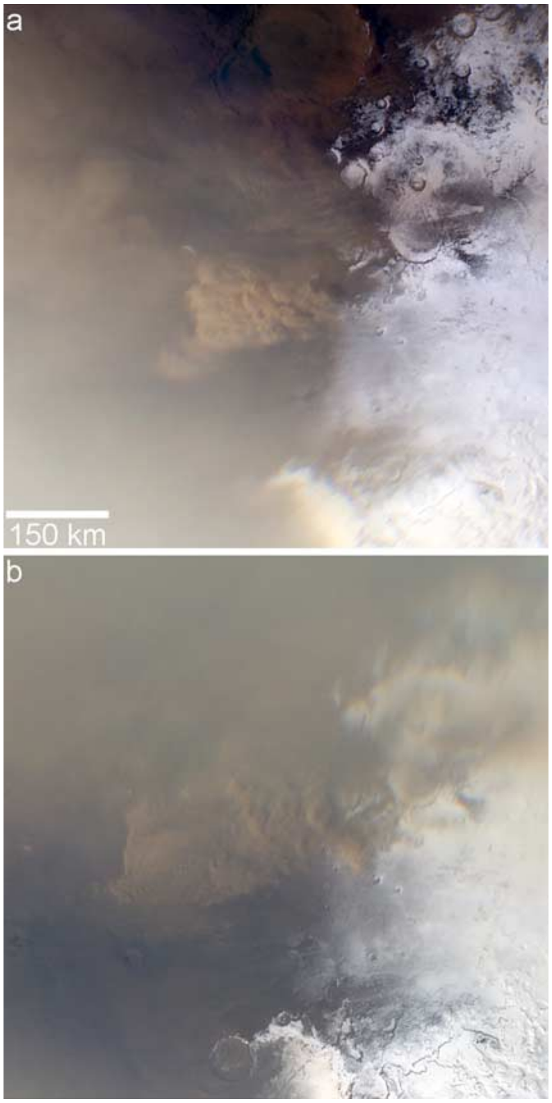

Figure 25. Example of using MARCI to track a local dust storm, centered at 64.4°S, 62.1°W, along the edge of the seasonal south polar cap on the 31 May 2007 at $L_s = 248.2-248.4°$. This storm moved NNW at an average speed of 16.4 $\mathrm{m\ s^{-1}}$ over a period of about 2 h. Images have been polar stereographically projected at a resolution of 1 km $\mathrm{pixels^{-1}}$.

pass, and is thus not directly comparable to broadband albedos such as those derived from MGS/TES or Viking IRTM, without additional analysis.

[169] It is also important to note that in order to maximize SNR during each orbit track, the exposure times of MARCI image sequences may vary over the course of individual MARCI raw images acquired after 28 April 2007 (when this strategy was implemented). For example, the visible band exposure time may have initially been set to a low value for imaging beginning over the bright south polar cap, then reset to a higher value for imaging over darker midlatitude and equatorial terrain, then reset to a lower value for imaging over the bright north polar cap. A text-formatted table called varexp.tab is provided in the "index" subdirectory associated with each MARCI PDS data volume release after that date, and this table describes these exposure time changes. Specifically, each table entry lists the file for which an exposure time change occurs, the first frame (in a zero-based counting system) having a new exposure time, as well as that new visible band exposure time itself, in milliseconds. The corresponding UV filter exposure time can be derived from the visible exposure time using equation (3) above. If the exposure time was changed more than once during an image, that image will have multiple entries in the table. A text file called varexp.lbl is also available in the PDS release that provides more details on the exposure time change table. More generally, additional details of the MARCI calibration pipeline process are described within the document marcical.txt that is stored online within the calib subdirectory associated with each MARCI PDS data volume release.

7.3. More Robust Bias and Scattered Light Removal

[170] As described previously, the above "standard" MARCI pipeline calibration process does not perform any bias, dark current, or scattered/stray light removal steps, primarily because these components of the observed signal level were observed to be too small (typically only from ∼1 to ∼10 DN, or 0.1% to 1% of the typical illuminated Mars signal level) to cause particularly debilitating uncertainties or artifacts in the calibrated data. However, while the dark current has been shown to be effectively zero in the MARCI detector at flight operational temperatures (sections 5.2.2 and 6.2), the magnitude of the residual bias and scattered/stray light components in the raw MARCI VIS filter data is not zero. As a result, for applications that require the highest possible calibration fidelity, an additional

Figure 26. Water-ice clouds over Syrtis Major observed by MRO MARCI on the 13 November 2006 at $L_s = 134.7°$. Images have been simple cylindrically projected at 1 km $\mathrm{pixel^{-1}}$.

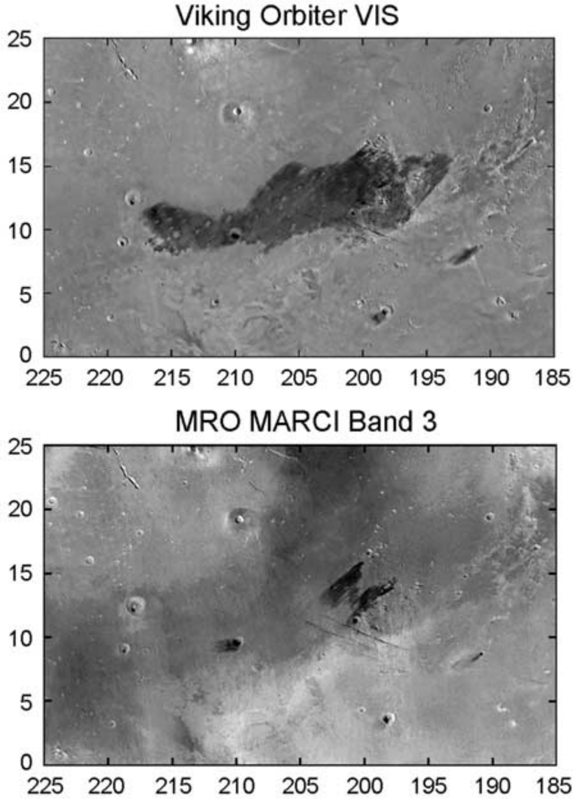

Figure 27. Maps of the Cerberus region. (top) Viking Orbiter VIS red filter photomosaic, resolution of 64 pixels/°. (bottom) MRO MARCI band 3 (604 nm) image, obtained at L_s = 330° (October 2007), resolution of 1.0 km pixel^{-1}. Both maps are in simple cylindrical projection. Note the dramatic changes in the Cerberus albedo feature in the roughly 25 years separating the maps.

(optional) processing step can be performed to effectively remove most of any additional small signal from the visible wavelength data (the correction has not been found to be necessary for the UV filter data).

[171] The first step in this process is to define regions that best characterize the residual background (bias plus scattered light) signal levels in normal (nadir viewing) MARCI images. Examination of large numbers of images led us to choose two standard "reference boxes" in which to characterize the residual background. These boxes are regions near the far left and far right of the MARCI field of view, and under nadir-viewing imaging conditions contain views of space off the limbs of the planet. Because the scattered light varies slightly with filter (section 6.5), the reference boxes are defined framelet by framelet (Figure 23). Specifically, for MARCI VIS data acquired in summing mode 1, the left side reference box was chosen to span columns 1 to 25 and rows 1 to 16, and the right side reference box was chosen to span columns 1000 to 1024 and rows 1 to 16. The limits of these boxes need to be scaled appropriately for summing mode 2 and 4 data.

[172] The average and standard deviation (σ) of all of the pixels in each reference box are calculated, and then the data are "despiked" by discarding all pixels in each box that are outside of 1σ from that initial mean, and recalculating a new mean value. The process is then repeated, to further eliminate outlier pixels. To assess whether there is a gradient in the residual background signal across the array, the despiked means of the left and right reference boxes are averaged, and the RMS error of that average is calculated from the standard deviations of the despiked left and right box data. If the difference between the despiked means of the left and right reference boxes was within two standard deviations, then the average of the despiked left and right box means was judged to be an adequate measure of the residual background signal, and that average would be subtracted from the decompanded raw data (section 7.2.1) before flat fielding. If the difference exceeded two standard deviations, then this indicates the presence of a gradient in the stray light component that would need to be examined in more detail. Typically, this gradient is small and can be modeled with a linear fit to the despiked left and right box means across the array. The modeled background level would then be subtracted from the decompanded raw data before flat fielding.

[173] While only a small correction, the end result of this additional residual signal removal process is a set of calibrated MARCI images with a background level (space look, off the limbs) that is truly zero, typically plus or minus 0.1% to 0.2% of the average illuminated Mars signal.

8. Examples of Initial MARCI Scientific Results

8.1. Atmospheric Studies

[174] MARCI has been acquiring critical data on Martian atmospheric processes from systematic, synoptic observations at the global scale since 24 September 2006. These observations include a daily global mapping campaign (Figure 24) that has effectively provided weather satellite quality coverage of the surface and atmosphere nearly every day (except during spacecraft upsets) for more than 1 Mars year. MARCI daily global maps extend the continuous orbital monitoring of Martian weather phenomena that began with MGS MOC WA imaging in 1999. A significant highlight has been the tracking of regional- and global-scale dust storms (Figure 25) [*Malin et al.*, 2008] in order to better understand the dynamics and energetics of dust transport in the current Martian environment. Indeed, regularly repeated global mapping by MARCI is now the primary method for monitoring dust storm activity at Mars, and is of sufficient spatial and temporal resolution to allow detailed mapping of dust storm timing, location, and evolution. The multispectral capability is important for distinguishing between dust and condensate clouds, and for investigating mixtures of the two. Equally important is the expansion of the historical record of dust storm monitoring. Observations of Mars for multiple years and at a scale of better than 10 km will further define the global dust cycle and help to identify sources and sinks for dust. Coupled with MGS MOC results, the MARCI data enable complete records of more than six consecutive seasonal dust cycles. These combined data sets will be critical in addressing the circumstances that lead to planet encircling dust events and the causes of limited interannual variability in the dust cycle.

[175] The continuous global mapping with MARCI as begun in 2006 is enabling opportunities for new insights into the seasonal and interannual weather patterns observed,

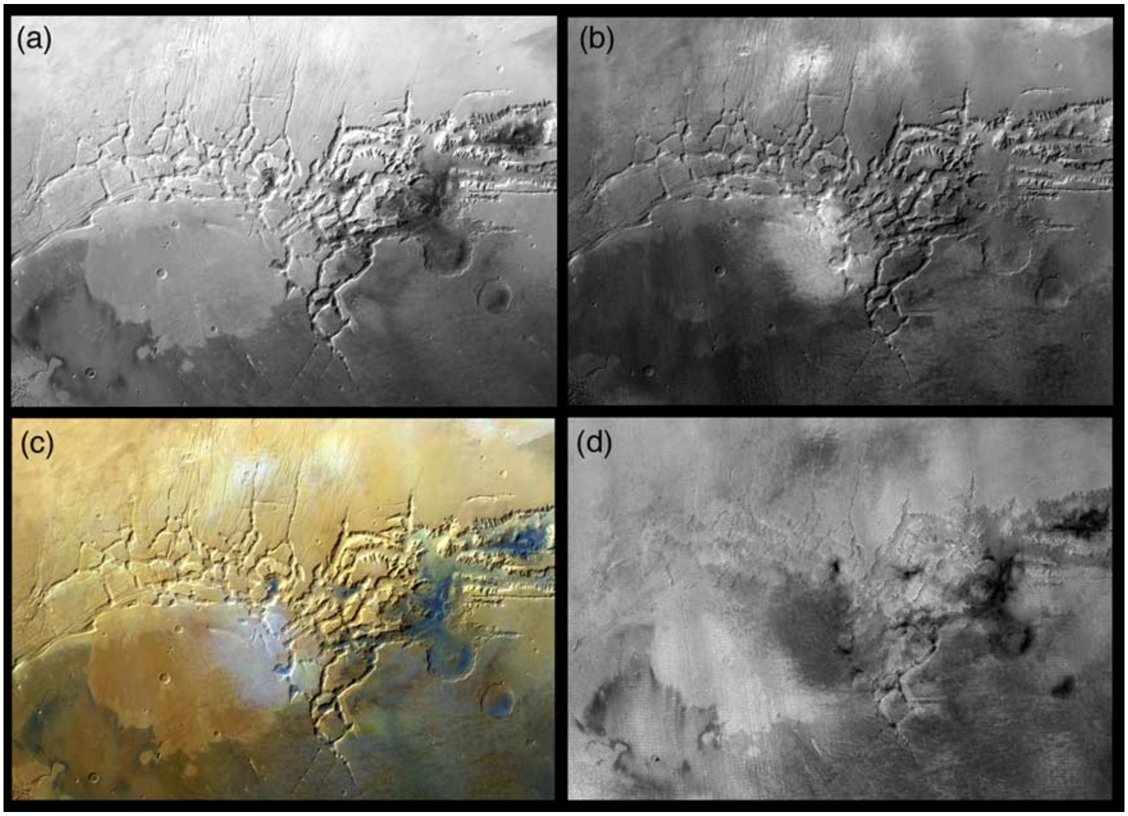

Figure 28. MARCI false color RGB composite mosaic of Noctis Labyrinthus (spanning 0°–15°S latitude top to bottom, and 90°E–110°E, left to right). (a) MARCI band 5 (720 nm) mosaic; (b) MARCI band 1 (440 nm) mosaic; (c) RGB composite generated from bands 5 (720 nm), 2 (540 nm), and 1 (440 nm); (d) MARCI band 5/band 1 (720 nm/440 nm) color ratio mosaic. The mosaic coverage of this region was assembled from 29 separate MARCI images acquired over an L_s range from 240° to 270° (18 May 2007 to 30 June 2007).

potentially illuminating longer-term (decadal) weather cycles. It also opens new possibilities for weather forecasting on short-term as well as seasonal and interannual timescales. These observations have already been demonstrated as vital for providing advance "storm warnings" for the solar powered Mars Exploration Rovers and Phoenix lander, enabling mission teams to properly configure those spacecraft in advance of high dust opacity conditions and thus to maximize their ability to continue to operate on Mars. This kind of short-term weather forecasting capability will no doubt also prove important to other future, long-lived surface missions.

[176] Other highlights have included the detailed characterization and modeling of water ice clouds on Mars from MARCI UV and blue filter observations (Figure 26), and the mapping of atmospheric ozone from the specifically designed UV wavelength bands [e.g., *Clancy et al.*, 2007]. MARCI has been especially useful in actively monitoring the vicinities of the polar caps, in order to determine the relationship between water ice clouds and dust in these frontal systems, distinguish between the retreating seasonal cap edge and the fog generated by that retreat, and to study cloud structure and variability.

8.2. Surface Studies

[177] The excellent calibration and synoptic coverage of MARCI allows monitoring of surface polar cap processes on a large scale, including observation of the effects of atmospheric dust on the seasonal polar cap recession. While many of the albedo changes in the permanent ice caps are below the spatial scale of MARCI, numerous larger-scale phenomena are being monitored, including the albedo drop across Gemini Lingula, the persistence of and/or changes in generally sustained bright patches in the north [*Calvin and Titus*, 2008] and the deposition of dust in the wake of atmospheric dust events [*Malin et al.*, 2008]. In addition, MARCI's daily coverage and multispectral sampling is being used to help monitor the time dependence of albedo as a function of location within the residual polar caps and to discriminate surface frost from ice clouds during periods of the most dynamic seasonal changes.

[178] The significant expansion of the time base of repeated global observations by MARCI is enabling significant insight on the seasonal and interannual stability or variability of surface/atmosphere interactions. Daily global mapping observations by MARCI are ideal for monitoring regional albedo features and for detecting areas undergoing albedo variations, and can be directly intercomparable with the accumulated MOC daily global observations and earlier Viking measurements to encompass a ∼16 Mars year record of surface albedo changes. A representative example is the change in the Cerberus region between the time of Viking and early MGS MOC observations (Figure 27). Where

active variable features are detected, follow-up regional mapping at much higher resolution is being conducted using the MRO Context Camera (CTX) and CRISM instruments.

[179] Finally, the MARCI daily global mapping campaign is enabling the generation of high-quality "atmospherically minimized" mosaics to be culled from the large amount of overlap coverage of surface regions from sol to sol. For example, mosaics can be generated from tens to hundreds of input image sequences over relatively small ranges of L_s (tens of degrees) in order to build up regional multispectral maps of the surface with the least amount of dust and/or water ice aerosol "contamination" per pixel (e.g., Figure 28). These maps can then be analyzed using simple multispectral analysis methods like color ratios or band depth maps to provide unprecedented constraints on the crystallinity and oxidation state of iron-bearing minerals at the ~1 km spatial scale [e.g., *Bell et al.*, 2008c].

9. Summary

[180] The MRO/MARCI instrument was designed to acquire daily synoptic-scale multispectral images of Mars in order to enable investigations that study the evolution of weather systems, polar volatiles, and surface features modified by aeolian processes. The instrument is simple in design, has no moving parts, and is relatively simple to operate: a 1024×1024 push frame CCD camera with seven bonded on narrowband filters (five visible, two UV) and wide-angle (180°) optics uses a framing rate carefully timed to spacecraft ground track motion in order to provide limb-to-limb multispectral images covering all dayside latitudes within about ±2 h of 15:00 local solar time on almost every MRO orbit. Over the course of each ~12 MRO orbits per sol, MARCI coverage overlap has enabled the creation of a "global image" for every Martian sol since late September 2006 (i.e., before the beginning of the MRO primary science phase, which began in November 2006).

[181] Some instrumental and operational simplicity has been traded for postprocessing complexity in the MARCI investigation. Raw MARCI images are concatenations of hundreds of individual snapshots (frames) of separate filter-covered subareas of the CCD (framelets), which then have to be extracted and sorted into continuous image strips in each desired wavelength. MARCI framelets are decompanded from 8–11-bit format, corrected for pixel-to-pixel nonuniformity (flat field) variations, and scaled to radiance or radiance factor on the basis of preflight laboratory calibrations. The fidelity of the calibration has been verified and/or improved by in-flight validation tests and calibration refinement observations. Geometric rectification and map projection of the resulting calibrated data enables the creation of multispectral mosaics and global maps for scientific analysis. A major goal of this paper has been to describe the instrument, its requirements, its operations, and its calibration in sufficient detail so that both the potential and the limitations of the data set can be well understood by contemporary and future MARCI data users.

[182] MARCI is obtaining important and high-quality scientific and operational (supporting other missions) data as part of a coordinated Program of Mars spacecraft exploration that began in the mid-1990s. Perhaps most importantly, MARCI observations extend and enhance the 4 Mars years of detailed daily, seasonal, and interannual monitoring of the current Martian climate that was begun by Mars Global Surveyor. New insights on dust storms (at all scales), atmospheric volatile transport, polar cap growth and recession, surface albedo feature variability, and surface composition are continually being obtained from this successful, ongoing investigation. There is every reason to believe that MARCI will play a critical role in making new discoveries during what will hopefully be many extended missions for the MRO spacecraft.

Appendix A: MARCI File Naming Scheme

[183] Raw MARCI data released via the NASA Planetary Data System (PDS; archived online at, for example, http://pds-imaging.jpl.nasa.gov/Admin/resources/cd_mro.html) use the following file naming convention: *ppp_nnnnnn_tttt_*M*x_aahbbb*W.IMG.

[184] 1. Here *ppp* is MRO Mission subphase. For the first character, "T" means Transition orbit subphase, between Mars Orbit Insertion (MOI) in March 2006 and the beginning of the primary science phase in November 2006, and "P" means primary science phase and subsequent extended mission phase are labeled "B" (September 2008 through June 2010) and "G" (after June 2010). The second two characters are a numerical count of the number of Earth months in that mission subphase, starting with P01 in November 2006.

[185] 2. Here *nnnnnn* is the MRO orbit number, starting with 000001 at MOI in March 2006.

[186] 3. Here *tttt* is the areocentric longitude of the Sun (L_s) or Martian season at the start of the observation, with the last digit being the first decimal place of the value to the nearest 0.1° (e.g., 1745 = 174.5°). $L_s = 0°$ is defined as the first day of spring (the vernal equinox) in the northern hemisphere.

[187] 4. M indicates that this is a MARCI image.

[188] 5. Here *x* is A, B, C, D, or U, where A indicates that the five MARCI VIS filters were acquired and are included in this file; B indicates that MARCI bands 1, 2, 3, and 5 (437, 546, 604, and 718 nm) were acquired; C indicates that MARCI bands 1, 2, and 3 (437, 546, and 604 nm) were acquired; D indicates that MARCI bands 1, 2, 3, and 4 (437, 546, 604, and 653 nm) were acquired; and U indicates that this file contains only the MARCI UV filter observations for this sequence.

[189] 6. Here *aa* is "00" by default for normal "one observation sequence per orbit" long MARCI image strips that cross the equator. However, if this number is not 00 then it indicates the latitude at the center of the image (to the nearest degree), for multiple observations taken on the same orbit.

[190] 7. Here *h* is N for north latitude (the default for MARCI) or S for south latitude;

[191] 8. Here *bbb*W is the west longitude (to the nearest degree) at the planned dayside equator crossing of the spacecraft.

[192] For example, the file P06_003537_2280_MA_00N356W.IMG is a raw MARCI PDS-formatted image acquired during the primary science phase in April 2007 (6 months from November 2006) during MRO orbit 3537 and at $L_s = 228.0°$. The file contains framelets from all five

MARCI VIS filters, from a single long image strip acquired on this orbit that crossed the dayside equator at 356°W longitude.

[193] **Acknowledgments.** The MARCI development, operations, and science teams are privileged to have had an enormous amount of help with this investigation from the Mars Reconnaissance Orbiter spacecraft and operations teams at Lockheed Martin (Denver, CO) and the Jet Propulsion Laboratory (Pasadena, CA). The authors thank Jeff Johnson and an anonymous reviewer for comments and suggestions that substantially improved an earlier draft of this paper. We also thank Shireen Gonzaga of the Space Telescope Science Institute for helpful conversations regarding the absolute calibration of the HST data and Ryan Anderson and Karrie Kressler at Cornell University for assistance with MARCI calibration and mapping software. This work is funded by NASA contracts from the Mars Reconnaissance Orbiter Project to Malin Space Science Systems, Inc., and Cornell University and was also supported in part by Space Telescope Science Institute DD grant 11314.

References

Adams, J. B., and T. B. McCord (1969), Mars: Interpretation of spectral reflectivity of light and dark regions, *J. Geophys. Res.*, *74*, 4851–4856, doi:10.1029/JB074i020p04851.

Balme, M. R., P. L. Whelley, and R. Greeley (2003), Mars: Dust devil track survey in Argyre Planitia and Hellas Basin, *J. Geophys. Res.*, *108*(E8), 5086, doi:10.1029/2003JE002096.

Bandfield, J. L. (2002), Global mineral distributions on Mars, *J. Geophys. Res.*, *107*(E6), 5042, doi:10.1029/2001JE001510.

Barnes, J. R., J. B. Pollack, R. M. Haberle, C. B. Leovy, R. W. Zurek, H. Lee, and J. Schaeffer (1993), Mars atmospheric dynamics as simulated by the NASA AMES General Circulation Model: Part 2. Transient baroclinic eddies, *J. Geophys. Res.*, *98*, 3125–3148, doi:10.1029/92JE02935.

Barth, C. A., C. W. Hord, A. I. Stewart, A. L. Lane, M. L. Dick, and G. P. Anderson (1973), Mariner 9 ultraviolet spectrometer experiment: Seasonal variations of ozone on Mars, *Science*, *179*, 795–796.

Bass, D. S., K. E. Herkenhoff, and D. A. Paige (2000), Variability of Mars' north polar water ice cap: part I. Analysis of Mariner 9 and Viking Orbiter imaging data, *Icarus*, *144*, 382–396, doi:10.1006/icar.1999.6300.

Basu, S., M. I. Richardson, and R. J. Wilson (2004), Simulation of the Martian dust cycle with the GFDL Mars GCM, *J. Geophys. Res.*, *109*, E11006, doi:10.1029/2004JE002243.

Bell, J. F., III, T. B. McCord, and P. D. Owensby (1990), Observational evidence of crystalline iron oxides on Mars, *J. Geophys. Res.*, *95*, 14,447–14,461, doi:10.1029/JB095iB09p14447.

Bell, J. F., III, M. J. Wolff, T. C. Daley, D. Crisp, P. B. James, S. W. Lee, J. T. Trauger, and R. W. Evans (1999), Near-infrared imaging of Mars from HST: Surface reflectance, photometric properties, and implications for MOLA data, *Icarus*, *138*, 25–35, doi:10.1006/icar.1998.6057.

Bell, J. F., III, et al. (2000), Mineralogic and compositional properties of Martian soil and dust: Results from Mars Pathfinder, *J. Geophys. Res.*, *105*, 1721–1755, doi:10.1029/1999JE001060.

Bell, J. F., III, et al. (2003), Mars Exploration Rover Athena Panoramic Camera (Pancam) investigation, *J. Geophys. Res.*, *108*(E12), 8063, doi:10.1029/2003JE002070.

Bell, J. F., III, et al. (2004a), Pancam multispectral imaging results from the Spirit rover at Gusev Crater, *Science*, *305*, 800–806, doi:10.1126/science.1100175.

Bell, J. F., III, et al. (2004b), Pancam multispectral imaging results from the Opportunity Rover at Meridiani Planum, *Science*, *306*, 1703–1709, doi:10.1126/science.1105245.

Bell, J. F., III, J. Joseph, J. N. Sohl-Dickstein, H. M. Arneson, M. J. Johnson, M. T. Lemmon, and D. Savransky (2006), In-flight calibration and performance of the Mars Exploration Rover Panoramic Camera (Pancam) instruments, *J. Geophys. Res.*, *111*, E02S03, doi:10.1029/2005JE002444.

Bell, J. F., III, T. Glotch, V. Hamilton, T. McConnochie, T. McCord, A. McEwen, P. Christensen, and R. Arvidson (2008a), Visible to near-IR multispectral observations of Mars, in *The Martian Surface: Composition, Mineralogy, and Physical Properties*, edited by J. F. Bell III, chap. 8, pp. 169–194, Cambridge Univ. Press, New York.

Bell, J. F., III, M. S. Rice, J. R. Johnson, and T. M. Hare (2008b), Surface albedo observations at Gusev Crater and Meridiani Planum, Mars, *J. Geophys. Res.*, *113*, E06S18, doi:10.1029/2007JE002976.

Bell, J. F., III, K. Kressler, R. B. Anderson, and M. J. Wolff (2008c), MRO MARCI-CTX science and operations teams, color mosaics and multispectral analyses of Mars Reconnaissance Orbit Mars Color Imager (MARCI) observations, *Eos Trans. AGU*, Fall Meet. Suppl., Abstract.

Benson, J. L., and P. B. James (2005), Yearly comparisons of the Martian polar caps: 1999–2003 Mars Orbiter Camera observations, *Icarus*, *174*, 513–523, doi:10.1016/j.icarus.2004.08.025.

Benson, J. L., B. P. Bonev, P. B. James, K. J. Shan, B. A. Cantor, and M. S. Caplinger (2003), The seasonal behavior of water ice clouds in the Tharsis and Valles Marineris regions of Mars: Mars Orbiter Camera observations, *Icarus*, *165*, 34–52, doi:10.1016/S0019-1035(03)00175-1.

Benson, J. L., P. B. James, B. A. Cantor, and R. Remigo (2006), Interannual variability of water ice clouds over major Martian volcanoes observed by MOC, *Icarus*, *184*, 365–371, doi:10.1016/j.icarus.2006.03.014.

Bibring, J.-P., and Y. Langevin (2008), Mineralogy of the Martian surface from Mars Express OMEGA observations, in *The Martian Surface: Composition, Mineralogy, and Physical Properties*, edited by J. F. Bell III, chap. 7, pp. 153–168, Cambridge Univ. Press, New York.

Bibring, J.-P., et al. (2005), Mars surface diversity as revealed by the OMEGA/Mars Express observations, *Science*, *307*, 1576–1581, doi:10.1126/science.1108806.

Bonev, B. P., P. B. James, J. E. Bjorkman, and M. J. Wolff (2002), Regression of the Mountains of Mitchel polar ice after the onset of a global dust storm on Mars, *Geophys. Res. Lett.*, *29*(21), 2017, doi:10.1029/2002GL015458.

Boreman, G. D. (2001), *Modulation Transfer Function in Optical and Electro-Optical Systems*, *Tutorial Texts Opt. Eng. Ser.*, vol. TT52, SPIE Press, Bellingham, Wash.

Briggs, G. A., and C. B. Leovy (1974), Mariner 9 observations of the Mars north polar hood, *Bull. Am. Meteorol. Soc.*, *55*, 278–296, doi:10.1175/1520-0477(1974)055<0278:MOOTMN>2.0.CO;2.

Briggs, G. A., W. A. Baum, and J. Barnes (1979), Viking Orbiter imaging observations of dust in the Martian atmosphere, *J. Geophys. Res.*, *84*, 2795–2820, doi:10.1029/JB084iB06p02795.

Calvin, W. M., and T. N. Titus (2008), Summer season variability of the North Residual Cap of Mars as observed by the Mars Global Surveyor Thermal Emission Spectrometer (MGS-TES), *Planet. Space Sci.*, *56*, 212–226, doi:10.1016/j.pss.2007.08.005.

Cantor, B. A. (2003), MGS-MOC observations of Martian dust storm activity, in *Sixth International Conference on Mars, July 20–25, 2003, Pasadena CA* [CD-ROM], *LPI Contrib.*, *1164*, Abstract 3166. (Available at http://www.lpi.usra.edu/meetings/sixthmars2003/pdf/3166.pdf)

Cantor, B. A. (2007a), MOC observations of the 2001 Mars planet-encircling dust storm, *Icarus*, *186*, 60–96, doi:10.1016/j.icarus.2006.08.019.

Cantor, B. A. (2007b), Present-day Martian weather–5 Mars years of observations by MGS-MOC and MRO-MARCI, in *Seventh International Conference on Mars, July 9–13, 2007, Pasadena CA* [CD-ROM], *LPI Contrib.*, *1353*, Abstract 3063. (Available at http://www.lpi.usra.edu/meetings/7thmars2007/pdf/3063.pdf)

Cantor, B. A., and M. C. Malin (2007), Martian weather: Approximately 5 Mars years of MOC and MARCI observations, *Bull. Am. Astron. Soc.*, *39*, 441.

Cantor, B. A., P. B. James, M. Caplinger, and M. J. Wolff (2001), Martian dust storms: 1999 Mars Orbiter Camera observations, *J. Geophys. Res.*, *106*(E10), 23,653–23,688, doi:10.1029/2000JE001310.

Cantor, B. A., M. C. Malin, and K. S. Edgett (2002), Multiyear Mars Orbiter Camera (MOC) observations of repeated Martian weather phenomena during the northern summer season, *J. Geophys. Res.*, *107*(E3), 5014, doi:10.1029/2001JE001588.

Cantor, B. A., K. M. Kanak, and K. S. Edgett (2006), Mars Orbiter Camera observations of Martian dust devils and their tracks (September 1997 to January 2006) and evaluation of theoretical vortex models, *J. Geophys. Res.*, *111*, E12002, doi:10.1029/2006JE002700.

Christensen, P. R., et al. (2000a), Detection of crystalline hematite mineralization on Mars by the Thermal Emission Spectrometer: Evidence for near-surface water, *J. Geophys. Res.*, *105*, 9623–9642, doi:10.1029/1999JE001093.

Christensen, P. R., J. L. Bandfield, M. D. Smith, V. E. Hamilton, and R. N. Clark (2000b), Identification of a basaltic component on the Martian surface from Thermal Emission Spectrometer data, *J. Geophys. Res.*, *105*, 9609–9622, doi:10.1029/1999JE001127.

Christensen, P. R., et al. (2004), Thermal Emission Imaging System (THEMIS) for the Mars 2001 Odyssey Mission, *Space Sci. Rev.*, *110*, 85–130, doi:10.1023/B:SPAC.0000021008.16305.94.

Christensen, P. R., J. L. Bandfield, A. D. Rogers, T. D. Glotch, V. E. Hamilton, S. W. Ruff, and B. M. Wyatt (2008), Global mineralogy mapped from the Mars Global Surveyor Thermal Emission Spectrometer, in *The Martian Surface: Composition, Mineralogy, and Physical Properties*, edited by J. F. Bell III, chap. 9, pp. 22–195, Cambridge Univ. Press, New York.

Clancy, R. T., and H. Nair (1996), Annual (perihelion-aphelion) cycles in the photochemical behavior of the global Mars atmosphere, *J. Geophys. Res.*, *101*, 12,785–12,790, doi:10.1029/96JE00836.

Clancy, R. T., D. O. Muhleman, and G. L. Berge (1990), Global changes in the 0–70 km thermal structure of the Mars atmosphere derived from 1975 to 1989 microwave CO spectra, *J. Geophys. Res.*, *95*, 14,543–14,554, doi:10.1029/JB095iB09p14543.

Clancy, R. T., M. J. Wolff, P. B. James, E. Smith, Y. N. Billawala, S. W. Lee, and M. Callan (1996), Mars ozone measurements near the 1995 aphelion: Hubble Space Telescope ultraviolet spectroscopy with the Faint Object Spectrograph, *J. Geophys. Res.*, *101*, 12,777–12,784, doi:10.1029/96JE00835.

Clancy, R. T., M. J. Wolff, and P. B. James (1999), Minimal aerosol loading and global increases in atmospheric ozone during the 1996–1997 Martian northern spring season, *Icarus*, *138*, 49–63, doi:10.1006/icar.1998.6059.

Clancy, R. T., B. J. Sandor, M. J. Wolff, P. R. Christensen, M. D. Smith, J. C. Pearl, B. J. Conrath, and R. J. Wilson (2000), An intercomparison of ground-based millimeter, MGS TES, and Viking atmospheric temperature measurements: Seasonal and interannual variability of temperatures and dust loading in the global Mars atmosphere, *J. Geophys. Res.*, *105*, 9553–9571, doi:10.1029/1999JE001089.

Clancy, R. T., M. J. Wolff, B. A. Whitney, and B. A. Cantor (2004), The distribution of high altitude (70 km) ice clouds in the Mars atmosphere from MGS TES and MOC limb observations, *Bull. Am. Astron. Soc.*, *36*, 1128.

Clancy, R. T., et al. (2007), Mars ozone measurements from the Mars Reconnaissance Orbiter (MRO) MARCI and CRISM experiments, in *Seventh International Conference on Mars, July 9–13, 2007, Pasadena CA* [CD-ROM], *LPI Contrib.*, *1353*, Abstract 3082. (Available at http://www.lpi.usra.edu/meetings/7thmars2007/pdf/3082.pdf)

Curran, R. J., B. J. Conrath, R. A. Hanel, V. G. Kunde, and J. C. Pearl (1973), Mars: Mariner 9 spectroscopic evidence for H_2O ice clouds, *Science*, *182*, 381–383, doi:10.1126/science.182.4110.381.

de Grenier, M., and P. C. Pinet (1995), Near-opposition Martian limb-darkening: Quantification and implication for visible–near-infrared bidirectional reflectance studies, *Icarus*, *115*, 354–368, doi:10.1006/icar.1995.1103.

Ferri, F., P. H. Smith, M. Lemmon, and N. O. Renno (2003), Dust devils as observed by Mars Pathfinder, *J. Geophys. Res.*, *108*(E12), 5133, doi:10.1029/2000JE001421.

Fischer, E. M., and C. M. Pieters (1993), The continuum slope of Mars: Bidirectional reflectance investigations and applications to Olympus Mons, *Icarus*, *102*, 185–202, doi:10.1006/icar.1993.1043.

Fisher, J. A., M. I. Richardson, C. E. Newman, M. A. Szwast, C. Graf, S. Basu, S. P. Ewald, A. D. Toigo, and R. J. Wilson (2005), A survey of Martian dust devil activity using Mars Global Surveyor Mars Orbiter Camera images, *J. Geophys. Res.*, *110*, E03004, doi:10.1029/2003JE002165.

Geissler, P. E. (2005), Three decades of Martian surface changes, *J. Geophys. Res.*, *110*, E02001, doi:10.1029/2004JE002345.

Geissler, P. E., R. B. Singer, G. Komatsu, S. Murchie, and J. Mustard (1993), An unusual spectral unit in West Candor Chasma: Evidence for aqueous or hydrothermal alteration in the Martian canyons, *Icarus*, *106*, 380–391, doi:10.1006/icar.1993.1179.

Geissler, P., W. R. Thompson, R. Greenberg, J. Moersch, A. McEwen, and C. Sagan (1995), Galileo multispectral imaging of Earth, *J. Geophys. Res.*, *100*, 16,895–16,906, doi:10.1029/95JE01407.

Gendrin, A., et al. (2005), Sulfates in Martian layered terrains: The OMEGA/Mars Express view, *Science*, *307*, 1587–1591, doi:10.1126/science.1109087.

Gifford, F. A. (1964), The Martian canals according to a purely aeolian hypothesis, *Icarus*, *3*, 130–135, doi:10.1016/0019-1035(64)90054-5.

Guerineau, N., J. Primot, M. Tauvy, and M. Caes (1999), Modulation transfer function measurement of an infrared focal plane array by use of the self-imaging property of a canted periodic target, *Appl. Opt.*, *38*, 631–637, doi:10.1364/AO.38.000631.

Guinness, E. W., R. E. Arvidson, I. Clark, and M. K. Shepard (1997), Optical scattering properties of terrestrial varnished basalts compared with rocks and soils at the Viking Lander sites, *J. Geophys. Res.*, *102*, 28,687–28,703, doi:10.1029/97JE03018.

Haberle, R. M., J. R. Murphy, and J. Schaeffer (2003), Orbital change experiments with a Mars general circulation model, *Icarus*, *161*, 66–89, doi:10.1016/S0019-1035(02)00017-9.

Haberle, R. M., J. Noble, J. R. Murphy, A. F. Bridger, J. L. Hollingsworth, B. Cantor, M. Malin, and M. Smith (2005), Synthesis of MGS observations of the 2001 global dust storm on Mars: Implications for atmospheric dynamics, *Eos Trans. AGU*, *86*(52), Fall Meet. Suppl., Abstract P21E-07.

Hansen, G. B. (1999), Control of the radiative behavior of the Martian polar caps by surface CO_2 ice: Evidence from Mars Global Surveyor measurements, *J. Geophys. Res.*, *104*(E7), 16,471–16,486, doi:10.1029/1998JE000626.

Hapke, B. (1993), *Theory of Reflectance and Emittance Spectroscopy*, 455 pp., Cambridge Univ. Press, New York.

Hinson, D., and R. J. Wilson (2004), Temperature inversions, thermal tides, and water ice clouds in the Martian tropics, *J. Geophys. Res.*, *109*, E01002, doi:10.1029/2003JE002129.

Hoefen, T. M., R. N. Clark, J. L. Bandfield, M. D. Smith, J. C. Pearl, and P. R. Christensen (2003), Discovery of olivine in the Nili Fossea region of Mars, *Science*, *302*, 627–630, doi:10.1126/science.1089647.

Hollingsworth, J. L., R. M. Haberle, A. F. C. Bridger, J. B. Pollack, H. Lee, and J. Schaeffer (1996), Winter storm zones on Mars, *Nature*, *380*, 413–416, doi:10.1038/380413a0.

James, P. B., and B. A. Cantor (2001), Martian North Polar cap recession: 2000 Mars Orbiter Camera observations, *Icarus*, *154*, 131–144, doi:10.1006/icar.2001.6653.

James, P. B., and S. W. Lee (1999), Hubble Space Telescope observations of planets and satellites, *Annu. Rev. Earth Planet. Sci.*, *27*, 115–148, doi:10.1146/annurev.earth.27.1.115.

James, P. B., K. M. Malolepszy, and L. J. Martin (1987), Interannual variability of Mars' south polar cap, *Icarus*, *71*, 298–305, doi:10.1016/0019-1035(87)90154-0.

James, P. B., R. T. Clancy, S. Lee, L. J. Martin, R. B. Singer, E. Smith, R. Kahn, and R. Zurek (1994), Monitoring Mars with the Hubble Space Telescope: 1990–1991 observations, *Icarus*, *109*, 79–101, doi:10.1006/icar.1994.1078.

James, P. B., J. F. Bell III, R. T. Clancy, S. W. Lee, L. J. Martin, and M. J. Wolff (1996), Global imaging of Mars by Hubble Space Telescope during the 1995 opposition, *J. Geophys. Res.*, *101*, 18,883–18,890, doi:10.1029/96JE01605.

Janesick, J. R., K. P. Klaasen, and T. Elliot (1987), Charge-coupled device charge-collection efficiency and the photon transfer technique, *Opt. Eng.*, *26*, 972–980.

Johnson, J. R., and W. M. Grundy (2001), Visible/near-infrared spectra and two-layer modeling of palagonite-coated basalts, *Geophys. Res. Lett.*, *28*, 2101–2104, doi:10.1029/2000GL012669.

Johnson, J. R., J. F. Bell III, P. Geissler, W. M. Grundy, E. A. Guinness, P. C. Pinet, and J. Soderblom (2008), Physical properties of the Martian surface from spectrophotometric observations, in *The Martian Surface: Composition, Mineralogy, and Physical Properties*, edited by J. F. Bell III, chap. 19, pp. 428–450, Cambridge Univ. Press, New York.

Kahn, R. (1984), The spatial and seasonal distribution of Martian clouds and some meteorological implications, *J. Geophys. Res.*, *89*, 6671–6688, doi:10.1029/JA089iA08p06671.

Kahn, R. A., T. Z. Martin, R. W. Zurek, and S. W. Lee (1992), The Martian dust cycle, in *Mars*, edited by H. H. Kieffer et al., pp. 1017–1053, Univ. of Ariz. Press, Tucson, Ariz.

Kahre, M. A., J. R. Murphy, R. M. Haberle, F. Montmessin, and J. Schaeffer (2005), Simulating the Martian dust cycle with a finite surface dust reservoir, *Geophys. Res. Lett.*, *32*, L20204, doi:10.1029/2005GL023495.

Kieffer, H. H., and T. C. Stone (2005), The spectral irradiance of the Moon, *Astron. J.*, *129*, 2887–2901, doi:10.1086/430185.

Kirkland, L. E., and K. C. Herr (2000), Spectral anomalies in the 11 and 12 μm region from the Mariner Mars 7 infrared spectrometer, *J. Geophys. Res.*, *105*, 22,507–22,515, doi:10.1029/1999JE001214.

Klingelhöfer, G., et al. (2004), Jarosite and Hematite at Meridiani Planum from Opportunity's Mössbauer Spectrometer, *Science*, *306*, 1740–1745, doi:10.1126/science.1104653.

Kuhn, J. R., H. Lin, and D. Loranz (1991), Gain calibrating nonuniform image-array data using only the image data, *Publ. Astron. Soc. Pac.*, *103*, 1097–1108, doi:10.1086/132932.

Langevin, Y., F. Poulet, J. P. Bibring, and B. Gondet (2005), Summer evolution of the north polar cap of Mars as observed by OMEGA/Mars express, *Science*, *307*(5715), 1581–1584, doi:10.1126/science.1109438.

Langevin, Y., J. P. Bibring, F. Montmessin, F. Forget, M. Vincendon, S. Doute, F. Poulet, and B. Gondet (2007), Observations of the south seasonal cap of Mars during recession in 2004–2006 by the OMEGA visible/near-infrared imaging spectrometer on board Mars Express, *J. Geophys. Res.*, *112*, E08S12, doi:10.1029/2006JE002841.

Lebonnois, S., E. Quémerais, F. Montmessin, F. Lefèvre, S. Perrier, J. L. Bertaux, and F. Forget (2006), Vertical distribution of ozone, on Mars as measured by SPICAM/Mars-Express using stellar occultations, *J. Geophys. Res.*, *111*, E09S05, doi:10.1029/2005JE002643.

Lee, S. W., P. C. Thomas, and J. Veverka (1982), Wind streaks in Tharsis and Elysium: Implications for sediment transport by slope winds, *J. Geophys. Res.*, *87*, 10,025–10,042, doi:10.1029/JB087iB12p10025.

Lee, S. W., R. T. Clancy, and T. Z. Martin (1994), Spatial and temporal mapping of regional surface albedo and atmospheric dust opacity on Mars, *Bull. Am. Astron. Soc.*, *26*, 1112–1113.

Lefèvre, F., S. Lebonnois, F. Montmessin, and F. Forget (2004), Three-dimensional modeling of ozone on Mars, *J. Geophys. Res.*, *109*, E07004, doi:10.1029/2004JE002268.

Lemmon, M., et al. (2004), Atmospheric imaging results from the Mars Exploration Rovers: Spirit and Opportunity, *Science*, *306*, 1753–1756, doi:10.1126/science.1104474.

Lucey, P. G., J. L. Hinrichs, M. S. Robinson, J. Johnson, C. A. Peterson, N. Domergue-Schmidt, and G. J. Taylor (1997), Near-infrared (1.0–2.0 microns) global imaging of the moon, *Lunar Planet. Sci.*, *XXVIII*, Abstract 1398.

Malin, M., J. F. Bell III, W. Calvin, R. T. Clancy, R. M. Haberle, P. B. James, S. W. Lee, P. C. Thomas, and M. A. Caplinger (2001), The Mars Color Imager (MARCI) on the Mars Climate Orbiter, *J. Geophys. Res.*, *106*, 17,651–17,672, doi:10.1029/1999JE001145.

Malin, M. C., and K. S. Edgett (2001), Mars Global Surveyor Mars Orbiter Camera: Interplanetary cruise through primary mission, *J. Geophys. Res.*, *106*(E10), 23,429–23,570, doi:10.1029/2000JE001455.

Malin, M. C., W. M. Calvin, B. A. Cantor, R. T. Clancy, R. M. Haberle, P. B. James, P. C. Thomas, M. J. Wolff, J. F. Bell III, and S. W. Lee (2008), Climate, weather, and north polar observations from the Mars Reconnaissance Orbiter Mars Color Imager, *Icarus*, *194*, 501–512, doi:10.1016/j.icarus.2007.10.016.

Malin Space Science Systems (MSSS) (2005), Mars Reconnaissance Orbiter, Mars Color Imager (MARCI), and Context Camera (CTX) pre-flight calibration report, *Rep. MSSS-CTX-DOC-2002*, San Diego, Calif. (Available at http://marswatch.astro.cornell.edu/MARCI/Calibration_Report/MARCI_CTX_Cal_Report_v1.5.pdf)

Martin, L. J. (1974a), The major Martian yellow storm of 1971, *Icarus*, *22*, 175–188, doi:10.1016/0019-1035(74)90116-X.

Martin, L. J. (1974b), The major Martian dust storms of 1971 and 1973, *Icarus*, *23*, 108–115, doi:10.1016/0019-1035(74)90108-0.

Martin, L. J. (1976), 1973 dust storm on Mars: Maps from hourly photographs, *Icarus*, *29*, 363–380, doi:10.1016/0019-1035(76)90139-1.

Martin, L. J. (1984), Clearing the Martian air: The troubled history of dust storms, *Icarus*, *57*, 317–321, doi:10.1016/0019-1035(84)90120-9.

Martin, L. J., and R. W. Zurek (1993), An analysis of the history of dust activity on Mars, *J. Geophys. Res.*, *98*, 3221–3246, doi:10.1029/92JE02937.

McConnochie, T. H., J. F. Bell III, D. Savransky, G. Mehall, M. Caplinger, P. R. Christensen, L. Cherednik, K. Bender, and A. Dombovari (2006), Calibration and in-flight performance of the Mars Odyssey THEMIS Visible Imaging Subsystem (VIS) Instrument, *J. Geophys. Res.*, *111*, E06018, doi:10.1029/2005JE002568.

McCord, T. B., R. N. Clark, and R. B. Singer (1982a), Mars: Near-infrared reflectance and spectra of surface regions and compositional implications, *J. Geophys. Res.*, *87*, 3021–3032, doi:10.1029/JB087iB04p03021.

McCord, T. B., R. B. Singer, B. R. Hawke, J. B. Adams, D. L. Evans, J. W. Head, P. J. Mouginis-Mark, C. M. Pieters, R. L. Huguenin, and S. H. Zisk (1982b), Mars: Definition and characterization of global surface units with emphasis on composition, *J. Geophys. Res.*, *87*, 10,129–10,148, doi:10.1029/JB087iB12p10129.

McElroy, M. B., and T. M. Donahue (1972), Stability of the Martian atmosphere, *Science*, *177*, 986–988, doi:10.1126/science.177.4053.986.

McEwen, A. S., and M. S. Robinson (1997), Mapping of the Moon by Clementine, *Adv. Space Res.*, *19*, 1523–1533, doi:10.1016/S0273-1177(97)00365-7.

McKim, R. J. (1996), The dust storms of Mars, *J. Br. Astron. Assoc.*, *106*, 185–200.

McMaster, M. and J. Biretta (Eds.) (2008), *Wide Field and Planetary Camera 2 Instrument Handbook*, version 10.0, Space Telesc. Sci. Inst., Baltimore, Md. (Available at http://www.stsci.edu/hst/wfpc2/documents/handbook/cycle17/wfpc2_cover.html)

McPeters, R. D., et al. (1998), Earth probe Total Ozone Mapping Spectrometer (TOMS) data products user's guide, *Tech. Publ. 1998-206895*, NASA Goddard Space Flight Cent., Greenbelt, Md. (Available at http://toms.gsfc.nasa.gov/n7toms/nim7toms.html)

Mischna, M., J. F. Bell III, P. B. James, and D. Crisp (1998), Synoptic measurements of Martian winds using the Hubble Space Telescope, *Geophys. Res. Lett.*, *25*, 611–614, doi:10.1029/98GL50358.

Miyamoto, S. (1957), The great yellow cloud and the atmosphere of Mars: Report of visual observations during the 1956 opposition, report, p. 71, Univ. of Kyoto, Kyoto, Japan.

Montmessin, F., F. Forget, P. Rannou, M. Cabane, and R. M. Haberle (2004), Origin and role of water ice clouds in the Martian water cycle as inferred from a general circulation model, *J. Geophys. Res.*, *109*, E10004, doi:10.1029/2004JE002284.

Montmessin, F., B. Gondet, J. P. Bibring, Y. Langevin, P. Drossart, F. Forget, and T. Fouchet (2007), Hyperspectral imaging of convective CO$_2$ ice clouds in the equatorial mesosphere of Mars, *J. Geophys. Res.*, *112*, E11S90, doi:10.1029/2007JE002944.

Morris, R. V., et al. (2000), Mineralogy, composition, and alteration of Mars Pathfinder rocks and soils: Evidence from multispectral, elemental, and magnetic data on terrestrial analogue, SNC meteorite, and Pathfinder samples, *J. Geophys. Res.*, *105*, 1757–1817, doi:10.1029/1999JE001059.

Morris, R. V., et al. (2006), Mössbauer mineralogy of rock, soil, and dust at Gusev Crater, Mars: Spirit's journey through weakly altered olivine basalt on the plains and pervasively altered basalt in the Columbia Hills, *J. Geophys. Res.*, *111*, E02S13, doi:10.1029/2005JE002584.

Murchie, S., et al. (2007), Compact Reconnaissance Imaging Spectrometer for Mars (CRISM) on Mars Reconnaissance Orbiter (MRO), *J. Geophys. Res.*, *112*, E05S03, doi:10.1029/2006JE002682.

Murphy, J. R., and S. Nelli (2002), Mars Pathfinder convective vortices: Frequency of occurrence, *Geophys. Res. Lett.*, *29*(23), 2103, doi:10.1029/2002GL015214.

Neubauer, F. M. (1966), Thermal convection in the Martian atmosphere, *J. Geophys. Res.*, *71*(10), 2419–2426.

Newman, C. E., S. R. Lewis, P. L. Read, and F. Forget (2002), Modeling the Martian dust cycle: 1. Representation of dust transport processes, *J. Geophys. Res.*, *107*(E12), 5123, doi:10.1029/2002JE001910.

Paige, D. A., and A. P. Ingersoll (1985), Annual heat balance of Martian polar caps: Viking observations, *Science*, *228*, 1160–1168, doi:10.1126/science.228.4704.1160.

Parkinson, T. M., and D. M. Hunten (1972), Spectroscopy and aeronomy of O$_2$ on Mars, *J. Atmos. Sci.*, *29*, 1380–1390, doi:10.1175/1520-0469(1972)029<1380:SAAOOO>2.0.CO;2.

Peterfreund, A. R. (1985), Local dust storms and global opacity on Mars as detected by the Viking IRTM, *Tech. Rep. 85-02*, 10 pp., Lunar and Planet. Inst., Houston, Tex.

Peterfreund, A. R., and H. H. Kieffer (1979), Thermal infrared properties of the Martian atmosphere: 3. Local dust clouds, *J. Geophys. Res.*, *84*, 2853–2863, doi:10.1029/JB084iB06p02853.

Porco, C. C., et al. (2004), Cassini imaging science: Instrument characteristics and anticipated scientific investigations at Saturn, *Space Sci. Rev.*, *115*, 363–497, doi:10.1007/s11214-004-1456-7.

Poulet, F., J. P. Bibring, J. F. Mustard, A. Gendrin, N. Mangold, Y. Langevin, R. E. Arvidson, B. Gondet, and C. Gomez (2005), Phyllosilicates on Mars and implications for early Martian climate, *Nature*, *438*, 623–627, doi:10.1038/nature04274.

Richardson, M. I., and R. J. Wilson (2002), Investigation of the nature and stability of the Martian seasonal water cycle with a general circulation model, *J. Geophys. Res.*, *107*(E5), 5031, doi:10.1029/2001JE001536.

Richardson, M. I., J. R. Wilson, and A. V. Rodin (2002), Water ice clouds in the Martian atmosphere: General circulation model experiments with a simple cloud scheme, *J. Geophys. Res.*, *107*(E9), 5064, doi:10.1029/2001JE001804.

Robinson, M. S., E. M. Eliason, H. Hiesinger, B. L. Jolliff, A. S. McEwen, M. C. Malin, M. A. Ravine, D. Roberts, P. C. Thomas, and E. P. Turtle (2005), LROC–Lunar Reconnaissance Orbiter Camera, *Lunar Planet. Sci.*, *XXXVI*, Abstract 1576.

Ryan, J. A., and R. D. Lucich (1983), Possible dust devils: Vortices on Mars, *J. Geophys. Res.*, *88*, 11,005–11,011, doi:10.1029/JC088iC15p11005.

Ryan, J. A., and R. D. Sharman (1981), Two major dust storms, one Mars year apart: Comparison from Viking data, *J. Geophys. Res.*, *86*, 3247–3254, doi:10.1029/JC086iC04p03247.

Shkuratov, Y. G., D. G. Stankevich, D. V. Petrov, P. C. Pinet, A. M. Cord, Y. H. Daydou, and S. D. Chevrel (2005), Interpreting photometry of regolith-like surfaces with different topographies: Shadowing and multiple scattering, *Icarus*, *173*, 3–15, doi:10.1016/j.icarus.2003.12.017.

Singer, R. B., and T. B. McCord (1979), Mars: Large-scale mixing of bright and dark surface materials and implications for analysis of spectral reflectance, *Proc. Lunar Planet. Sci. Conf.*, *Xth*, 1835–1848.

Singer, R. B., T. B. McCord, R. N. Clark, J. B. Adams, and R. L. Huguenin (1979), Mars surface composition from reflectance spectroscopy: A summary, *J. Geophys. Res.*, *84*, 8415–8426, doi:10.1029/JB084iB14p08415.

Sitter, D. N., J. S. Goddard, and R. K. Ferrell (1995), Method for the measurement of the modulation transfer function of sampled imaging systems from bar-target patterns, *Appl. Opt.*, *34*, 746–751, doi:10.1364/AO.34.000746.

Slipher, E. C. (1962), *Mars: The Photographic Story*, 168 pp., Sky, Cambridge, Mass.

Smith, M. D. (2004), Interannual variability in TES atmospheric observations of mars during 1999–2003, *Icarus*, *167*, 148–165, doi:10.1016/j.icarus.2003.09.010.

Smith, M. D., B. J. Conrath, J. C. Pearl, and P. R. Christensen (2002), Thermal emission spectrometer observations of Martian planet-encircling dust storm 2001A, *Icarus*, *157*, 259–263, doi:10.1006/icar.2001.6797.

Smith, P. H., and M. Lemmon (1999), Opacity of the Martian atmosphere measured by the Imager for Mars Pathfinder, *J. Geophys. Res.*, *104*, 8975–8986, doi:10.1029/1998JE900017.

Snyder Hale, A., D. S. Bass, and L. K. Tamppari (2005), Monitoring the perennial Martian northern polar cap with MGS MOC, *Icarus*, *174*, 502–512, doi:10.1016/j.icarus.2004.10.033.

Soderblom, J. M., J. F. Bell III, M. Y. H. Hubbard, and M. J. Wolff (2006), Martian phase function: Modeling the visible to near-infrared surface photometric function using HST-WFPC2 data, *Icarus*, *184*, 401–423, doi:10.1016/j.icarus.2006.05.006.

Soderblom, L. A., K. Edwards, E. M. Eliason, E. M. Sanchez, and M. P. Charette (1978), Global color variations of the Martian surface, *Icarus*, *34*, 446–464, doi:10.1016/0019-1035(78)90037-4.

Stamnes, K., S. C. Tsay, W. Wiscombe, and K. Jayaweera (1988), Numerically stable algorithm for discrete ordinate method radiative transfer in multiple scattering and emitting layered media, *Appl. Opt.*, *27*, 2502–2509, doi:10.1364/AO.27.002502.

Strausberg, M. J., H. Wang, M. I. Richardson, S. Ewald, and A. D. Toigo (2005), Observations of the initiation and evolution of the 2001 Mars global dust storm, *J. Geophys. Res.*, *110*, E02006, doi:10.1029/2004JE002361.

Szwast, M. A., M. I. Richardson, and A. R. Vasavada (2006), Surface dust redistribution on Mars as observed by the Mars Global Surveyor and Viking orbiters, *J. Geophys. Res.*, *111*, E11008, doi:10.1029/2005JE002485.

Thomas, P., and J. Veverka (1979), Seasonal and secular variation of wind streaks on Mars: An analysis of Mariner 9 and Viking data, *J. Geophys. Res.*, *84*, 8131–8146, doi:10.1029/JB084iB14p08131.

Thomas, P. C., P. Gierasch, R. Sullivan, D. S. Miller, E. Alvarez del Castillo, B. A. Cantor, and M. T. Mellon (2003), Mesoscale linear streaks on Mars: Environments of dust entrainment, *Icarus*, *162*, 242–258, doi:10.1016/S0019-1035(03)00028-9.

Thomas, P. C., M. C. Malin, P. B. James, B. A. Cantor, R. M. E. Williams, and P. Gierasch (2005), South polar residual cap of Mars: Features, stratigraphy, and changes, *Icarus*, *174*(2), 535–559, doi:10.1016/j.icarus.2004.07.028.

Thorpe, T. E. (1979), The Mars opposition effect at 20°N latitude and 20°W longitude, *Icarus*, *37*, 389–398, doi:10.1016/0019-1035(79)90003-4.

Thorpe, T. E. (1982), Martian surface properties indicated by the opposition effect, *Icarus*, *49*, 398–415, doi:10.1016/0019-1035(82)90045-8.

Toigo, A. D., M. I. Richardson, R. J. Wilson, H. Wang, and A. P. Ingersoll (2002), A first look at dust lifting and dust storms near the south pole of Mars with mesoscale model, *J. Geophys. Res.*, *107*(E7), 5050, doi:10.1029/2001JE001592.

Tomasi, C., V. Vitale, B. Petkov, A. Lupi, and A. Cacciari (2005), Improved algorithm for calculations of Rayleigh-scattering optical depth in standard atmospheres, *Appl. Opt.*, *44*, 3320–3341, doi:10.1364/AO.44.003320.

Tschimmel, M., M. S. Robinson, D. C. Humm, B. W. Denevi, S. J. Lawrence, S. Brylow, M. Ravine, and T. Ghaemi (2009), Lunar Reconnaissance Orbiter Camera (LROC): Ready for rocks, *Lunar Planet. Sci.*, *XXXX*, Abstract 2475.

Wang, H., R. W. Zurek, and M. I. Richardson (2005), Relationship between frontal dust storms and transient eddy activity in the northern hemisphere of Mars as observed by Mars Global Surveyor, *J. Geophys. Res.*, *110*, E07005, doi:10.1029/2005JE002423.

Wang, H. Q., and A. P. Ingersoll (2002), Martian clouds observed by Mars Global Surveyor mars Orbiter Camera, *J. Geophys. Res.*, *107*(E10), 5078, doi:10.1029/2001JE001815.

Wehrli, C. (1986), Solar spectral irradiance, *World Clim. Res. Programme Publ. Ser. 7/World Meteorol. Organ. Inf. Technol. Div. Rep. 149*, pp. 119–126, World Radiat. Cent., Davos-Dorf, Switzerland.

Wells, E. N., J. Veverka, and P. Thomas (1984), Mars: Experimental study of albedo changes caused by dust fallout, *Icarus*, *58*, 331–338, doi:10.1016/0019-1035(84)90079-4.

Wilson, R. J., and M. I. Richardson (2000), The Martian atmosphere during the Viking mission, part I, Infrared measurements of atmospheric temperatures revisited, *Icarus*, *145*, 555–589, doi:10.1006/icar.2000.6378.

Wolff, M. J., and R. T. Clancy (2003), Constrains on the size of Martian aerosols form Thermal Emission Spectrometer observation, *J. Geophys. Res.*, *108*(E9), 5097, doi:10.1029/2003JE002057.

Wolff, M. J., S. W. Lee, R. T. Clancy, L. J. Martin, P. B. James, and J. F. Bell III (1997), Observations of dust storms on Mars with the Hubble Space Telescope, *J. Geophys. Res.*, *102*, 1679–1692, doi:10.1029/96JE03417.

Wolff, M. J., J. F. Bell III, P. B. James, R. T. Clancy, and S. W. Lee (1999), Hubble Space Telescope observations of the Martian aphelion cloud belt prior to the Mars Pathfinder mission: Water ice cloud and dust optical depths, *J. Geophys. Res.*, *104*, 9027–9042, doi:10.1029/98JE01967.

Wolff, M., R. T. Clancy, M. D. Smith, R. Arvidson, B. Cantor, M. Kahre, R. Morris, and F. Seelos (2007), Investigating the wavelength dependence of the single-scattering albedo of Martian dust aerosols with CRISM and MARCI observations of the very dusty atmosphere in 2007, *Eos Trans. AGU*, *88*(52), Fall Meet. Suppl., Abstract P31D-03.

Zurek, R. W. (1982), Martian great dust storms: An update, *Icarus*, *50*, 288–310.

Zurek, R. W., and L. J. Martin (1993), Interannual variability of planet-encircling dust storms on Mars, *J. Geophys. Res.*, *98*, 3247–3259, doi:10.1029/92JE02936.

Zurek, R. W., and S. E. Smrekar (2007), An overview of the Mars Reconnaissance Orbiter (MRO) science mission, *J. Geophys. Res.*, *112*, E05S01, doi:10.1029/2006JE002701.

J. F. Bell III, T. McConnochie, E. Noe Dobrea, D. Schaeffer, and P. C. Thomas, Department of Astronomy, Cornell University, 402 Space Sciences Building, Ithaca, NY 14853-6801, USA. (jfb8@cornell.edu)

W. M. Calvin, Department of Geological Sciences and Engineering, University of Nevada, Reno, Mail Stop 172, 1664 North Virginia Street, Reno, NV 89557-0138, USA.

B. A. Cantor, M. A. Caplinger, K. S. Edgett, J. Fahle, F. Ghaemi, M. C. Malin, M. A. Ravine, and K. D. Supulver, Malin Space Science Systems, Inc., 9115 Brown Deer Road, San Diego, CA 92121, USA.

R. T. Clancy and M. J. Wolff, Space Science Institute, 4750 Walnut Street, Mail Stop 205, Boulder, CO 80301, USA.

L. J. Edwards and R. M. Haberle, NASA Ames Research Center, Mail Stop 245-3, Moffett Field, CA 94035, USA.

A. Hale, Jet Propulsion Laboratory, 4800 Oak Grove Drive, Pasadena, CA 91103, USA.

P. B. James, Department of Physics and Astronomy, University of Toledo, 2801 West Bancroft, Toledo, OH 43606-3390, USA.

S. W. Lee, Denver Museum of Nature and Science, 2001 Colorado Boulevard, Denver, CO 80205, USA.